

MEMOIRS  
OF THE  
FACULTY OF ENGINEERING  
OSAKA CITY UNIVERSITY

---

VOL. 57

---

DECEMBER 2016

PUBLISHED BY THE  
GRADUATE SCHOOL OF ENGINEERING  
OSAKA CITY UNIVERSITY

This Memoirs is annually issued. Selected original works of the members of the Faculty of Engineering are compiled herein. Abstracts of paper presented elsewhere during the current year are also compiled in the latter part of the volume.

All communications with respect to Memoirs should be addressed to:

Dean of the Graduate School of Engineering  
Osaka City University  
3-3-138, Sugimoto, Sumiyoshi-ku  
Osaka 558-8585, Japan

Editors

Yoshinori KANJO

Souichi SAEKI

Masafumi MURAJI

Eiji SHIKOH

Noritsugu KOMETANI

Tetsu TOKUONO

MEMOIRS OF THE FACULTY OF ENGINEERING  
OSAKA CITY UNIVERSITY

VOL. 57

DECEMBER 2016

CONTENTS

Regular Articles ..... 1

*Mechanical and Physical Engineering*

*Mechanical Engineering*

**Error Control of Single-Point Energy from First-principles Band Calculations**

*Ippei KISHIDA* ..... 1

*Urban Engineering*

*Urban Design and Engineering*

**Questionnaire Survey of Riverfront Residents After Nature-oriented Water Amenity  
Development Project of a Minor River in a Built-up Area**

*Yasumasa FUKUSHIMA and Takashi UCHIDA* ..... 11

**Numerical Study on Effect of Edge distance on the Mechanical Behavior after Major Slip of  
High Strength Frictional Bolted Joints**

*Hitoshi MORIYAMA and Takashi YAMAGUCHI* ..... 27

Abstracts of Papers Published in Other Journals ..... 35

*Mechanical and Physical Engineering*

*Mechanical Engineering* ..... 37

<i>Physical Electronics and Informatics</i>	
<i>Applied Physics and Electronics</i> .....	54
<i>Electrical and Information Engineering</i> .....	66
<i>Applied Chemistry and Bioengineering</i>	
<i>Applied Chemistry and Bioengineering</i> .....	69
<i>Urban Engineering</i>	
<i>Architecture and Building Engineering</i> .....	88
<i>Urban Design and Engineering</i> .....	90

MEMOIRS  
OF THE  
FACULTY OF ENGINEERING  
OSAKA CITY UNIVERSITY

---

VOL. 57

---

DECEMBER 2016

PUBLISHED BY THE  
GRADUATE SCHOOL OF ENGINEERING  
OSAKA CITY UNIVERSITY



# Error Control of Single-Point Energy from First-principles Band Calculations

Ippei KISHIDA\*

( Received October 7, 2016)

## Synopsis

Quantitative analysis of errors in computational science was established. Total energies of fcc and hcp Mg crystals were performed by single-point calculations of first-principles band calculations. Errors in the total energies originated from  $k$ -sampling,  $n$ , and from cutoff energy of plane wave for core potentials,  $E_{\text{cutoff}}$ , were examined. The highest condition calculated value was found to be more suitable for the best estimate, which was alternatively used to the true value, than an arithmetic average and a weighted average. Error components originated from  $n$  and  $E_{\text{cutoff}}$  fit well to  $an^{-3}$  and  $a\exp(bE_{\text{cutoff}})$ , respectively. A whole error was obtained by the propagation of errors in statistics. The value of the total energy including the error was expressed in conventional notation using standard deviation like  $E_{\text{total}} = -1.1516 \pm 0.0004$  [eV]. This technique is able to point out the main error component and the efficient condition to obtain a higher precision. This also made it possible to construct the algorithm that automatically optimizes an accuracy.

keywords: error analysis; error component; best estimate; standard deviation; first-principles band calculations;

## 1. Introduction

There has been increasing necessity of investigating much materials because of the progress of materials science. First-principles calculation, which is only based on the quantum theory, is a powerful technique to analyze physical and chemical properties of materials. A lot of achievements has been already reported in thermal stability,<sup>1-4)</sup> electric potential,<sup>5-8)</sup> ionic conduction,<sup>9-13)</sup> and so on. Although first-principles band calculation can obtain electronic states and total energies with high precision, it is a numerical computation and is not free from errors. In experimental science, error analysis is well systematized and the contained error in measured values are widely performed by an average and a standard deviation of multiple measurements. Since each trial of experimental measurements generally show different values, the error can be analyzed statistically.<sup>14)</sup> In computational science, the same program with the same conditions basically reproduces the same results.<sup>14)</sup> The accuracy of a computer is the reason why the same technique as experiments cannot be used. And the accuracy is also a reason why the importance of correctly estimating an error in the calculation tends to be disregarded. However, an error control is important not only for experiments but also for computations. It is necessary to estimate the errors of results such as significant figures required for discussion.

An error can be roughly divided into a system error and a random error.<sup>15)</sup> The system error is mainly originated from the measurement process. It is desired to devise the experimental process in order to shrink the system error, rather than to analyze it with a statistical method. The system error in the first-principles band calculation includes approximations for  $N$ -body problem, design of core potentials, and so on. Most of them have been reduced by a lot of theoretical scientists and code developers. There are great achievements, e.g., projector augmented wave(PAW) potentials for core potentials,<sup>16,17)</sup> generalized gradient approximation (GGA)<sup>18)</sup> with +U potential<sup>19-21)</sup> for a exchange correlation term, and special point method<sup>22)</sup> and tetrahedron method<sup>23)</sup> with Blöchl correlation<sup>24)</sup> for  $k$ -point sampling of space integration. In addition, the effect of the system error is cancellable by computing the difference between the calculated values with the same conditions. In many cases, therefore, the system error is less likely to become a big problem as a standpoint of an end-user.

The errors originated from  $k$ -mesh and cutoff energy of plane wave for core potentials,  $E_{\text{cutoff}}$ , must be examined in the responsibility of an end-user of calculations on actual materials. It is appropriate to consider that these errors are the independent and random error. There were few strict arguments on the accuracy that depends on these conditions. The significant figures may be decided experientially and semi-quantitatively by overestimating errors to approach on the safe side. The present study establishes the method for quantitative estimation of the error included in a calculated value. We discuss on the total energy, which includes errors originated from  $k$ -mesh and plane-wave cutoff energy. Although geometry optimizations were often performed in actual calculations, the present study dealt only with single-point calculations. This is because a simple system was required to establish a theory of error analysis in the first-principles band calculations. The geometry

---

\* Research Associate, Department of Mechanical Engineering

optimization is more complicated to handle than single-point calculation; e.g., evaluation of force on ions and stress on cell,<sup>25)</sup> truncating condition of ionic loop, an assumption of a fitting function of errors originated from smearing,<sup>26)</sup> and multiple output values to be discussed including lattice constant and ionic coordinates. Nevertheless, it is possible to apply the present technique to geometry optimization.

This paper provides a general framework of an error analysis in the computational science. Precise error analysis was conducted by statistical procedure on calculation parameters that affects the accuracy of a calculated value. Establishing a systematized theory of error analysis, computational researchers will be able to use proper conditions for more minute discussion and to perform larger-scale calculations with suitable load. Moreover, this technique enables automatic determination of conditions, which can become one step for fully automated materials calculation. Now, databases of material properties from first-principles are being accumulated, e.g., Materials Project,<sup>27)</sup> MatNavi<sup>28)</sup> and AFLOW.<sup>29)</sup> The present work can aid to add the information of accuracy of the calculated values to the databases.

## 2. Methodology

### A. Computational conditions and evaluated values

The present study focused on a total energy of a cell,  $E_{\text{total}}$ , as a calculated value among much information obtained from a first-principles band calculation. The total energy is an integration of the energies of many bands occupied by electrons and is fundamental to understand the physical phenomena and chemical reactions of a substance. Since it is a scalar, it is suitable for the discussion on the influence of conditions. We suppose  $k$ -mesh in reciprocal space and cutoff energy of plane wave around ionic core,  $E_{\text{cutoff}}$ , as calculation conditions that mainly affect the error included in calculated  $E_{\text{total}}$ . The former can be divided into sampling numbers,  $n_j$  ( $j = a, b, c$ ), on  $k_j$  axis. Let  $\delta_j$ ,  $\delta_{\text{cutoff}}$ , and  $\delta_{\text{other}}$  be error components in  $E_{\text{total}}$  originated from  $n_j$ ,  $E_{\text{cutoff}}$ , and others, respectively. In the present study,  $\delta_{\text{other}}$  was assumed to be much smaller than  $\delta_a$ ,  $\delta_b$ ,  $\delta_c$ , and  $\delta_{\text{cutoff}}$ . Therefore,

$$|\delta_{\text{other}}| \ll |\delta_a| + |\delta_b| + |\delta_c| + |\delta_{\text{cutoff}}|. \quad (1)$$

This assumption is valid if employed conditions are appropriate. Even if the assumption was not satisfied, it could be satisfied by redefining  $\delta_{\text{other}}$ ; putting main components of  $\delta_{\text{other}}$  under the error control and redefining the residual as  $\delta_{\text{other}}$ .

We employed face centered cubic (fcc) and hexagonal closed pack (hcp) of Mg. These structures have simple and fundamental atomic arrangement, which are included as a sublattice in many crystals. Since all three axes in fcc are equivalent because of the symmetry, three numbers for  $k$ -points,  $n_a$ ,  $n_b$ , and  $n_c$ , are not independent, that is,  $n_a = n_b = n_c$ . Therefore,  $n_a$  is only one independent condition for  $k$ -mesh. On the other hand, since  $k_a$  and  $k_b$  are equivalent and  $k_c$  is independent in hcp,  $n_a$  and  $n_c$  are the independent conditions for  $k$ -mesh in hcp. The range of  $k$ -mesh conditions were employed to be integers in  $3 \leq n_j \leq 20$ . Tetrahedron method with Blöchl correlation (hereafter TMB)<sup>24)</sup> was applied to obtain  $E_{\text{total}}$  from  $k$ -points integration.

The single-point calculations were performed by using density functional theory<sup>30,31)</sup> with the PAW method<sup>16)</sup> as implemented in the VASP code.<sup>17,32,33)</sup> The exchange-correlation term was treated with the Perdew-Burke-Ernzerhof functional<sup>18)</sup> based on the generalized gradient approximation. PAW data set for Mg core had 1s electrons as inner shell orbital and ten valence electrons, and was designed for energy cutoff more than 371 eV. Hence, a plane-wave cutoff energy of  $400 \leq E_{\text{cutoff}} \leq 1200$  [eV] with 50 eV steps were employed.

### B. Best Estimate

A computer program is generally expressed as a function  $f$  that make output  $y$  from  $N$  input data,  $x_1, \dots, x_N$ , that is,

$$y = f(x_1, \dots, x_N).$$

In the present study, it is assumed that  $x_1, \dots, x_N$  are the inputs that causes a random error, and that  $f$  includes the inputs that doesn't cause a random error. Let  $x_i$  be a value of condition  $i$ . For the sake of simplicity, it is assumed that higher  $x_i$  can expect a lower error. Even when  $x_i$  closer to zero is expected a lower error, the assumption above is sufficient by using reciprocal number of  $x_i$  as a condition.

The true value of  $y$ ,  $y_{\text{true}}$ , cannot be obtained by actual calculation. The calculated value generally includes an error since limited values of  $x_i$  are used. Then, the calculated value  $y$  is expressed as a sum of the  $y_{\text{true}}$  and a function of error,  $\delta(x_1, \dots, x_N)$ ;

$$y = f(x_1, \dots, x_N) = y_{\text{true}} + \delta(x_1, \dots, x_N).$$

$\delta(x_1, \dots, x_N)$  is assumed to be a random error and to come out equally in positive and negative direction. The best estimate,  $y_{\text{best}}$ , which is presupposed to include an error, is generally used instead of  $y_{\text{true}}$ .<sup>15)</sup>

$$y = y_{\text{best}} + \delta(x_1, \dots, x_N).$$

In experimental science, the best estimate is often obtained by statistical processing of multiple data. In

computational science, however, multiple trials on the same conditions just reproduces the same result. Then, multiple calculations with varying conditions are often performed to obtain variety of calculated  $y$ .

We examine three methods to obtain the best estimate in the present study: an arithmetic average, a weighted average, and the highest condition calculated value. The arithmetic average is widely used in experimental science. We examine this technique as a candidate to obtain the best estimate. However, the results obtained by calculations with different conditions have different expected errors each other. In order to deal with this problem, the weighted average according to the expected errors is also often performed. Although this technique might seem to match to our purpose, it is not available in general case. This is because the best estimate may require the weights and the weight may require the best estimate. But the weighted average is available without assumption of the best estimate if the ratio of an expected error is evaluated from a condition value. Since the expected error on  $k$ -mesh fits this case as mentioned later in eq.(3), the weighted average was examined by  $k$ -mesh condition. The smallest error should be expected in the calculated value with the highest condition value among limited condition values. Therefore, the highest condition calculated value (hereafter HCCV) was examined as a candidate of the best estimate. The highest condition in the present study was  $n_a = n_c = 20$  and  $E_{\text{cutoff}} = 1200$  [eV].

### C. Fitting function

When  $y_{\text{best}}$  is determined,  $\delta(x_1, \dots, x_N)$  can be performed as follows;

$$\delta(x_1, \dots, x_N) = f(x_1, \dots, x_N) - y_{\text{best}}.$$

Here,  $\bar{\delta} = |\delta|$  is used to treat as a positive function;

$$\bar{\delta}(x_1, \dots, x_N) = |f(x_1, \dots, x_N) - y_{\text{best}}|$$

In the limit that all conditions become the ultimately high value, all  $x_i \rightarrow +\infty$ , then  $\bar{\delta}(x_1, \dots, x_N) \rightarrow 0$ . Error components  $\bar{\delta}_i(x_i)$  can be extracted by scanning only one condition  $i$  to a low condition value.

$$\bar{\delta}_i(x_i) \cong \bar{\delta}(x_1^h, \dots, x_{i-1}^h, x_i, x_{i+1}^h, \dots, x_N^h) \quad (2)$$

where  $x_l^h$  is the sufficiently high condition value for condition  $l$ . Calculated  $\bar{\delta}_i(x_i)$  were fit to an assumed function.

Expected error in TMB is supposed to be proportional to powers to 3 of characteristic  $k$ -spacing<sup>16)</sup>. The function of expected error,  $\bar{\delta}_i(x_i)$ , should be expressed using a fitting coefficient  $a_j$  as follows;

$$\bar{\delta}_j(n_j) = a_j n_j^{-3}, \quad (3)$$

It is difficult to determine the function that fit to error originated from  $E_{\text{cutoff}}$ , because it depends on the design of the core potentials. We assume and examine two functions in the present study.

$$\bar{\delta}_{\text{cutoff}}(E_{\text{cutoff}}) = a E_{\text{cutoff}}^{-3/2} \quad (4)$$

$$\bar{\delta}_{\text{cutoff}}(E_{\text{cutoff}}) = a \exp(b E_{\text{cutoff}}) \quad (5)$$

Eq. (4) is appropriate if an expected error is inversely proportional to the number of the plane wave taken in calculation by cutoff energy. This is based on the idea that the number of plane wave is proportional to

$\left(\frac{2m}{\hbar} E_{\text{cutoff}}\right)^{3/2}$  in three dimensional space. Eq. (5) is appropriate if the contribution of the plane wave of higher

energy decreases exponentially. In this research, data points were fit to the assumed functions by the least-squares method after mathematical operation of transforming to first-degree equation and taking the logarithm.

### D. Control of error

Let  $\bar{\delta}_i(x_i)$ ,  $V_i(x_i)$ , and  $\sigma_i(x_i)$  be the function of error, variance, and standard deviation for condition  $i$ , respectively. Then,

$$\sigma_i(x_i) = \sqrt{V_i(x_i)} = \sqrt{\bar{\delta}_i(x_i)^2} = \bar{\delta}_i(x_i),$$

Let  $\sigma(x_1, \dots, x_N)$  be standard deviation of the whole expected error in a calculated value when a set of arbitrary condition values,  $(x_1, \dots, x_N)$ , is used. If each of  $\sigma_i(x_i)$  is independent and random,  $\sigma(x_1, \dots, x_N)$  can be

expressed as follows.

$$\sigma(x_1, \dots, x_N) = \sqrt{\sigma_1^2(x_1) + \dots + \sigma_N^2(x_N)}$$

This equation corresponds to the propagation of errors in statistics<sup>15)</sup> as follows;

$$\sigma = \sqrt{\sigma_1^2 + \dots + \sigma_N^2}$$

Let  $\sigma_{\text{fcc}}$  and  $\sigma_{\text{hcp}}$  be the standard deviation of the whole error in calculated  $E_{\text{total}}$  of Mg with fcc and hcp structures, respectively. Then,

$$\sigma_{\text{fcc}}(n_a, E_{\text{cutoff}}) = \sqrt{\sigma_a^2(n_a) + \sigma_{\text{cutoff}}^2(E_{\text{cutoff}})} \quad (6)$$

$$\sigma_{\text{hcp}}(n_a, n_c, E_{\text{cutoff}}) = \sqrt{\sigma_a^2(n_a) + \sigma_c^2(n_c) + \sigma_{\text{cutoff}}^2(E_{\text{cutoff}})} \quad (7)$$

### 3. Results and Discussion

#### A. Best estimate

Fig. 1 shows the calculated  $E_{\text{total}}$  of fcc Mg in the conditions that were changed only  $n_a$  from the highest condition. The calculated value obviously converged when higher condition values were employed. The convergence value was about -1.15 eV. The arithmetic average, weighted average, and HCCV were also plotted as horizontal line in Fig. 1. The difference between the arithmetic average and the convergence value was found to be about  $10^{-2}$  eV. This large difference was caused by a large error due to inclusion of calculation with low condition value of  $n_a$ . The arithmetic average was not suitable as the best estimate, since it had a very bigger difference to convergence value than the weighted average and HCCV.

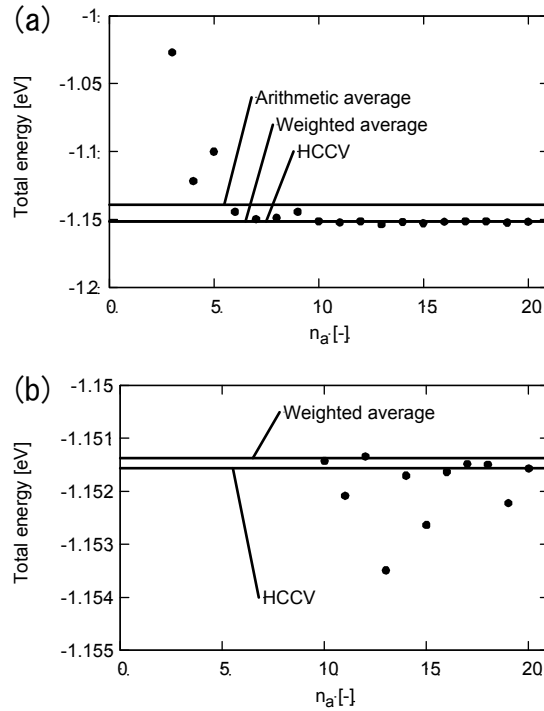


Fig. 1 Calculated total energies (closed circles) of fcc Mg with conditions of fixed  $E_{\text{cutoff}} = 1200$  eV. An arithmetic average value, weighted average, the highest condition calculated value (HCCV) are plotted as horizontal line. (a) All data and (b) enlargement.

The weighted average and HCCV were examined more finely by using Fig. 1 (b), which is an enlargement of Fig. 1 (a). The difference between the weighted average and HCCV was a very small value of  $2 \times 10^{-4}$  eV. We found that it was less likely to cause a big problem even when any of these techniques was employed as best estimate. The weighted average is theoretically preferable than the HCCV, since the HCCV depends on one data point and is more sensitive to the error in the point than the weighted average. Therefore, the weighted average

seemed to be suitable for the best estimate of only one condition. However, it is difficult to use the weighted average when the whole error from various conditions is examined. It is because weighted average allows multiple best estimates for condition axes and this thinking collides the thinking that the true value should correspond to the only one best estimate. Moreover, the HCCV has advantages of easier evaluation than weighted average even if the weight is not expectable. From these viewpoints, the HCCV should be used as the best estimate for analysis of the whole error. The HCCV of fcc Mg was described to be -1.151566 eV as a raw output without regard of significant figures. This value was employed as the best estimate of fcc Mg in the present study.

The similar dependencies to  $n_a$  of fcc Mg were found in results on  $n_a$  and  $n_c$  of hcp Mg (see Figs. 3 and 4). In addition, the HCCV was also suitable for the best estimate for varying  $E_{\text{cutoff}}$  (see Figs. 5 and 6).

## B. Error originated from $k$ -point

Since the HCCV was adopted as the best estimate, calculated  $\bar{\delta}_i(x_i)$  in the highest condition must be zero and does not have information. The HCCV should be excluded from fitting datapoints. Therefore, calculated  $\bar{\delta}_i(x_i)$  without the HCCV were fit to assumed functions.

Fig. 2 shows calculated  $\bar{\delta}_a(n_a)$  on each  $n_a$  of fcc Mg and fitting function to eq. (3). Data points on  $n_a \leq 2$  does not exist since the tetrahedron method cannot be executed. Fitting functions to  $a_j n_j^{-1}$  and  $a_j n_j^{-2}$  are also plotted in Fig. 2 for comparison. It was clear that they did not reflect the behavior of the error in high  $k$  region. The errors fit well to  $a_j n_j^{-3}$ , which was derived from the theory of TMB.<sup>24)</sup> This results showed the validity of eq. (1). Since the behavior of the error agreed with the function even in the low  $k$  region, the large errors should not be ignored but should be used for evaluation of an expected error. The fitting function to eq. (3) was obtained as follows.

$$\sigma_{\text{fcc},a}(n_a) = 3.2n_a^{-3} [\text{eV}]. \quad (8)$$

According to this equation, the error component originated from  $n_a$  can be estimated even in the highest condition, that is,  $\sigma_{\text{fcc},a}(20) = 4.0 \times 10^{-4}$  eV.

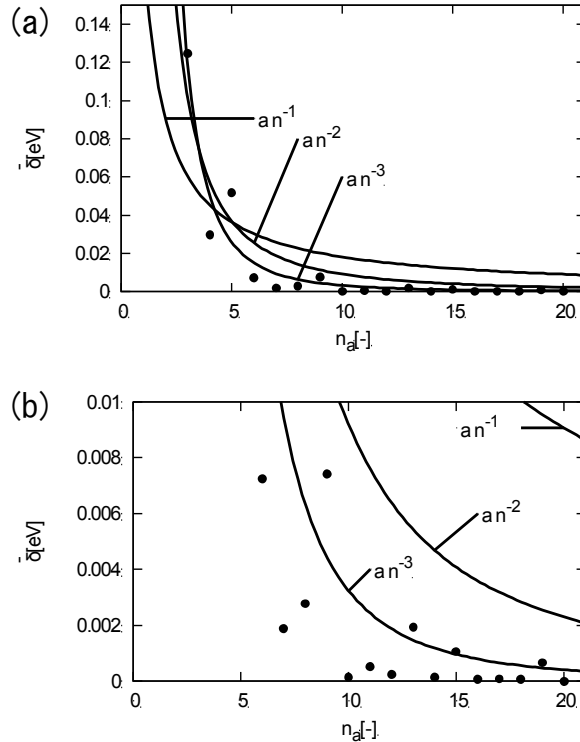


Fig. 2 Absolute value of differences between calculated total energies and HCCV of fcc Mg with conditions of fixed  $E_{\text{cutoff}} = 1200$  eV. Candidates for fitting functions were also shown. (a) All data points and (b) enlargement.

Figs. 3 and 4 shows calculated  $\bar{\delta}_a(n_a)$  and  $\bar{\delta}_c(n_c)$  of hcp Mg, respectively. Their fitting function to  $a_j n_j^{-3}$ , which were also shown in the figures, reflected the similar dependency of errors to fcc Mg shown in Fig. 2. Since the errors on both the  $n_a$  and  $n_c$  in the hcp structure matched well to  $a_j n_j^{-3}$ , it was shown that the errors on each axis can be analyzed by fitting to respective  $a_j n_j^{-3}$ . The fitting functions to eq. (3) were obtained as follows.

$$\begin{aligned} \sigma_{\text{hcp},a}(n_a) &= 9.2n_a^{-3} [\text{eV}], \\ \sigma_{\text{hcp},c}(n_c) &= 1.0n_c^{-3} [\text{eV}]. \end{aligned}$$

According to this equation, the error components originated from  $n_a$  and  $n_c$  in the highest condition were estimated to be  $\sigma_{\text{hcp},a}(20)=1.2\times 10^{-3}$  eV and  $\sigma_{\text{hcp},c}(20)=1.3\times 10^{-4}$  eV.

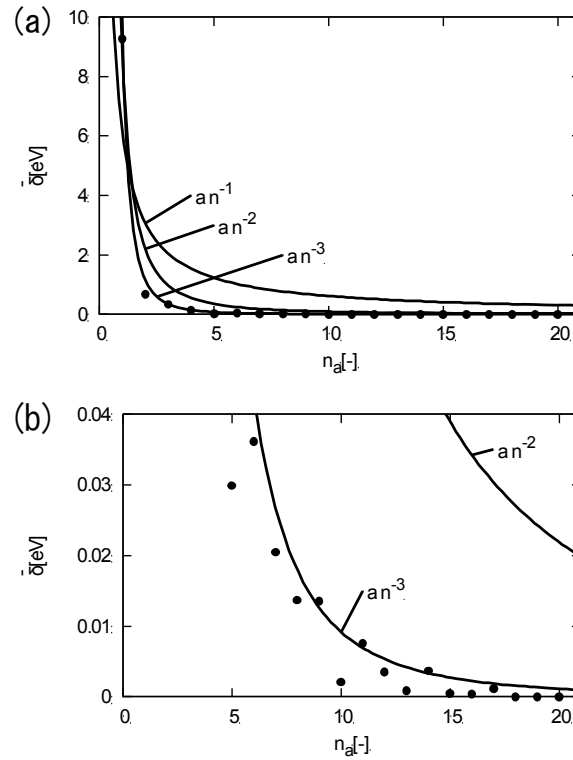


Fig. 3 Absolute value of differences between calculated total energies and HCCV of hcp Mg with conditions of fixed  $E_{\text{cutoff}} = 1200$  eV and  $n_c = 20$ . Candidates for fitting functions were also shown. (a) All data points and (b) enlargement.

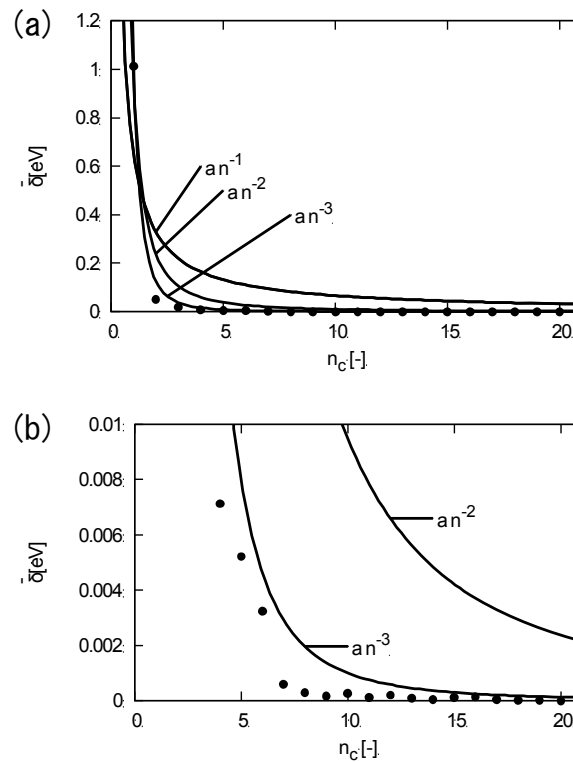


Fig. 4 Absolute value of differences between calculated total energies and HCCV of hcp Mg with conditions of fixed  $E_{\text{cutoff}} = 1200$  eV and  $n_a = 20$ . Candidates for fitting functions were also shown. (a) All data points and (b) enlargement.

### C. Error originated from cutoff energy

Fig. 5 shows calculated  $\bar{\delta}_{\text{cutoff}}(E_{\text{cutoff}})$  of fcc Mg and fitting function to eqs. (4) and (5). The error tended to decrease rapidly by the increase in  $E_{\text{cutoff}}$ . It was found that the fitting function to  $aE_{\text{cutoff}}^{-3/2}$  did not reflect the convergence of the error in the high  $E_{\text{cutoff}}$  region well. The function that fit to  $a\exp(bE_{\text{cutoff}})$  could explain the tendency for the rapid decrease of the error. Although this function does not have a well-established theoretical background, it is suggested to have sufficient performance to guess the error practically. Since many core potentials would be designed to converge results with a limited cutoff energy, the fitting function to  $a\exp(bE_{\text{cutoff}})$  is expected to agree widely with other core potentials. The fitting function to eq. (5) was obtained as  $a=0.58$ ,  $b=-7.8 \times 10^{-3}$ , that is,

$$\sigma_{\text{fcc,cutoff}}(E_{\text{cutoff}}) = 0.58\exp(-7.8 \times 10^{-3}E_{\text{cutoff}}) [\text{eV}]. \quad (9)$$

According to this equation, the error component originated from  $E_{\text{cutoff}}$  in the highest condition was estimated to be  $\sigma_{\text{fcc,cutoff}}(1200)=5.2 \times 10^{-5}$  [eV].

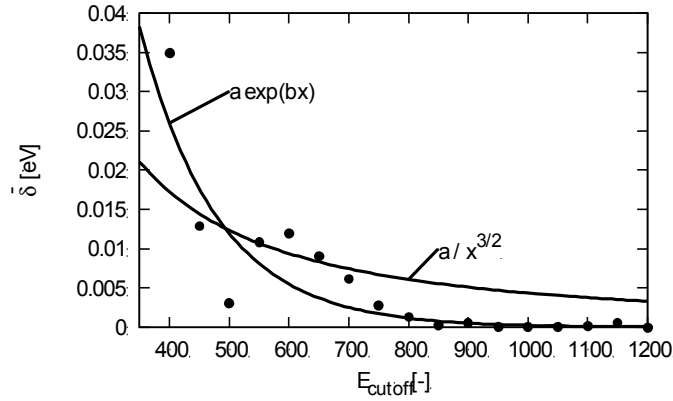


Fig. 5 Absolute value of differences between calculated total energies and HCCV of fcc Mg with conditions of fixed  $n_a = 20$ . Candidates for fitting functions were also shown. (a) All data points and (b) enlargement.

An error from  $E_{\text{cutoff}}$  of hcp Mg was also examined. Fig. 6 shows calculated  $\bar{\delta}_{\text{cutoff}}(E_{\text{cutoff}})$  of hcp Mg and fitting functions to eqs. (4) and (5). Similar to fcc Mg, the function that fit to  $a\exp(bE_{\text{cutoff}})$  could explain the behavior of the error. The fitting function to eq. (5) was obtained as  $a = 0.24$  and  $b = -4.3 \times 10^{-3}$ , that is,

$$\sigma_{\text{hcp,cutoff}}(E_{\text{cutoff}}) = 0.24\exp(-4.3 \times 10^{-3}E_{\text{cutoff}}) [\text{eV}].$$

According to this equation, the error component originated from  $E_{\text{cutoff}}$  in the highest condition was estimated to be  $\sigma_{\text{hcp,cutoff}}(1200)=6.7 \times 10^{-4}$  [eV].

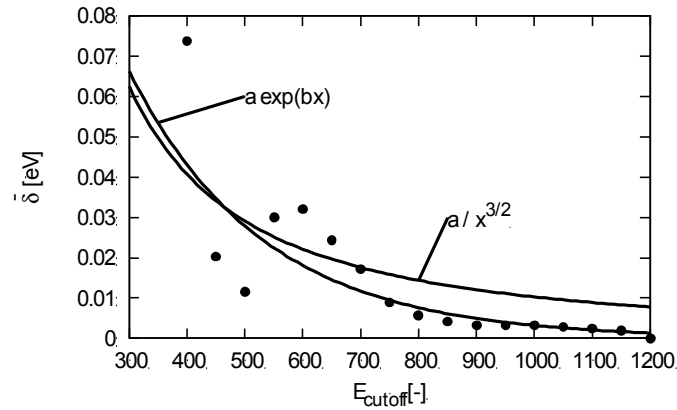


Fig. 6 Absolute value of differences between calculated total energies and HCCV of hcp Mg with conditions of fixed  $n_a = n_c = 20$ . Candidates for fitting functions were also shown. (a) All data points and (b) enlargement.

#### D. Whole error analysis

All components of the error in the HCCV of fcc Mg were already obtained. The error in the HCCV can be obtained by substituting the components,  $\sigma_{\text{fcc},a}(20) = 4.0 \times 10^{-4}$  eV and  $\sigma_{\text{fcc},\text{cutoff}}(1200) = 5.2 \times 10^{-5}$  eV, to eq. (6), that is,  $\sigma_{\text{fcc}}(20, 1200) \approx 4.0 \times 10^{-4}$  [eV]. The value including the error can be expressed in conventional notation using standard deviation,  $E_{\text{total},\text{fcc}} = -1.1516 \pm 0.0004$  [eV]. This error was found to be originated mainly from  $n_a$ . This suggests that it would be effective to use  $n_a$  higher than 20 if a higher precision was required, and to use  $E_{\text{cutoff}}$  lower than 1200 eV if a lower precision was permitted.

All components of the error in the HCCV of hcp Mg were also already obtained. Substituting  $\sigma_{\text{hcp},a}(20) = 1.2 \times 10^{-3}$  eV,  $\sigma_{\text{hcp},c}(20) = 1.3 \times 10^{-4}$  eV, and  $\sigma_{\text{hcp},\text{cutoff}}(1200) = 6.7 \times 10^{-4}$  [eV] to eq. (7),  $\sigma_{\text{hcp}}(20, 20, 1200) \approx 1.3 \times 10^{-3}$  [eV] was obtained. A magnitude relation of the error components were found to be  $\sigma_{\text{hcp},c} < \sigma_{\text{hcp},\text{encut}} < \sigma_{\text{hcp},a}$ . Similar to fcc Mg, it is effective to use higher  $n_a$  than 20 if a higher precision was required.

#### E. Control of error

The present technique can be used to decide a calculation condition to satisfy an acceptable error. For example, if the standard deviation of  $E_{\text{total}}$  of fcc Mg was required to be  $\sigma_{\text{fcc}} \leq 1 \times 10^{-3}$  eV, eq. (6) would be as follows.

$$\sigma_{\text{fcc}}(n_a, E_{\text{cutoff}}) = \sqrt{\sigma_{\text{fcc},a}^2(n_a) + \sigma_{\text{fcc},\text{cutoff}}^2(E_{\text{cutoff}})} \leq 1 \times 10^{-3}. \quad (10)$$

Each of the  $\sigma_{\text{fcc},a}$  and  $\sigma_{\text{fcc},\text{cutoff}}$  should satisfy the below equation as a rough target value;

$$\sigma_{\text{fcc},a}(n_a) = \sigma_{\text{fcc},\text{cutoff}}(E_{\text{cutoff}}) \leq \frac{\sqrt{2}}{2} \times 10^{-3} \text{ [eV]}. \quad (11)$$

Substituting each of eqs. (8) and (9) to eq. (11), we can obtain the conditions, that is,

$$n_a \geq 16.6, \quad (12)$$

$$E_{\text{cutoff}} \geq 864 \text{ [eV]}. \quad (13)$$

#### F. Error optimization

By this research, the algorithm that automatically optimizes an accuracy becomes able to be designed as follows.

1. Determine an acceptable error of a calculation as performed in eq. (10)
2. Obtain the acceptable error per condition as performed in eq. (11).
3. Set the highest condition.
4. Generate a sequence of each condition  $i$  by varying the condition value from the highest condition as shown at eq. (2).
5. Calculate with the conditions and fit the results to the assumed function to obtain  $\sigma_i$ .
6. Evaluate a sufficient condition value for the acceptable error per condition by using  $\sigma_i$  as performed at eqs. (12) and (13).
7. Reset the new highest condition by combination of the evaluated conditions.
8. Repeat from 4 to 7 until all expected error components in the HCCV become less than the acceptable error per condition.

This method would enable to assure the precision of calculations and will aid fully automated materials calculations.

### 4. Conclusion

We established quantitative analysis of random errors in computational science. Errors in total energies obtained by singlepoint calculations of first-principles band calculations were examined. The highest condition calculated value was found to be more suitable for the best estimate than an arithmetic average and a weighted average. Error components originated from  $k$ -sampling number,  $n$ , and cutoff energy,  $E_{\text{cutoff}}$ , fit well to  $an^{-3}$  and  $a\exp(bE_{\text{cutoff}})$ , respectively. A whole error was obtained by the propagation of errors in statistics. The value of the total energy including the error was expressed in conventional notation using standard deviation like  $E_{\text{total}} = -1.1516 \pm 0.0004$  [eV]. This method enables to assure the precision of calculations. Since the present technique made it possible to point out the main error component and the efficient condition to obtain a higher precision, computational researchers will be able to use proper conditions for more minute discussion and to perform larger-scale calculations with suitable load. This also made it possible to construct the algorithm that automatically

optimizes an accuracy, so that it becomes one step for fully automated materials calculation.

### Acknowledgments

This work was supported by JSPS KAKENHI Grant Number 26820319 and 15K06491.

### References

- 1) N. Bernstein, M. Johannes, and K. Hoang, *Physical Review Letters*, **109**, 205702 (2012).
- 2) H. Ben Yahia, M. Shikano, and H. Kobayashi, *Chemistry of Materials*, **25**, 3687 (2013).
- 3) I. Kishida, K. Orita, A. Nakamura, and Y. Yokogawa, *Journal of Power Sources*, **241**, 1 (2013).
- 4) K. Lejaeghere, J. Jaeken, V. Van Speybroeck, and S. Cottenier, *Physical Review B*, **89**, 014304 (2014).
- 5) M. K. Aydinol and G. Ceder, *Journal of the Electrochemical Society*, **144**, 3832 (1997).
- 6) M. K. Aydinol, A. F. Kohan, and G. Ceder, *Journal of Power Sources*, **68**, 664 (1997).
- 7) V. L. Chevrier, S. P. Ong, R. Armiento, M. K. Y. Chan, and G. Ceder, *Physical Review B*, **82**, 075122 (2010).
- 8) I. A. Courtney, J. S. Tse, O. Mao, J. Hafner, and J. R. Dahn, *Physical Review B*, **58**, 15583 (1998).
- 9) I. Kishida, F. Oba, Y. Koyama, A. Kuwabara, and I. Tanaka, *Physical Review B*, **80**, 24116 (2009).
- 10) G. K. P. Dathar, D. Sheppard, K. J. Stevenson, and G. Henkelman, *Chemistry of Materials*, **23**, 4032 (2011).
- 11) C. A. J. Fisher, A. Kuwabara, and H. Moriwake, *Journal of the Ceramic Society of Japan*, **119**, 861 (2011).
- 12) K. Fujimura, A. Seko, Y. Koyama, A. Kuwabara, I. Kishida, K. Shitara, C. A. J. Fisher, H. Moriwake, and I. Tanaka, *Advanced Energy Materials*, **3**, 980 (2013).
- 13) I. Kishida, *AIP Advances*, **5**, 107107 (2015).
- 14) M. Iri and Y. Fujino, *Suuchi Keisan no Joushiki (Common sense in Numerical Calculation)*, edited by M. Nanjou (Kyoritsu Shuppan, Tokyo, 1985).
- 15) J. R. Taylor, *An Introduction to Error Analysis: The Study of Uncertainties in Physical Measurements*, 2nd ed. (University Science Books, 1996) p. 327.
- 16) P. E. Blöchl, *Physical Review B*, **50**, 17953 (1994).
- 17) G. Kresse and D. Joubert, *Physical Review B*, **59**, 1758 (1999).
- 18) J. P. Perdew, K. Burke, and M. Ernzerhof, *Physical Review Letters*, **77**, 3865 (1996).
- 19) V. I. Anisimov, J. Zaanen, and O. K. Andersen, *Physical Review B*, **44**, 943 (1991).
- 20) M. Cococcioni and S. De Gironcoli, *Physical Review B*, **71**, 35105 (2005).
- 21) K. Knížek, Z. Jiráček, J. Hejtmánek, P. Novák, W. Ku, and Z. Jirak, *Physical Review B*, **79**, 014430 (2009).
- 22) H. Monkhorst and J. Pack, *Physical Review B*, **13**, 5188 (1976).
- 23) G. Gilat, *Physical Review B*, **12**, 3479 (1975).
- 24) P. E. Blöchl, O. Jepsen, and O. K. Andersen, *Physical Review B*, **49**, 16223 (1994).
- 25) R. P. Feynman, *Physical Review* **56**, 340 (1939).
- 26) M. Methfessel and A. Paxton, *Physical Review B*, **40**, 3616 (1989).
- 27) A. Jain, S. P. Ong, G. Hautier, W. Chen, W. D. Richards, S. Dacek, S. Cholia, D. Gunter, D. Skinner, G. Ceder, and K. A. Persson, *APL Materials*, **1**, 011002 (2013).
- 28) URL: <http://mits.nims.go.jp/>.
- 29) URL: <http://afloplib.org/>.
- 30) P. Hohenberg and W. Kohn, *Physical Review*, **136**, B864 (1964).
- 31) W. Kohn and L. J. Sham, *Physical Review*, **140**, A1133 (1965).
- 32) G. Kresse and J. Hafner, *Physical Review B*, **48**, 13115 (1993).
- 33) G. Kresse and J. Furthmüller, *Physical Review B*, **54**, 11169 (1996).



# **Questionnaire Survey of Riverfront Residents after Nature-oriented Water Amenity Development Project of a Minor River in a Built-up Area**

Yasumasa FUKUSHIMA\* and Takashi UCHIDA\*\*

(Received October 7, 2016)

## **Synopsis**

Recent municipal river development emphasizes environment and water amenity as well as flood control and water utilization. A waterfront development project involves multiple subjects such as a commissioning entity, riverfront residents, a planner, and agencies concerned. However, riverfront residents occasionally evaluate the project too little to encourage waterfront utilization. Therefore, examination based on a posterior situation is important for future improvement.

This study assesses waterside development in a minor river in an emerging built-up area. The actual conditions of and estimation of water amenity are comprehended using questionnaire survey of the riverfront residents at the project area several years after the completion. The analysis specifically examines their involvement in waterfront development. This study is expected to contribute fundamental data for examination and discussion of a development procedure highly appreciated by riverfront residents and effective for promotion of utilization, as concrete measures for smooth project performance and consensus building in the waterfront development of a municipal river.

**KEYWORDS:** Waterfront development, Consensus building, Public involvement, Posterior evaluation, Residents' attitudes

## **1. INTRODUCTION**

### **1.1 Background and objective of research**

Recent municipal river development adopts an approach of waterfront development emphasizing environment and water amenity as well as flood control and water utilization. However, various parameters of respective rivers or districts, such as development conditions or environment, are complicatedly related. Moreover, waterside development projects typically involve multiple subjects such as a commissioning entity, riverfront residents, a planner, and related agencies, so that arrangements for mutual consensus building become important. It is particularly necessary to extract riverfront residents' intentions. Nevertheless, riverfront residents occasionally appreciate a project too little to promote waterfront utilization. Therefore, an a posteriori examination of a situation is important for future improvement.

This study examines the case of waterside development conducted along with a land readjustment project at a minor river in an emerging built-up area. The actual condition of waterfront use is ascertained using a questionnaire survey to riverfront residents in addition to knowledge obtained through the process of project planning, performance, and subsequent secular change. Analyses particularly emphasize residents' involvement in waterfront development. This study was conducted to establish fundamental data for examination and discussion of concrete measures for smooth project performance and consensus building for the waterfront development of municipal rivers.

### **1.2 Previous studies**

The few studies of actual conditions of use and posterior evaluation by riverfront residents of waterfront development and landscape development of municipal rivers include the following.

Aniya et al. (2005)<sup>1)</sup> conduct a questionnaire and oral survey after organizing a plan and design intent for posterior evaluation of a waterfront landscape development project. They perform evaluation from a viewpoint

---

\* Student, Doctor Course of Department of Civil Engineering

\*\* Professor, Department of Civil Engineering

in agreement with development objectives to elucidate the actual conditions of everyday use by riverfront residents. Furthermore, they propose a method for extracting information that is useful for future planning and design.

Toyoda et al. (2007)<sup>2)</sup> analyze variation in the spatial configuration of a riverfront and the relation thereof with residents' attitudes, and the relation between the characteristics of the spatial configuration of a riverfront and residents' behavior, using a questionnaire and behavior observation survey. Results reveal aspects of waterfront development in a municipal river, suggesting that riverfront residents prefer taking a walk on a riverbank to direct contact such as touching the water, so it is important to ensure the continuity of pedestrian space.

Although particularly addressing not waterfront development of a municipal river but a creek, Inohae et al. (2003)<sup>3)</sup> administered a questionnaire survey to landowners and new residents about a creek improved by a land readjustment project. They point out that the diverse directives of respective land-owners cannot be actualized. Moreover, new residents' directives cannot be satisfied either, in the case of development advanced under a plan designed by administrators and approved passively by the land-owners' association.

These studies investigate the actual conditions of use and appreciation by riverfront residents of waterfront development and landscape development of municipal rivers. They analyze and evaluate the results. Nevertheless few studies propose concrete measures for smooth project performance and consensus building in the future. Furthermore, few studies have examined waterfront development especially that progressing along with land readjustment projects at a municipal river.

### 1.3 Method of research

This study specifically examines X River, a minor river of the class A Yodogawa River system, which flows through an emerging built-up area in a Kyoto suburb. Concepts and planning and design intent for waterfront development<sup>4)</sup> are reviewed<sup>5)</sup>. A questionnaire survey to riverfront residents is conducted<sup>6)</sup>. The attributes, personal history, and tastes of riverfront residents and the actual condition of waterfront use and their attitudes about a waterfront development project are investigated based on the survey results. Moreover, the data are tabulated with emphasis on respondent groups that use the water-front frequently and which have high intention for involvement in a waterfront construction plan.

A development procedure that is highly appreciated by riverfront residents and which is effective for promotion of utilization should be discussed as a concrete measure for smooth project performance and consensus building in the waterfront development of a municipal river. As the first step, posterior evaluation is conducted. Fundamental data are acquired for discriminant analysis (quantification method II) to ascertain the relation of factors affecting attitudes of riverfront residents about waterfront use and the waterfront development project.

## 2. TARGET OF RESEARCH

Target sections of this study in X River (see Fig. 1) extend for about 3 km. They include section B as the center where waterfront development and a land readjustment project were conducted together, and upstream section A and downstream section C, where the implementation states of waterfront development and a land readjustment project differed. Differences in the development status and the riverfront situation of each section are described below.

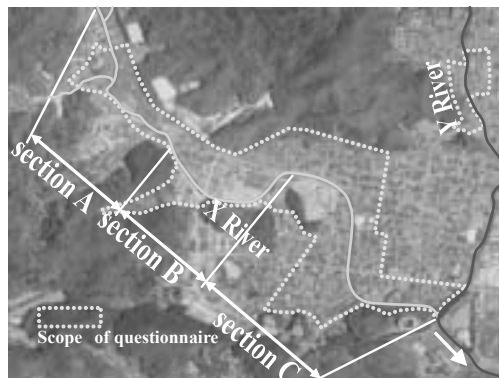


Fig. 1 Target area of Study for X River.

## **2.1 Section A:**

This is an upstream section where neither waterfront development nor a land readjustment project has been implemented. The riverfront situation is roughly divisible into two types: the uppermost stream section, where houses built by development stand in a row; and a cultivated riverfront. Undeveloped river banks and sections with excessive luxuriance of herbaceous plants both exist, but there has been no approach taken with the waterfront. On only one side is there a promenade or a road along the river, with continuity along the flow direction.

## **2.2 Section B:**

This is a middle reach section among the target sections. It underwent nature-oriented river construction with an unlined bed in 2002–2011 along with a land readjustment project with "river channel improvement and nature-oriented development plan by cooperation with a land readjustment project" as a concept. Although some cultivated land remains along the riverfront, urbanization has progressed after the land readjustment project. Maintenance by deep-joint block revetment suppresses the excessive luxuriant growth of herbaceous plants on the river banks, although spontaneous water routes formed by the power of the river are sustained in the river channel. Seven approaches for access to the water-front are prepared. There is a promenade or a road on both banks along the riverside, so that continuity in the flow direction is assured.

## **2.3 Section C:**

This is a downstream section where river development with a lined bed was conducted along with a land readjustment project before 2002. Urbanization of the riverfront has advanced considerably and the ratio of cultivated land is the lowest. River banks are built with blocks, and more or less luxuriant growth of herbaceous plants can be observed except for deposited soil in the river channel, which presents an artificial appearance. Ladders or footsteps are pre-pared on the steep slope revetment for approach to the waterfront, and there is a promenade or a road on both banks along the riverside, so that continuity in the flow direction is assured.

# **3. DESIGN OF QUESTIONNAIRE SURVEY**

## **3.1 Target area and questionnaire participants**

The questionnaire target area includes around 1,900 households within a distance of several hundred meters from X River in Sections A–C at about 3 km upstream from the junction of Y River and the lowest reach of X River (see Fig. 1). This questionnaire specifically examines riverfront residents in the sections with different conditions of the implementation states of waterfront development and a land readjustment project. The results enable us to comprehend the effects of waterfront development and residents' intentions for involvement in a waterfront construction plan, and to analyze differences thereof. The outer edge of section B includes an old village in which no land readjustment has been conducted to show differences. Moreover, a part of riverfront of Y River into which X River flows is included in the target, to show effects of residents in a riverfront of a river other than the river examined here.

The questionnaire was distributed to all ordinary households in the target area, but educational institution related facilities such as schools and student residences and public facilities such as care welfare facilities were excluded. For participants it was re-quested that one adult respondent should represent each household to answer the questionnaire on the "relation with the river" of the respondent and the entire household.

## **3.2 Focus points for survey result analysis**

Fig. 2 depicts the cause–effect linkage (hypothesis) of focus points in the analysis of survey results, question setting of the questionnaire survey, and items to be analyzed.

For collecting opinions from a group with interest in waterfront development based on the waterfront use experience and high intentions for involvement in waterfront construction planning, it is effective to conduct development that accommodates the needs of riverfront residents by collecting opinions efficiently. Factors affecting attitudes related to today's waterfront use situation and a waterfront development project include riverfront residents' attributes such as their living environment and household structure. In addition, tastes related to the waterfront are strongly influential and are regarded as affected by personal history. Accordingly, analysis that specifically addresses the following points was con-ducted for this study.

**1) Tastes related to the waterfront**

Presumably, groups with interest in waterfront development and high intentions for involvement in waterfront construction planning have strong correlation with a group using the waterfront frequently. These groups are expected to carry a basically good image for waterfront use.

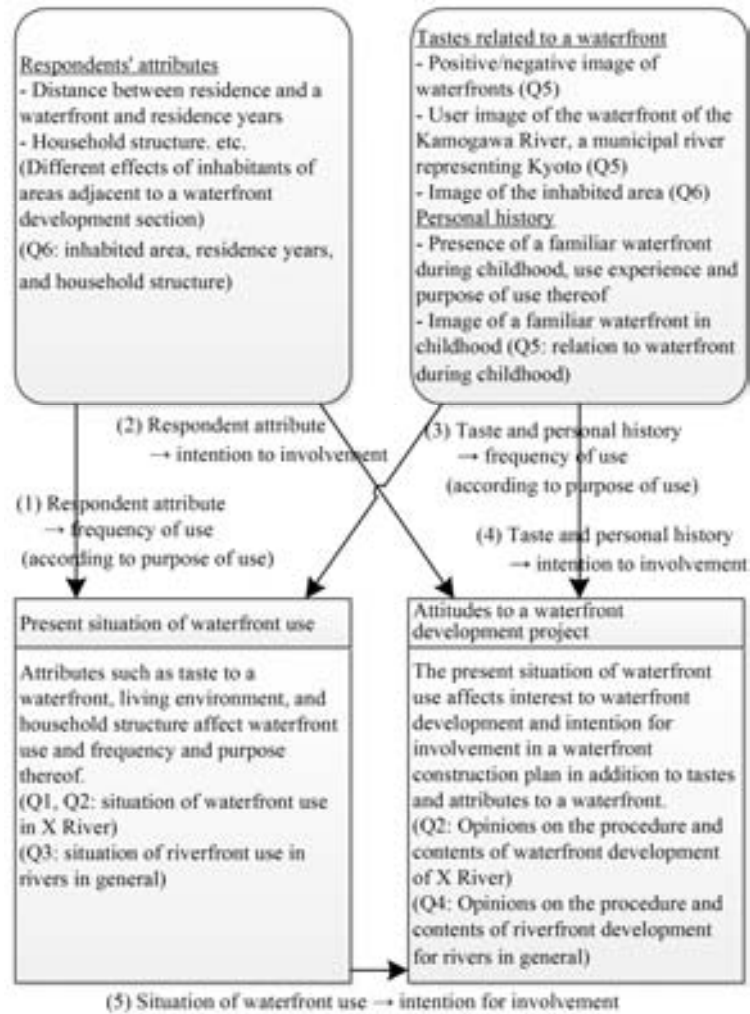
**2) Personal history**

It is presumed that tastes related to a waterfront are affected greatly by personal history such as intimacy with a waterfront during childhood, and that such a historical attitude is formed by the presence of a nearby waterfront during childhood and the image and use experience thereof.

**3) Attributes**

It is assumed that factors such as household structure, such as distance from a residence to a developed waterfront, residence years, and with and without children, as well as tastes related to a waterfront, affect the frequency and purpose of water-front use, interest in waterfront development, and intention for involvement in a waterfront construction plan.

Most X Riverfront residents in section B moved to the area after completion of the land readjustment project. Analyses specifically addressed the residents of downstream section C, upstream section A, and the Y Riverfront are conducted to elucidate the effects of waterfront development in section B on surrounding residents. Whether a person is qualified as resident of a district of a land readjustment project was determined according to the inhabited area and residence years.



(number in parenthesis denotes an analysis plan number)  
 Fig. 2 Cause-effect linkage (hypothesis) and question setting.

### 3.3 Question setting of questionnaire

An outline of questionnaire questions is presented in Table 1. Q1 asks the use situation of a waterfront in sections A–C of X River. Q2 asks opinions about the procedure and contents of waterfront development and the use situation of the developed water-front in section B of X River. Q3–Q5 ask the overall use situation of riverfronts, opinions related to procedures and contents of waterfront development, and lifestyle, not limited to X River but over rivers in general. Q6 asks about the inhabited area, residence years, and household structure.

Table 1 Items and contents of questionnaire survey

No.	Survey item	Contents
Q1	Situation of waterfront use of sections A–C in X River	Degree of acknowledgment, use experience, frequency of use, purpose of use, moving means, what is thought to be good
Q2	Opinions on the procedure and contents of waterfront development and situation of waterfront use in section B in X River	Degree of acknowledgment of development, comparison with an ideal image of environmental aspects, balance of environment and use, fluctuation in frequency of use, and frequency of use and degree of acknowledgment of an approach
Q3	Situation of the waterfront use in rivers in general	Use experience, river name, frequency of use, purpose of use in a river other than X River
Q4	Opinions about the procedure and contents of riverfront development for rivers in general	Range of subjects of hearing, intention for involvement in a waterfront construction plan, necessity for an approach, structure of a preferable approach, necessity for a landing bridge
Q5	Lifestyle related to rivers in general	The image over a riverfront, a purpose of use assuming to visit the Kamogawa River, and presence, image, and purposes of use of a familiar waterfront during childhood
Q6	Inhabited area, years of residence, and household structure	Inhabited area, presence of a land readjustment project in the inhabited area, residence years, what is thought to be good of the inhabited area, and household structure

## 4. IMPLEMENTATION OF QUESTIONNAIRE AND GROUND TOTAL OF SURVEY RESULTS

### 4.1 Distribution / recovery situations

The implementation situation of the questionnaire survey is the following. The total recovery rate was about 22%, in which 27% were in sections B and C and 21% were in section A, slightly higher the downstream where waterfront use is regarded as high. The recovery rate from an old village in the outer edge of section B was as low as 6%, and that from an old village in the riverfront of Y River different from X River was as low as 3% (Fig. 3).

Date of distribution: July 5, 2014 (Sat.)

Number distributed: about 1,900 residences

Distribution and collection procedure: distribution by throw-in / collection by mail

Recovery rate: About 22% (417 of about 1,900)

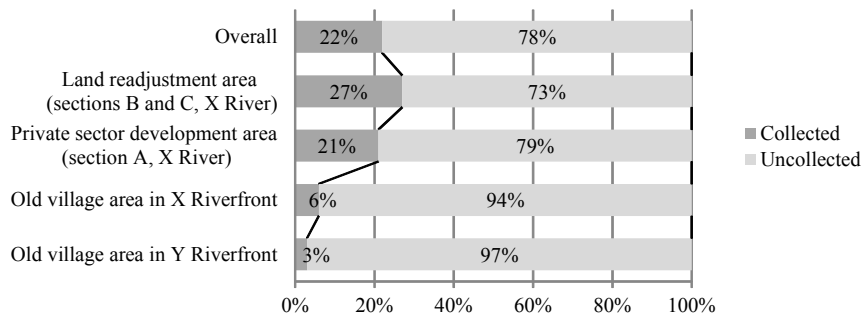


Fig. 3 Questionnaire recovery rate for each area.

### 4.2 Attributes of respondents

The respondent household structure was mostly households of 1–4 persons. Households of only adults aged 19 and over were 31%, those of only elderly people aged 61 and over were 30%, those with children in an elementary school or younger 29%, and the fraction of households with underage members in a junior high school or older was the lowest: 10%.

Residence years were divided into two types, 10 years or more and 5 years or fewer. Few households

reported 5–10 years of residence. Many households with children in an elementary school or younger had inhabited the area for five years or fewer (moved in after land readjustment), although many households of only adults had inhabited the area for 10 years or longer (since before land readjustment) (see Fig. 4).

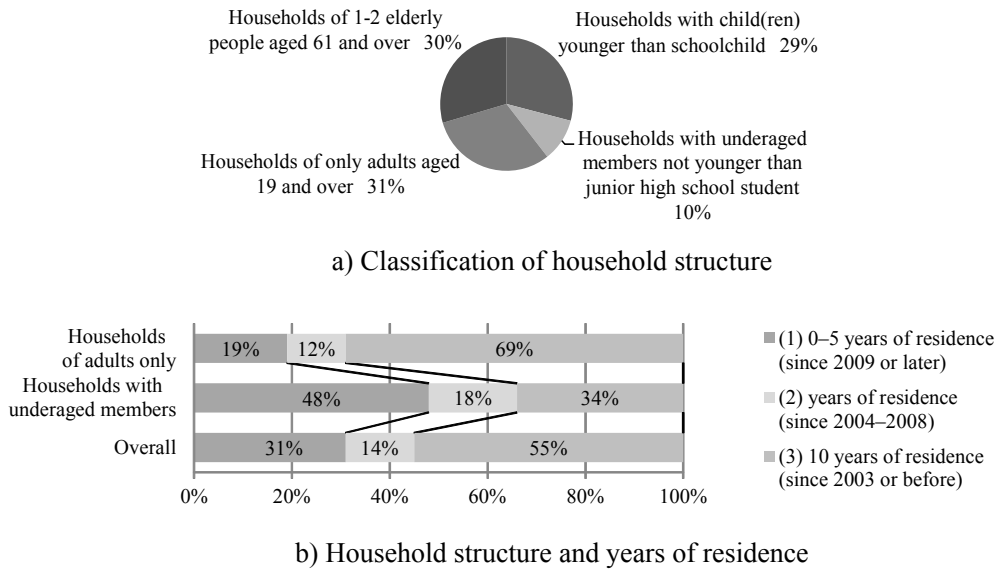


Fig. 4 Respondents' household structure and years of residence.

### 4.3 Actual condition of waterfront use

The degree of awareness to each of section A–C and the presence of use experience mostly showed agreement. However in general, the degree of awareness and use experience were lower of the upper sections than the section in which the respondent resided, probably because a subway station and commercial facilities are located on the neighborhood of the lowest part of downstream section C, so that residents nearby rarely go upstream from the residential area during usual living activities. Nevertheless, as for section B, the degree of awareness and use experience of downstream section A were high, probably because section B is within walking distance (in general not more than 1 km) from section A, which is a major purpose of the use of a waterfront.

Regarding frequency of use, 31% of respondents used a waterfront area almost every day; 32% used a waterfront area 1–3 times per week, so that use once or more per week were about 60%, but about 20% used such areas only several times per year. Purposes of use include taking a walk (67%), followed by shopping (12%), commuting (8%), and using a riverside park (4%).

Section B used to have so much difficulty in access of the river channel that direct waterfront use was rare before development. Children were observed to play with the water using an approach (stairs) constructed in the revetment after development, so that an increase in direct waterfront use as the effect of waterfront development had been anticipated. However, the fraction of direct waterfront use among all users was as low as 3% (Fig. 5).

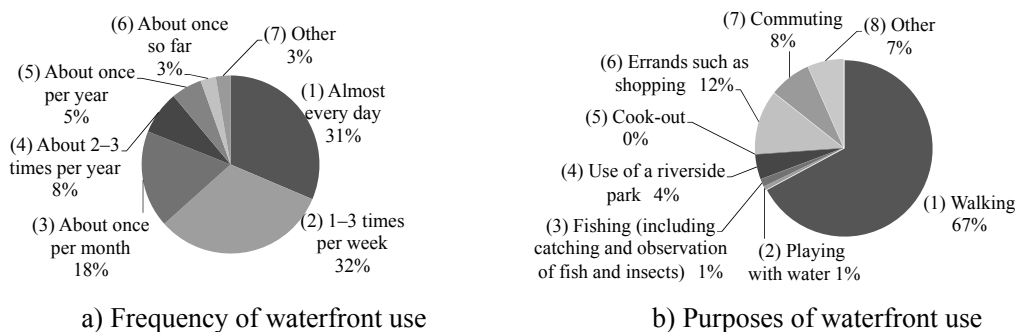


Fig. 5 Frequency and purpose of waterfront use in X River.

Major points that are thought to be good about X River include "abundant nature," "easy to walk along the riverside," and "close to home," although "many living things" and "easy to walk into the water" are minor (Fig. 6). These points agree with the fact that a waterfront is used as an area that is easy to walk along where one can feel nature near home, and that the major purposes of use include taking a walk.

There was little change in the frequency of use before and after development in most of the respondent group that was aware of waterfront development in section B (84%), although there were a few answers of increased frequency of use in a group that uses a waterfront mainly for walking. This is presumably true because taking a walk as a purpose of use before development is unchanged. Nevertheless, it is considered that the frequency of use increased slightly because the continuity of the promenade on the levee crown was ensured.

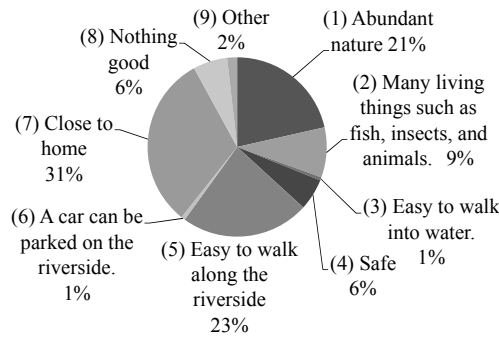


Fig. 6 What is thought good of X River.

#### 4.4 Riverfront residents' attitudes against waterfront development project

Results show that 68% of residents of 10 years or longer residence were aware of waterfront development aiming at Nature Oriented River Construction in section B, but only 16% of residents of five years or shorter residence who moved in after the land readjustment project were aware of it (see Fig. 7).

A respondent group that was aware of waterfront development in section B was asked about compatibility with the ideal image in an environmental aspect (See Fig. 8). Of those respondents, 48% answered that it was mostly compatible, about three times the number who answered that it was not compatible (19%). The project was advanced mainly by the commissioning entity and the planner under a plan aimed at "maintenance and creation of intimate natural environment" based on a partial hearing with old village residents. Generally speaking, waterfront development is regarded as acceptable by riverfront residents.

Regarding the method of hearing for riverfront residents (Fig. 9), few answered "No necessity of hearing" (2%), but respondents were generally negative about self-involvement, answering "A flier or brochure is sufficient (60%)" or "No intention for involvement" (9%).

Results show that 29% of respondents were positive about involvement in a waterfront construction plan by expressing opinions related to river creation activity with residents' participation such as at workshops and explanatory meetings to local residents. In addition, a request for a hearing was made by a questionnaire survey or via the internet because temporal restrictions did not permit attending a workshop.

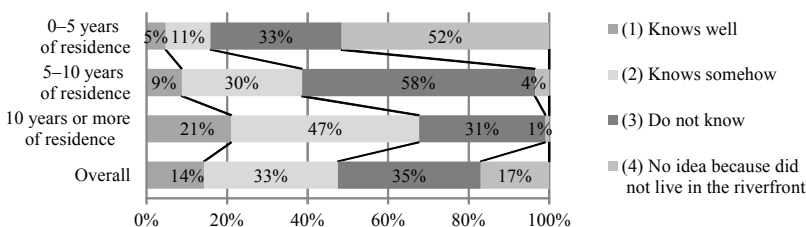


Fig. 7 Degree of acknowledgment of waterfront development of X River (classified by years of residence).

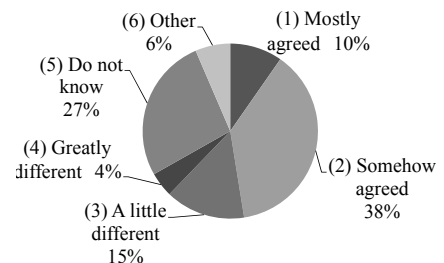


Fig. 8 Comparison with ideal image of waterfront development in X River.

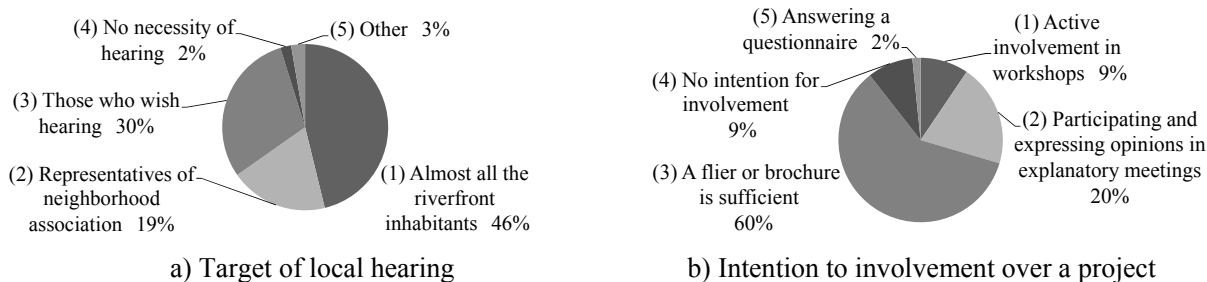


Fig. 9 Riverfront residents' attitudes against waterfront development project.

**4.5 Personal history and tastes of riverfront residents**

Of respondents, 92% had a positive image about the river waterfront (Fig. 10). Regarding personal history on a waterfront, as many as 84% of respondents reported a familiar waterfront (river, lake, pond, and swamp) close to their home in their childhood (Fig. 11). The waterfront did not necessarily provide a positive image, but there were many answers of negative images, such as "dangerous," "dirty," "deserted," "unpleasant," and "smelling bad." Nevertheless, 63% reported direct waterfront use of playing with water, catching fish, and catching insects as purposes of use. A nearby waterfront during childhood did not necessarily give a positive image, but the ideal image of use of a familiar waterfront was established: ideally, they are safe and beautiful, with abundant nature, where people can feel merriment and healing by direct waterfront use.

Of respondents, 39% nominated "streets in harmony with nature" as a salient benefit of the presently inhabited area (Fig. 12), followed by "clean air, beautiful mountain range and river" (44% cited all three items), whereas "beautiful street" accounted for only 6%. This result revealed the tastes of riverfront residents, who favor a balanced living environment with streets, but who love rich natural environment around the inhabited area. These tastes show agreement with those for the waterfront use described above in terms of loving a natural environment.

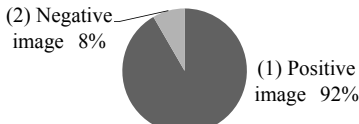


Fig. 10 Image over waterfront.

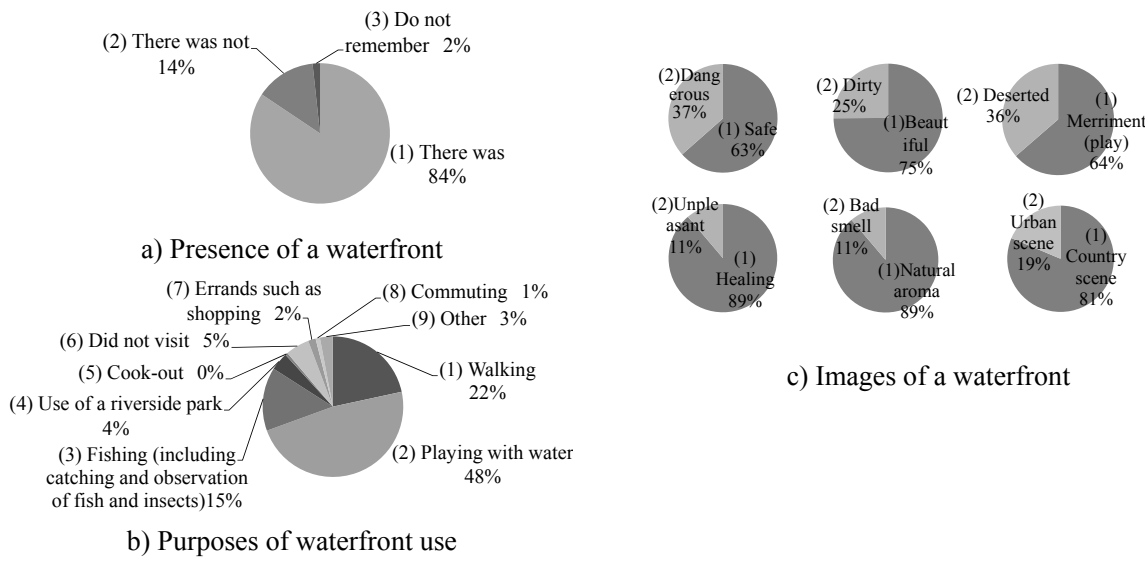


Fig. 11 Personal history on waterfront (intimate waterfront during childhood).

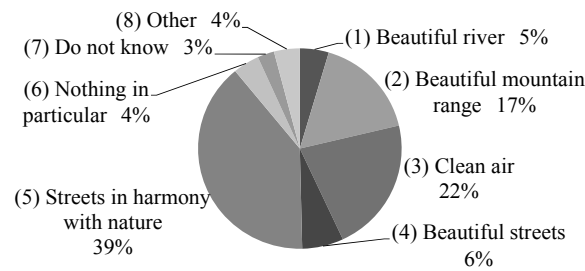


Fig. 12 What is good of inhabited area.

## 5. TABULATION FOR ANALYSIS OF SURVEY RESULTS

Cross tabulation was conducted to capture the trends of attributes and tastes that affect residents' attitudes related to the use situation of a waterfront and a waterfront development project, for each item to be analyzed in the cause-effect linkage (hypothesis) of focus points (1)–(5) in the analysis of survey results shown in Fig. 2.

A difference exists in the trend of attributes and tastes as factors of actual conditions of waterfront use between direct users intending to have direct water contact or walking and transit users intending to do shopping and commuting. For that reason, tabulation was conducted according to the purpose of use.

### 5.1 Relation of attributes with actual conditions of waterfront use and riverfront residents' attitudes

Figures 13–18 present results of cross tabulation of the attributes of respondents affecting the present situation of waterfront use and attitudes about a waterfront development project (analysis plans (1)-1, (1)-2, and (2) in Fig. 2).

#### 1) Frequency of use of X River and intention to involvement according to inhabited area

The groups of "(2) private sector development area (section A, X River)" reported higher frequency of use. Fewer of them had low intention to involvement compared with those in "(1) land readjustment area (sections B and C, X River)." Especially, the high frequency of use by transit users of section A in upstream X River was prominent. Presumably, they commute to stations in sections B and C downstream on the X River.

Residents of areas adjacent to the waterfront development project used the waterfront frequently irrespective of purpose and had high intentions for involvement in a waterfront construction plan.

#### 2) Frequency of use of X River and intention to involvement according to residence years

No significant effect was found on the frequency of use in a direct use group from the viewpoint of once or more times of use per week. However, frequent use of the riverfront was observed in the group of "(2) 5–10 years of residence" in the transit group. No prominent effect of residence years on intention for involvement in a waterfront construction plan, but that of the group "(2) 5–10 years of residence" was slightly low.

No significant effect was found for the intention to involvement, but the frequency of use by the group of 5–10 years of residence was high.

#### 3) Frequency of use of X River and intention to involvement according to household structure

The effect of the household structure differed a little for each purpose of use in the viewpoint of once or more use per week. Frequent riverfront users were direct users of "(2) households with underage member(s) not younger than junior high school student" and "(4) households of elderly people only," and transit users of "(1) households with child(ren) younger than schoolchild" and "(3) households of adults only." Consequently, an entirely opposite tendency was evident. The purposes of use were highly compatible with the respondents' age group (household structure).

It is characteristic that the intention to involvement of households with children is the highest, followed by households of adults only. Households with elderly people only were the lowest.

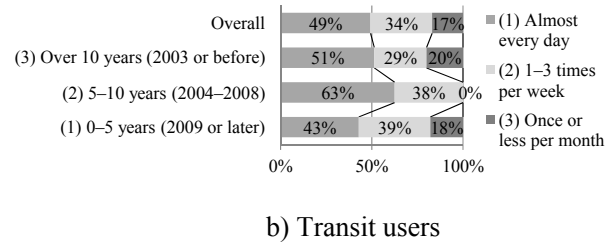
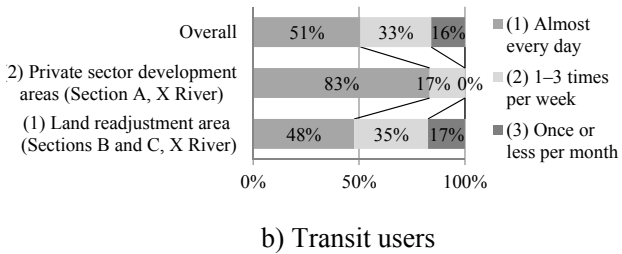
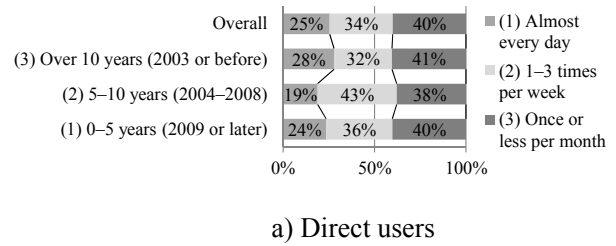
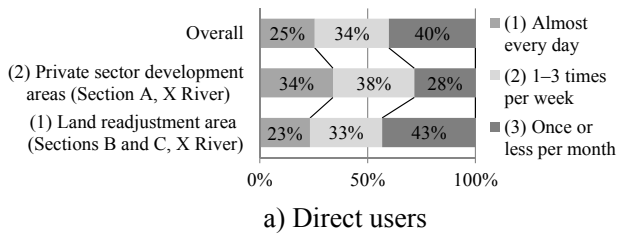


Fig. 13 Frequency of use of X River (according to inhabited area).

Fig. 14 Frequency of use of X River (according to years of habitation).

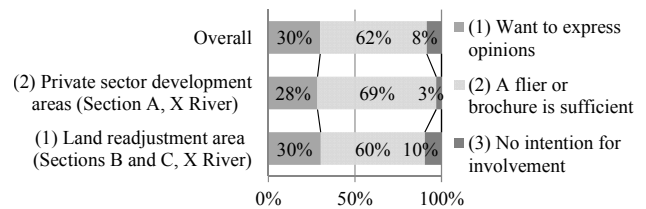
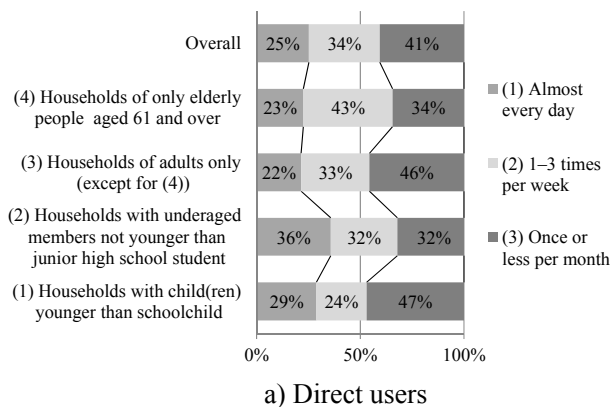


Fig. 16 intention for involvement in waterfront development project (according to inhabited area).

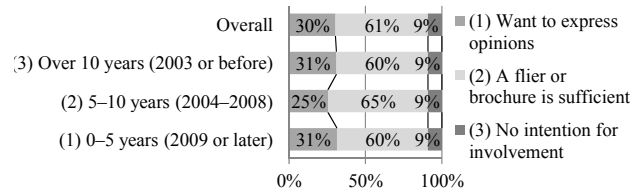
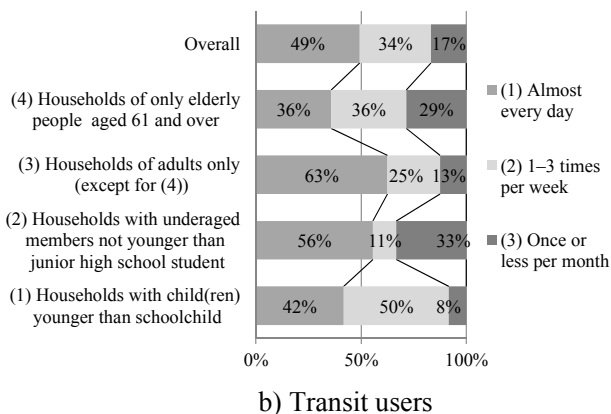


Fig. 17 intention for involvement in waterfront development project (according to years of habitation).

Fig. 15 Frequency of use of X River (according to household structure).

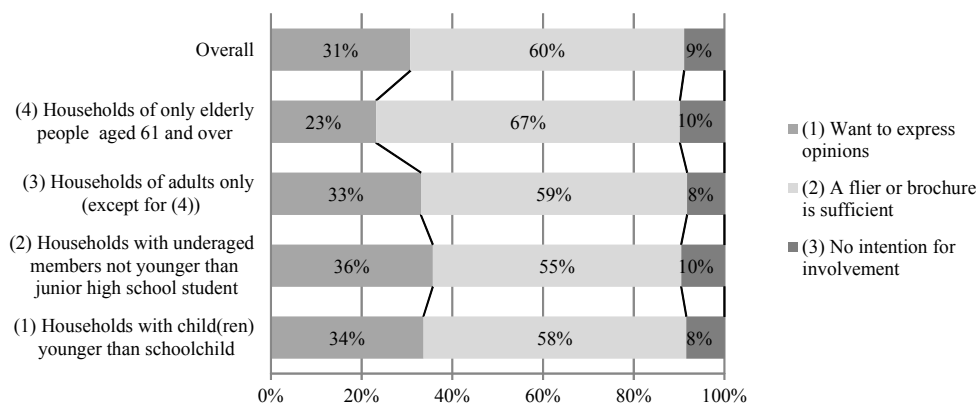


Fig. 18 Intention for involvement in waterfront development project (according to household structure)

## 5.2 Relation of tastes and personal history with the actual condition of waterfront use and riverfront residents' attitudes

Figures 19–26 present results of cross tabulation of tastes and personal history of respondents affecting the present situation of waterfront use and attitudes about a waterfront development project (analysis plans (3)-1, (3)-2, and (4) in Fig. 2).

### 1) Frequency of use of X River and intention to involvement according to the waterfront image

The frequency of use by direct users in "(2) negative image" was unexpectedly high. That by transit users was low, but this result was unreliable because of the small sample.

The intention to involvement of respondents of "(2) negative image" over a waterfront was low.

### 2) Frequency of use of X River and intention to involvement according to the user image of the Kamogawa River

The frequency of use was low by a group having a user image of "(1) direct waterfront use" of the Kamogawa River among the direct users of X River. The frequency of use by the group of "(1) direct waterfront use" among transit users was high, but this trend was unreliable because of the small sample of respondents of "(1) direct waterfront use."

Consequently, it is characteristic that the intention to involvement of those who have an image of direct waterfront use to the Kamogawa River, a municipal river representing Kyoto.

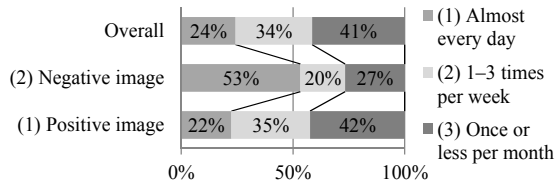
### 3) Frequency of use of X River and intention to involvement according to image of the inhabited area

No effect of difference in images was observed in the inhabited area. However, the frequency of use and intention to involvement of those impressed rather by the beauty of streets in harmony with nature than by the beauty of natural environment itself was high.

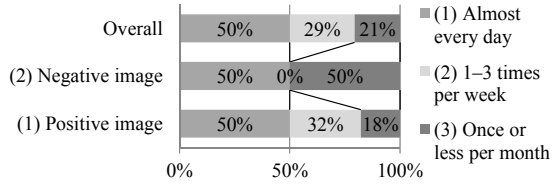
### 4) Frequency of use of X River and intention to involvement according to purposes for childhood waterfront use

From the viewpoint of almost daily use, the frequency of use of X River of the groups of "(1) direct waterfront use" and "(2) indirect waterfront uses (e.g. walking)" was high, whereas that of the group of "(3) there was a waterfront nearby but did not visit" was low.

Regarding the purpose of visiting a waterfront in childhood, those who had used a waterfront for direct use or indirect use (e.g. walking) in their childhood still used a waterfront frequently and had high intention for involvement. It is characteristic that those who did not visit a waterfront even though one exists nearby do not use it frequently but have high intention to involvement.

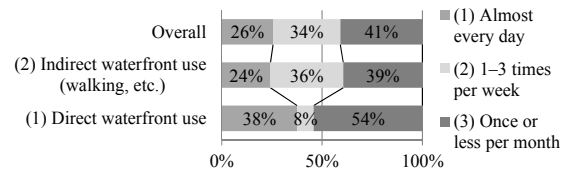


a) Direct users

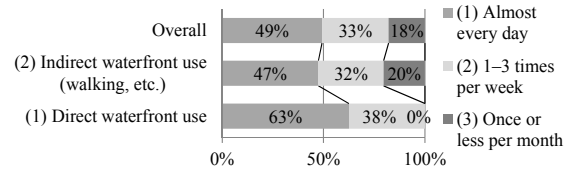


b) Transit users

Fig. 19 Frequency of use of X River (according to general image to waterfront).

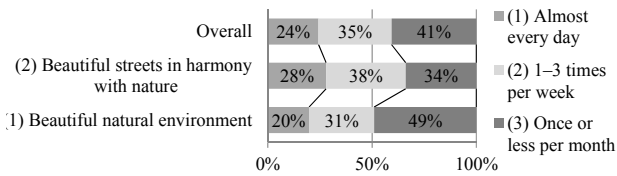


a) Direct users

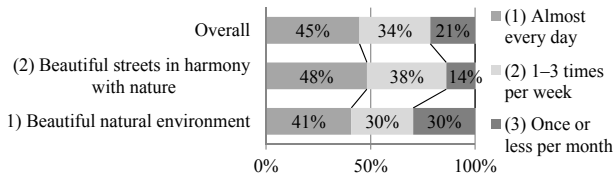


b) Transit users

Fig. 20 Frequency of use of X River (according to user image of Kamogawa riverfront).

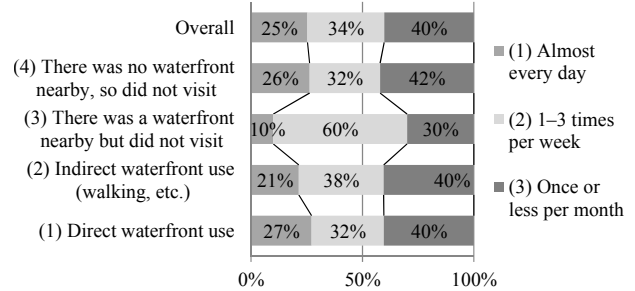


a) Direct users

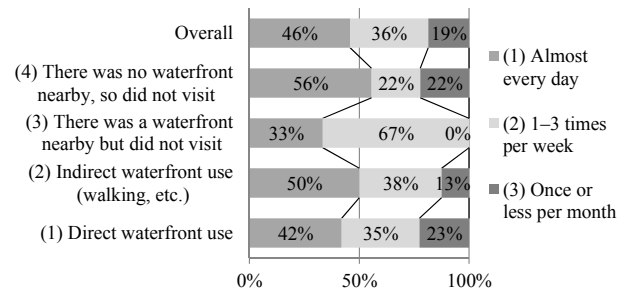


b) Transit users

Fig. 21 Frequency of use of X River (according to image to inhibited area).



a) Direct users



b) Transit users

Fig. 22 Frequency of use of X River (according to purposes to visit waterfront during childhood).

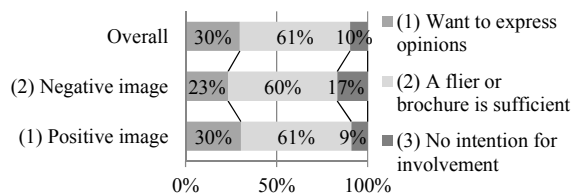


Fig. 23 Intention for involvement in waterfront development project (according to general image to waterfront).

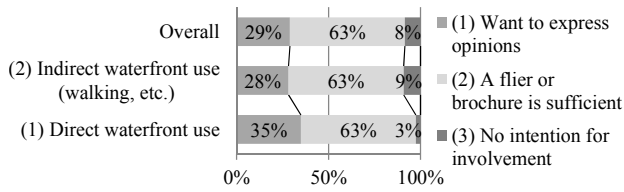


Fig. 24 Intention for involvement in waterfront development project (according to user image of Kamogawa riverfront).

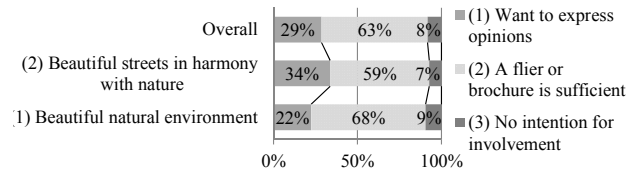


Fig. 25 Intention for involvement in waterfront development project (according to image to inhibited area).

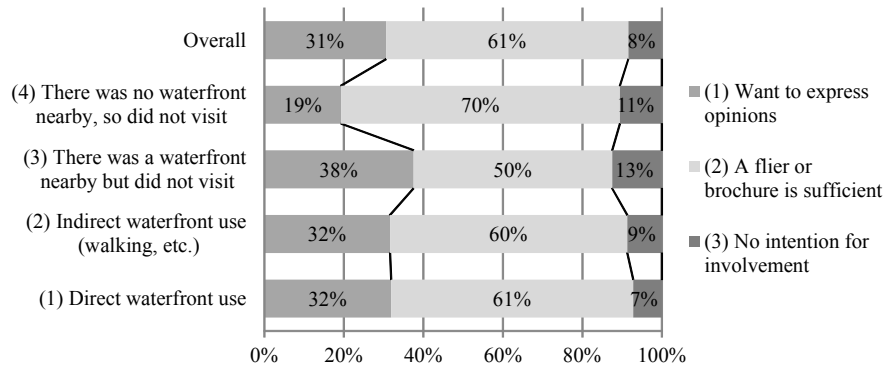


Fig. 26 Intention for involvement in waterfront development project (according to purposes to visit waterfront during childhood).

### 5.3 Relation between the actual condition of water-front use and riverfront residents' attitudes

Figures 27–29 present results of cross tabulation of the present waterfront use situation affecting attitudes to a waterfront development project (analysis plan number (5)-1 and (5)-2 in Fig. 2).

Residents with high intention for involvement include those who used intimate X Riverfront 1–3 times per week as indirect waterfront use (shopping and commuting) and those who used riverfronts other than intimate X River for direct use or indirect use (e.g. walking).

It is characteristic that the intention of involvement of a group that uses X Riverfront mainly for walking at high frequency is not so high, needless to say, it is much lower for a group with low frequency of use.

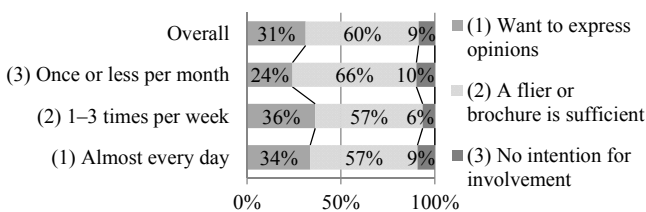


Fig. 27 Intention for involvement in waterfront construction plan

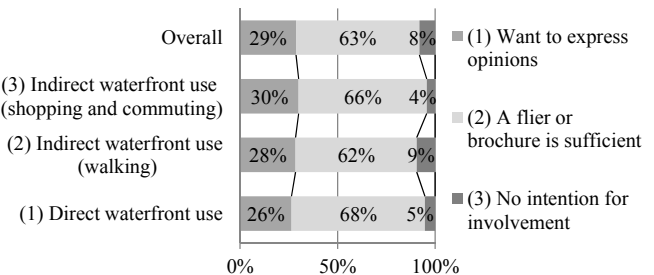


Fig. 28 Intention for involvement in waterfront construction plan (according to purpose of use of X River).

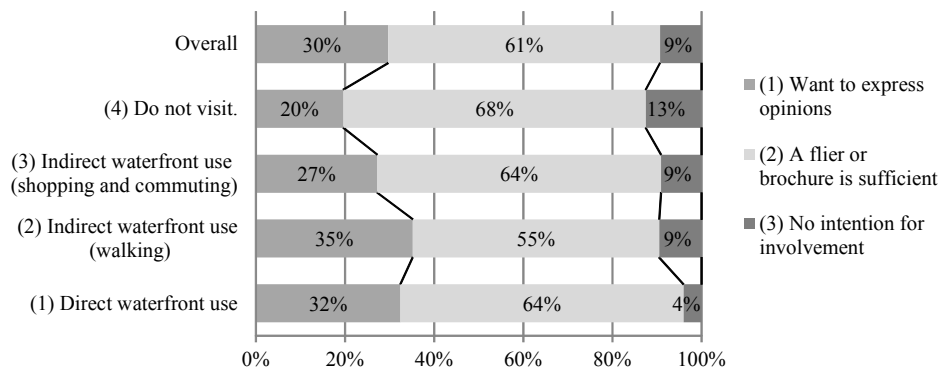


Fig. 29 Intention for involvement in waterfront construction plan (according to purpose of use of rivers other than X River).

### 5.4 Summary

The information tabulated for each analysis plan item in a cause-effect linkage (hypothesis) yields the following inferences about the characteristics of "groups of high/low intention of waterfront use" and "groups of high/low intention for involvement in a waterfront construction plan," which shall be verified in future analysis.

Those who used a waterfront in childhood still use it frequently and have strong intentions for involvement, but those who did not visit a waterfront although even when one was nearby use it infrequently at present, but have high intentions to involvement.

Transit users who use a waterfront for shopping and as a traveling route for commuting use it frequently and have high intentions to involvement.

However, a group mainly comprising elderly people who use a waterfront mainly for walking frequently, with long years of residence and bound to the community, has many opportunities to participate as a representative of residents in explanatory meetings to local residents. However, its intention for involvement in a waterfront construction plan is so low that it is inappropriate for consolidation of opinions.

## 6. CONCLUSION

This tabulation has elucidated trends in attributes, tastes, and personal history that are regarded as affecting the present situation of waterfront use and riverfront residents' attitudes to a waterfront development project. Consequently, this study is regarded as meaningful as an accomplishment of the first step for examination and discussion of a development procedure that is highly appreciated by riverfront residents and which is effective for promotion of utilization, as a concrete measure for smooth project performance and consensus building in waterfront development of municipal rivers.

Our future study shall include discriminant analysis (quantification method II) to evaluate the effects of factors such as attributes, tastes, and personal history, which are regarded as affecting the actual conditions of waterfront use and riverfront residents' attitudes, and furthermore, comprehensive analysis by covariance structure analysis to elucidate the characteristics of resident groups affecting planning of waterfront development projects.

### References

- 1) Aniya, S., Fukui, T. and Shinohara, O.: Study of Posterior Evaluation of Projects on Landscape Development – Case Study of the Sakaigawa River, Urayasu –, Proceedings of Conference for Architecture and Infrastructure Environment, No. 1, pp. 73-82, 2005.
- 2) Toyoda, M., Miyake, Y. and Sasaki, Y.: Surveillance Study of Relationship of Spatial Characterization of Kanda-Gawa Riverfront with User Behavior and Attitudes, Proceedings of Conference for Architecture and Infrastructure Environment, No. 3, pp. 293-300, 2007.
- 3) Inohae, T. and Sotoo, K.: Discussion on Inhabitants' Intention and Ideal State of Participation in Public Space Development – On the Case of Residential Area Development by Land Readjustment –, Proceedings of 27th Conference for Infrastructure Planning and Management (CD-ROM), 4pp., 2003.

- 4) Fukushima, Y., Nomi, T., Taniyama, T., and Kawamura, K.: River Channel Improvement and Nature-Oriented Development Plan by Cooperation with A Land Readjustment Project, Proceedings of Conference of the Society of Environmental Conservation Engineering, pp. 239-242, 2002.
- 5) Fukushima, Y. and Uchida, T.: Study of the Ideal State of Waterfront Development of Municipal Rivers on the Case of Minor River in Built-Up Area, Proceedings of 46th Conference for Infrastructure Planning and Management (CD-ROM), 9pp., 2012.
- 6) Fukushima, Y. and Uchida, T.: Posterior Evaluation of the Nature-Oriented Water Amenity Development of Minor River in Built-Up Area – Approach by Questionnaire to Riverfront Inhabitants –, Proceedings of 50th Conference for Infrastructure Planning and Management (CD-ROM), 9pp., 2014.



# Numerical Study on Effect of Edge distance on the Mechanical Behavior after Major Slip of High Strength Frictional Bolted Joints

Hitoshi MORIYAMA\*, Takashi YAMAGUCHI\*\*

(Received October 7, 2016)

## Synopsis

According to the Japanese Specifications for Highway Bridges, the number of bolts of high strength frictional bolted joints is determined by making slip resistance higher than any acting force. Thus, in case of seismic action, the number of bolts increases greatly. To make the recent enlarged joints with economy and structural rationalization, it should be applied to limit state design. Then it's important to investigate the effect bolt arrangement such as end distance, bolt pitch and edge distance on bearing resistance of joints. So, in this paper, FEA was carried out to clarify the effect of edge distance on bearing resistance. Obtained from the results, it finds that deformed bearing limit stress also increased gradually as edge distance increases, then was constant in due course. Thus, it is concluded that the effect of edge distance on bearing stress may be expressed by S-shape curve such as sigmoid function.

**KEYWORDS:** High strength frictional bolted joints, Finite element analysis, Bearing limit state, Bearing stress

## 1. Introduction

According to the Japanese Specifications for Highway Bridges<sup>1)</sup> (hereafter called as JSHB), the number of bolts of high strength frictional bolted joints is determined by making slip resistance higher than any acting force. In case of extremely large loads, such as seismic action and other combination of severe action, the number of bolts increases greatly. To reduce number of bolts rationally, the conventional design method should be improved and moved into limit state design. In our proposed design method, slip resistance is defined as serviceability limit state, and new resistance of bearing force is introduced as the ultimate limit state. Limit state of bearing resistance after major slip should be considered and clarified.

Fig. 1 shows the new bearing limit state, which our research group call it deformed bearing limit state. Deformed bearing limit state is defined by local plastic bolt hole deformation  $\delta_b$ . This state has high structural redundancy because this state is not defined by ultimate strength contrary to conventional bearing resistance such as Eurocode. As plastic deformation of joints is not so much developed in this situation, it should have capacity to equalize local plastic deformations of each bolt hole.

The previous tensile tests<sup>2,3)</sup> were carried out with 1 to 3 bolts to clarify fundamental mechanical behavior after major slip. It is concluded that the bearing limit stress is proportional to the bolt distance and spacing in load direction, such as end distance, bolt pitch. But, edge distance, bolt distance perpendicular to the load direction, hasn't been researched.

This study focuses on the mechanical behavior after major slip of high strength frictional bolted joint with a bolt. FEA were conducted to clarify the influence of edge distance on deformed bearing limit stress.

## 2. Finite Element Analysis

### 2.1 Analysis case

FEA was calculated by Abaqus / Standard 6.13. As shown in Fig. 2, analytical specimen has only one bolt at slip side as well as the previous tensile tests<sup>2)</sup>. In the tensile tests, because of limitation of loading capacity of the loading machine, F10T M16 bolt whose slip resistance is lower than that of F10T M22 bolt, which is used commonly for bridges in Japan, was selected. The ratio of bolt hole diameter  $d_0$  by bolt diameter  $d$  is the same as in case of M22 bolt. So, in this study, bolt diameter and bolt hole diameter are the same as the above sizes.

Table 1 shows the geometric configuration of specimens and considered parameters. As for considered parameters, they are represented as bold-face and blue letters in Table 1 and Fig. 2. Considered parameters were the edge distance and thickness of main plate and splice plates. The edge distance and thickness of splice plates were the same as main plate so as not to be fractured before the fracture of main plate. The end distance

---

\* Student, Doctor Course of Department of Urban Engineering

\*\* Professor, Department of Urban Engineering

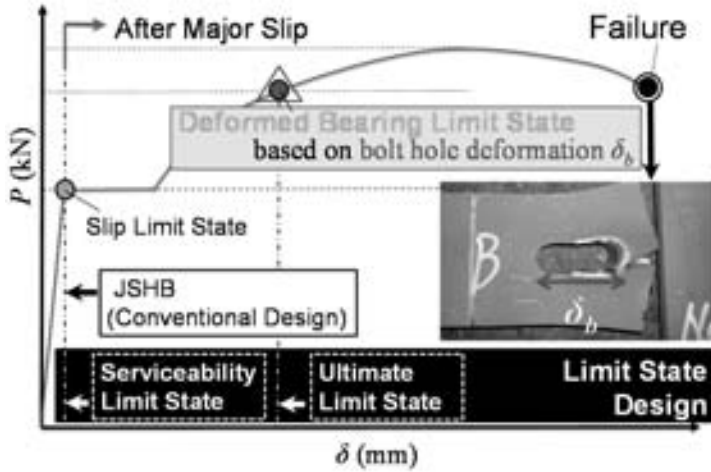


Fig. 1 Proposed Design

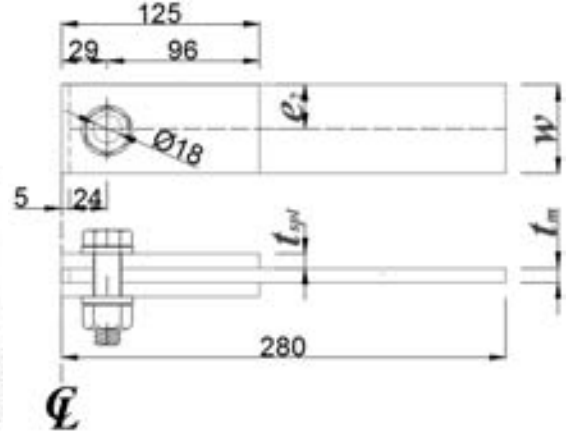


Fig. 2 Configurations of specimens (unit: mm)

Table 1 Geometric Configuration of specimens (**Bold-face** represents considered parameters)

Bolt hole diameter	Bolt diameter	End distance of main plate	End distance / Bolt diameter	Edge distance	End distance / Bolt diameter	Thickness of main plate and splice plate
$d_0$ mm	$d$ mm	$e_1$ mm	$e_1 / d$	$e_2$ mm	$e_2 / d$ mm	$t_m, t_{spl}$ mm
18	16	24	1.5	24, 40, 56, 72, 88	1.5, 2.5, 3.5, 4.5, 5.5	9, 14, 19, 25

of splice plates is large enough to prevent the influence of yield of splice plates to measure the pure bearing resistance of main plate.

The ratio of edge distance  $e_2$  by bolt diameter  $d$  is changed from 1.5 to 5.5 one by one. The thickness is changed to 9, 14, 19, 25mm.

It assume that specimens were fabricated from a single steel plate, steel grade SS400 (nominal material strengths  $\sigma_y = 235 \text{ N/mm}^2$ ,  $\sigma_t = 400 \text{ N/mm}^2$ ). The mechanical property were based on datum of previous study<sup>2</sup>. Used mechanical property in design resistance and FEA are summarized in Table 2. Material property of bolt, nut, and washer are specification values based on the standard of high strength hexagon bolts<sup>4</sup>.

## 2.2 Design Resistance

### 2.2.1. Slip and yield resistance (for serviceability limit state)

Design load carrying capacity are shown in Table 3. Mechanical property was based on Table 2, slip coefficient was 0.45 according to JSHB. As fracture of main plate occurs, Table 3 only shows the resistance of main plate. According to JSHB<sup>1</sup>), the design slip resistance is obtained by from eq. (1).

$$P_{sd} = nm \mu_d N_d \quad (1)$$

where;  $P_{sd}$  is design slip resistance,  $n$  ( $= 3$ ) is the number of bolts,  $m$  ( $= 2$ ) is number of friction surfaces,  $\mu_d$  is design slip coefficient,  $N_d$  is design bolt tensions.

As for net cross-section resistance in JSHB, it is defined as eq. (2).

$$P_{ynd} = (w - d_0)t_m \times \sigma_y = (2e_2 - d_0)t_m \times \sigma_y \quad (2)$$

where;  $P_{ynd}$  is design net cross-section yield resistance,  $w$  is width of main plate,  $d_0$  is bolt hole diameter,  $t_m$  is thickness of main plate,  $\sigma_y$  is yield stress of main plate,  $e_2$  is edge distance of main plate.

### 2.2.2. Ultimate strength and expected failure mode (for ultimate limit state)

As shown in Fig. 4 and Fig. 5, Failure mode of joints is classified into plate failure mode and bolt failure mode. Plate failure mode includes shear failure, bearing failure, and net cross-section failure. In fact, it's reported that the plate failure is sometimes influenced by multiple failure modes. Considering geometrical configuration of specimens in this study, shear failure of bolt and main plate are expected.

Design net cross-section failure resistance in JSHB is obtained by eq. (3)

Table 2 Mechanical property

Name	Reference data	Steel grade	Young's modulus $E$ (N/mm <sup>2</sup> )	Poisson's ratio $\nu$	Yield stress $\sigma_y$ (N/mm <sup>2</sup> )	Tensile strength $\sigma_t$ (N/mm <sup>2</sup> )	Yield strain $\varepsilon_y = \sigma_y / E$ ( $\times 10^{-6}$ )	Yield ratio $\gamma = \sigma_y / \sigma_t$
Main Plate Splice Plates	Material test	SM400	212,600	0.299	301.7	468.3	1419	0.64
Bolt, Nut, Washer	Specification value	F10T	200,000	0.300	900	1000	4,500	0.90

Table 3 Summary of design resistance

Analysis Case	Design slip coefficient $\mu_d$	Design bolt tensions $N_d$ kN	Slip resistance $P_{sd}$ kN	Shear failure resistance of bolts $P_{bd}$ kN	Net cross-section yield resistance $P_{ymd}$ kN	Net cross-section failure resistance $P_{ind}$ kN	Shear failure resistance $P_{ed}$ kN	Expected failure mode
e <sub>2</sub> 24-t9	0.20	106	42	232	82	126	101	Plate Shear failure
e <sub>2</sub> 24-t14					127	197	157	Plate Shear failure
e <sub>2</sub> 24-t19					172	267	214	Plate Shear failure
e <sub>2</sub> 24-t25					227	351	281	Bolt shear failure
e <sub>2</sub> 40-t9					169	261	101	Plate Shear failure
e <sub>2</sub> 40-t14					262	406	157	Plate Shear failure
e <sub>2</sub> 40-t19					356	552	214	Plate Shear failure
e <sub>2</sub> 40-t25					469	726	281	Bolt shear failure
e <sub>2</sub> 56-t9					256	396	101	Plate Shear failure
e <sub>2</sub> 56-t14					398	616	157	Plate Shear failure
e <sub>2</sub> 56-t19					540	836	214	Plate Shear failure
e <sub>2</sub> 56-t25					711	1101	281	Bolt shear failure
e <sub>2</sub> 72-t9					343	531	101	Plate Shear failure
e <sub>2</sub> 72-t14					533	826	157	Plate Shear failure
e <sub>2</sub> 72-t19					724	1121	214	Plate Shear failure
e <sub>2</sub> 72-t25					953	1475	281	Bolt shear failure
e <sub>2</sub> 88-t9					430	666	101	Plate Shear failure
e <sub>2</sub> 88-t14					669	1036	157	Plate Shear failure
e <sub>2</sub> 88-t19					908	1406	214	Plate Shear failure
e <sub>2</sub> 88-t25					1194	1850	281	Bolt shear failure

note: Case name is represented as

edge distance  $e_2$  (24, 40, 56, 72, 88) – thickness  $t$  (9, 14, 19, 25)

$$P_{ind} = (w - d_0)t_m \times \sigma_t = (2e_2 - d_0)t_m \times \sigma_t \quad (3)$$

where;  $P_{ind}$  is design net cross-section failure resistance,  $\sigma_t$  is tensile strength of main plate.

According to Recommendation for Design of Connections in Steel Structures<sup>5)</sup>, Shear failure resistance of main plate is expressed by eq. (4).

$$P_{ed} = 2e_1 t_m \times \frac{\sigma_t}{2} \quad (4)$$

where;  $P_{ed}$  is design shear resistance of main plate,  $e_1$  is end distance.

Bolt shear resistance is expressed by eq. (5).

$$P_{bd} = 2 \frac{\pi d^2}{4} \times \frac{\sigma_{t\_bolt}}{\sqrt{3}} \quad (5)$$

where;  $P_{bd}$  is design bolt shear resistance,  $d$  is bolt diameter,  $\sigma_{t\_bolt}$  is tensile strength of bolt.

### 2.3 FE model

FEM Analysis was calculated by Abaqus/Standard 6.13. Fig. 6 shows the shape of model, and Fig. 7 shows the mesh sizes of model. As shown in Fig. 6, 1/4 parts of the specimen were modeled by considering structural symmetry. Finite elements except those around bolt hole were reduced integration solid elements with 8-nodes. The elements related to bolt hole deformation, which defined deformed bearing limit state, were full integration solid elements with 20-nodes. In addition, it was added to the degree of freedom about hydrostatic pressure considering volumetric locking.

As for coated faying surface related to frictional force, the function “surface-to-surface contact” in Abaqus

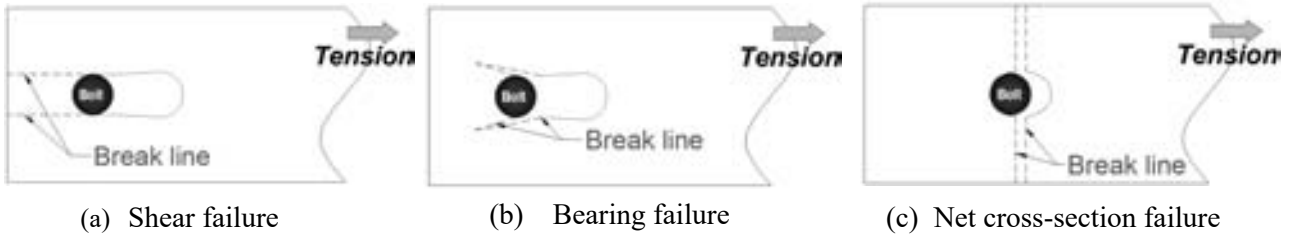


Fig. 4 Plate failure mode

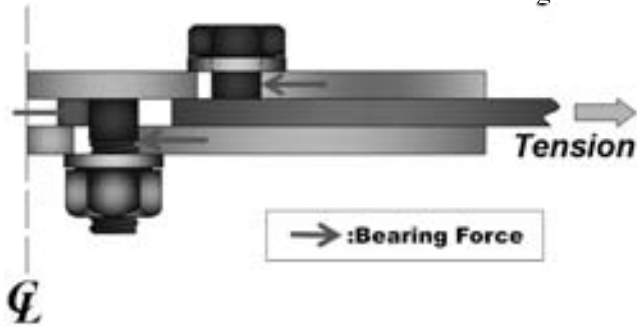


Fig. 5 Bolt shear failure

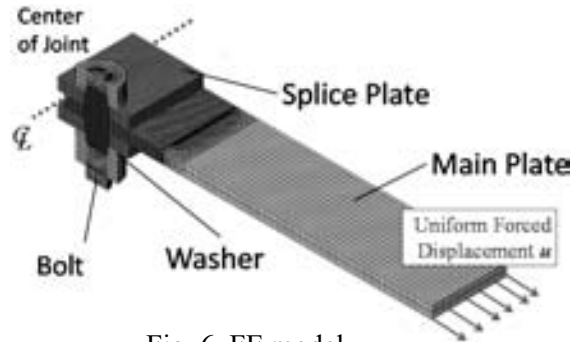


Fig. 6 FE model

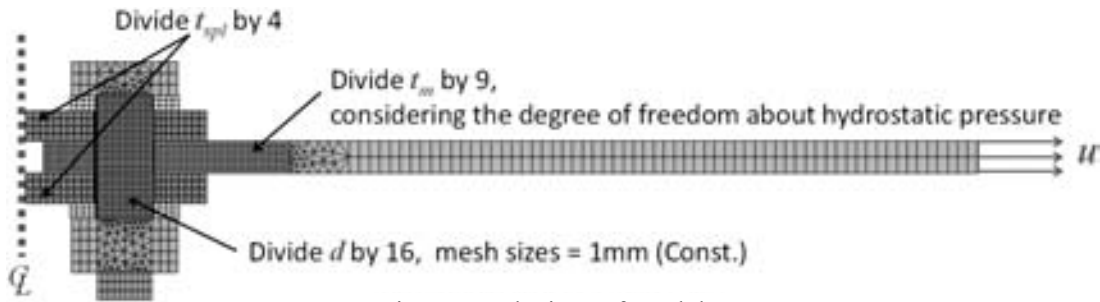


Fig. 7 Mesh sizes of model

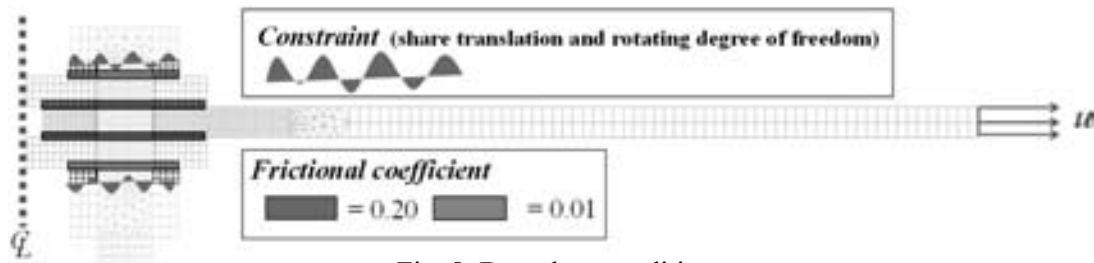


Fig. 8 Boundary conditions

was applied to each faying surface for preventing penetration of elements. Fig. 7 shows the area of boundary condition and applied friction coefficient in each faying surface.

There are two steps in this FEA. Firstly, main plate and splice plates were tightened by high strength bolt. Secondly, forced displacement was applied on the surface at the end of main plate.

Fig. 9 shows Stress-strain curves. Constitutive law of bolt, nut, and washer was based on our research group report<sup>(6)</sup>, the law of connected plate and splice plates was multi-linear model proposed in the specifications<sup>(7)</sup>.

### 3. Effect of edge distance and thickness on bearing behavior

#### 3.1 Load versus forced displacement

Load versus forced displacement curves are shown in Fig. 10. As edge distance increases, the initial stiffness after major slip and

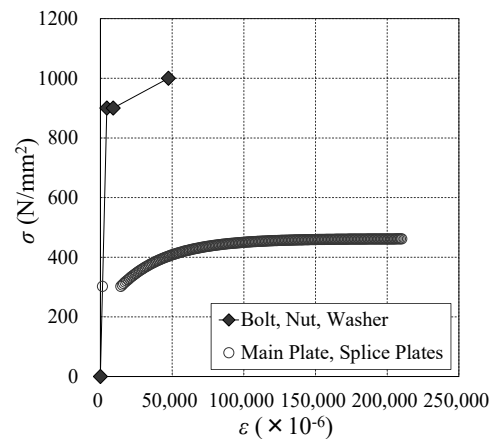


Fig. 9 Stress-strain curves

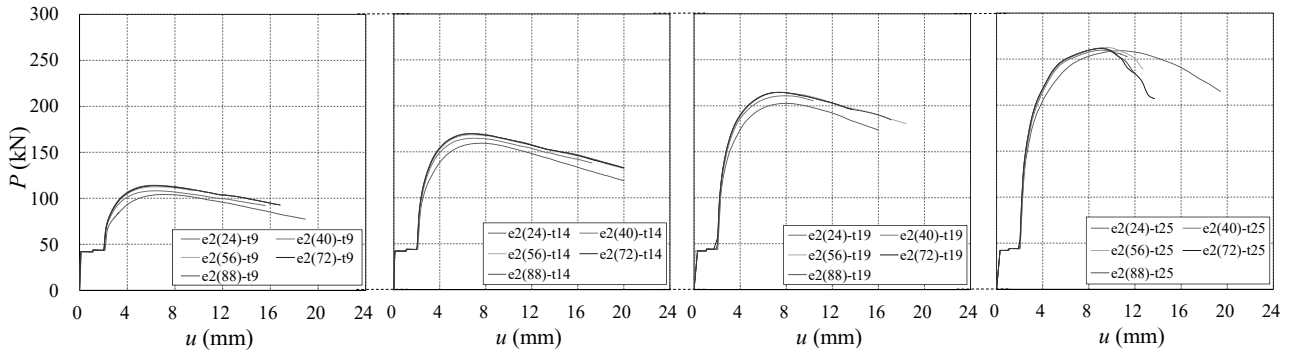


Fig. 10 Load versus deformed displacement

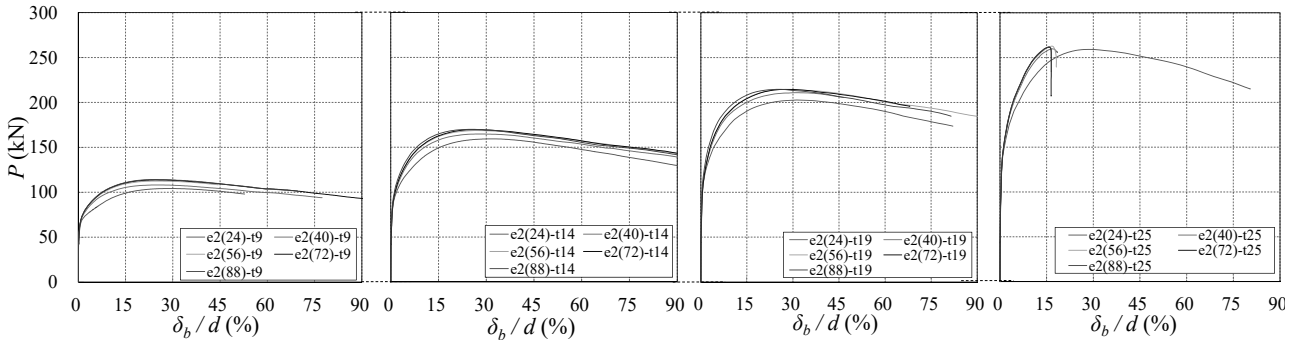


Fig. 11 Load versus bolt hole deformation

ultimate strength also increased. However, ultimate strength wasn't really changed when thickness is 25mm and then bolt shear failure mode occurred. In addition, whether edge distance was more than 24mm in case of  $t_m = 25\text{mm}$ , the strength and deformability after ultimate strength was influenced. In the case "e24-t25", those are kept. This is because thin main plate was deformed farther, and mixed failure mode of bolt shear and plate shear occurred.

### 3.2 Load versus bolt hole deformation

Load versus bolt hole deformation curves are shown in Fig. 11. Definition and measuring method of bolt hole deformation are shown in Fig. 12. For Fig. 11, as well as forced displacement, the same trends was seen in bolt hole deformation when plate shear failure occurred. When bolt shear failure occurred, bolt hole deformation wasn't almost increased and it wasn't increased at all after ultimate strength.

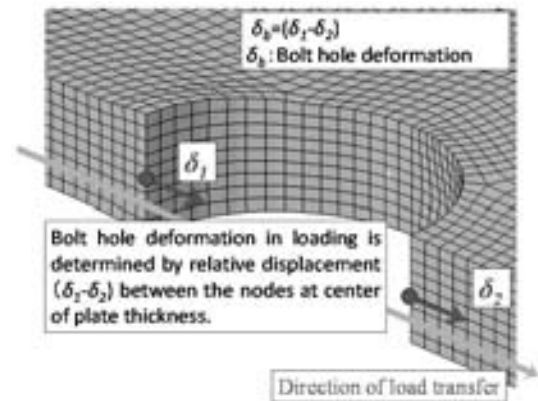


Fig. 12 Definition of bolt hole deformation

### 3.3 Load versus change ratio of bolt tensions

Load versus change ratio of bolt tensions are shown in Fig. 13. As edge distance increases, bolt hole deformation become smaller, then it lead to prevent the decrease of bolt tensions. Comparing specimens which has different thickness, the influence of edge distance on bolt tensions became smaller as thickness increases.

When edge distance was more than 24mm, and thickness was 25mm, the behavior of bolt tensions after ultimate strength was complexed. It's analytical problem, that is, strain was extrapolated and stress wasn't increased in all direction when Mises stress reaches input tensile strength.

### 3.4 Deformed Bearing Limit State

#### 3.4.1. Definition of deformed bearing limit state

Herein is to introduce definition of deformed bearing limit state. It was defined by the variation of bolt hole

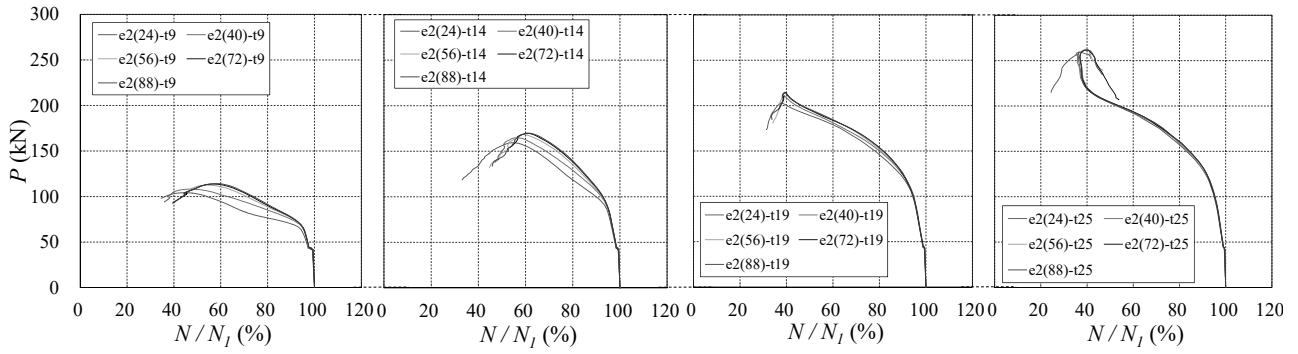


Fig. 13 Load versus change ratio of bolt tensions

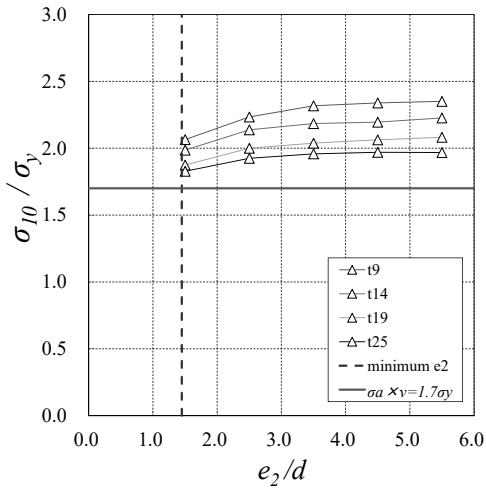


Fig. 14 Effect edge distance on 10% deformed bearing limit stress

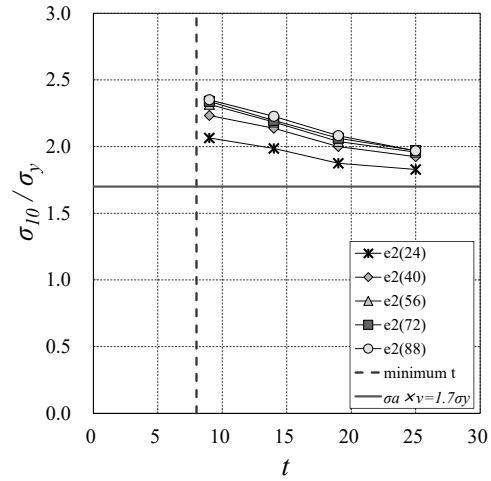


Fig. 15 Effect thickness on 10% deformed bearing limit

deformation. When the ratio of bolt hole deformation by bolt diameter  $\delta_b/d$  reaches 10%, joints becomes 10% deformed bearing limit state. Then, the deformed bearing limit stress is evaluated by nominal bearing stress. For example, consider 10% deformed bearing limit state, it's expressed by eq. (6).

$$\sigma_{10} = \frac{P_{10}}{ndt_m} \quad (6)$$

where;  $\sigma_{10}$  is 10% deformed bearing limit stress,  $P_{10}$  is the load at 10% deformed bearing limit state.

### 3.4.2. Deformed bearing limit stress

Fig. 14 shows the relationship of 10% deformed bearing limit stress and edge distance. The horizontal axis is the ratio of edge distance to bolt diameter, vertical axis is 10% deformed bearing limit stress normalized by yield stress of main plate. The horizontal continuous line is JSHB bearing yield stress ( $= 1.7\sigma_y$ ). The vertical blue dotted lines present the minimum edge distance prescribed in JSHB.

As shown in Fig. 14, even if the minimum edge distance were selected, the 10% deformed bearing limit stress could be higher than  $1.7\sigma_y$ . As edge distance increases, it also increased gradually, then was constant in due course. So, it seems that the effect of edge distance on bearing stress may be expressed by S-shape curve such as sigmoid function.

Fig. 15 shows the relationship of 10% deformed bearing limit stress and thickness. The horizontal axis is thickness of main plate. Vertical axis and the red line are the same as Fig. 14. The vertical blue dotted lines present the minimum thickness prescribed in JSHB.

Fig. 15 shows that 10% deformed bearing stress decreased gradually, as thickness was made large, then was constant in due course. Thus, it imply that the effect of thickness on bearing stress may be expressed by inverse S-shape curve or gentle exponential curve.

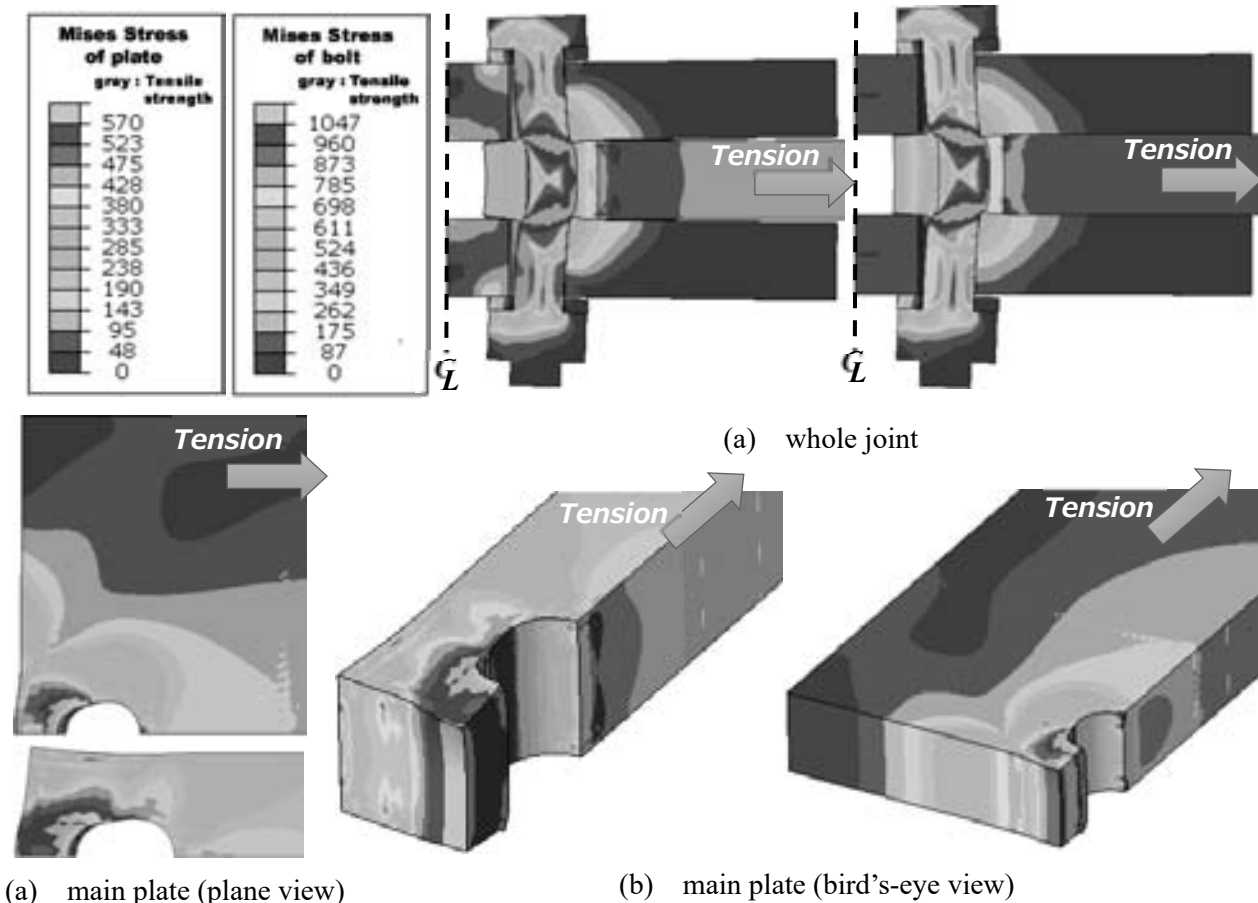


Fig. 16 Distribution of von Mises stress

### 3.5 Failure mode and ultimate strength

Fig. 16 shows the distribution of von Mises stress. The contour diagram is set in true stress in Fig. 16, and gray-colored area depicts that Mises stress reaches tensile strength based on material test.

In this analysis, failure mode were almost predictable results except for case“e<sub>2</sub>24-t25”. As already mentioned in 3.1 section, mixed failure mode of bolt shear and plate shear occurred in that case. Focused on the plastic area of main plate and bolt illustrated by Fig. 16(a) and (b), Mises stress at the end of main plate reached the tensile strength.

## 4. Conclusions

This study focuses on the mechanical behavior after major slip of high strength frictional bolted joint with a bolt. FEA were conducted to clarify the influence of edge distance on deformed bearing limit stress. Conclusions and remarks are as follows;

- 1) As edge distance increases, the initial stiffness after major slip and ultimate strength also increase. However, ultimate strength wasn't really changed and the strength and deformability after ultimate strength couldn't be kept when bolt shear failure mode occurred. As for bolt hole deformation, it wasn't almost increased. But, in the case e<sub>2</sub>24-t25, those are kept because of utilizing the ductility of plate which is higher than that of bolt.
- 2) Even if the minimum edge distance were selected, the 10% deformed bearing limit stress could be higher than 1.7 $\sigma_y$ . As edge distance increases, it also increased gradually, then was constant in due course. So, it seems that the effect of edge distance on bearing stress may be expressed by S-shape curve such as sigmoid function. Contrary to edge distance, 10% deformed bearing stress decreased gradually, as thickness was made large, then was constant in due course. Thus, it imply that the effect of thickness on bearing stress may be expressed by inverse S-shape curve or gentle exponential curve.
- 3) Failure mode were almost predictable results except for case“e<sub>2</sub>24-t25” where mixed failure mode of bolt shear and plate shear occurred. The distribution of von Mises stress about this case shows that Mises stress

at the end of main plate reached the tensile strength. So, design bearing resistance should consider the interaction of various failure modes.

## 5. References

- 1) Japan Road Association, *Specifications for Highway Bridges*, 2012.3 (in Japanese)
- 2) Toda Y., Yamaguchi T., Mineyama Y., Naoe K., “Experimental Study of Bearing Strength of Frictional Bolted Connection Based on Bolt Hole Deformation”, *Journal of Japan Society of Civil Engineers*, Ser. A1, Vol. 70, No.3, pp. 333-345, 2014.
- 3) Moriyama H., Tabata A., Yamaguchi T., Fujibayashi M., “The Basis Examination of Effects of Bolt Pitch and Number of Bolts on Bearing Limit Stress of High Strength Bolted Joint”, *Journal of Japan Society of Civil Engineers*, Ser. A1, Vol. 72, No.1, pp. 119-132, 2016.
- 4) Japanese Industrial Standards Committee, “*Sets of high strength hexagon bolt, hexagon nut and plain washers for friction grip joints*”, JIS B-1186, 2013, (in Japanese).
- 5) Architectural Institute of Japan, “*Recommendation for Design of Connections in Steel Structures*”, 2006, (in Japanese).
- 6) Public Works Research Institute, Osaka City University, “*Report on rationalistic design of high strength bolted friction type joint*”, Cooperative Research Report, No. 428, 2012, (in Japanese).
- 7) Japan Society of Civil Engineers, “*Standard Specifications for Steel and Composite Structures – 2008, IV Seismic Design*”, 2008, (in Japanese).

# **Abstracts of Papers**

## **Published in Other Journals**



***Mechanical Engineering***

**Development of a Solar Assisted High Efficiency Single/Double Effect Absorption Air Conditioning System**

Nobuya NISHIMURA, Tametoshi MATSUBARA, Hiroyuki NAKAGAWA and Yuma YAMAGA  
*Proc. of the 24<sup>th</sup> International Congress of Refrigeration*, ID:382, Yokohama, JAPAN, (2015.8) (on USB).

In order to expand use of solar heat, the authors have been developing a high efficiency solar heat driven cooling system. Also the authors have been conducting long term demonstration tests about a commercial air conditioning system that uses solar energy produced by different three type solar collectors as a heat source of an absorption air conditioning system. As a result, it was demonstrated that the COP in case of combined operation by solar energy and natural gas (exactly city gas) becomes 20 to 40 percent higher than that case of another operation modes. Also, seasonal performances of the system were calculated based on the appearance frequency of the outdoor temperature. Furthermore, in order to obtain mean COP during the air conditioning period, the air conditioning load ratio was sorted by appearance frequency of outdoor temperature. COP takes the maximum value at the air-conditioning load ratio of 30-50% and decreased at both higher and lower air-conditioning load ratios than that.

**Development of an Environment-friendly Disinfection Device for Rice Seed Using Steam Condensation Heat (Part 1) -Selection of Treatment Condition and Its Control Effect-**

Takahiro NODA, Yasuyuki HIDAKA, Hiroyuki IYOTA, Akihiko OCHI, Kazuhiko SAKAI, Tetsuo YABU, Yohei UWAGAKI, Genki MIMURO, Toshiyuki MORIKAWA, Jun ISOTA, Shigeru HOSHINO, Tsutomu ARIE, Toru NAKAMURA, Yuki KARUBE

*Journal of the Japanese Society of Agricultural Machinery and Food engineer*, 77(5), pp.371-383(2015)

In order to increase efficiency and reduce the costs associated with chemical-free, environment-friendly disinfection methods for rice seed, we developed a device with the following purposes: to heat and pasteurize rice seed using steam condensation heat at high temperature during a short time, and to significantly simplify the cooling and drying process compared to the conventional hot water treatment. To select the optimal treatment conditions of the developed device, we focused on the measuring technique of grain temperature, which is used in grain drying engineering. The temperature of rice seed after heating was correlated with the seed germination rate under various heating conditions. We determined a temperature of  $75 \pm 1^\circ\text{C}$  as the optimal condition. This enables a control effect that is equally or more effective against rice seed-borne diseases than the conventional hot water treatment, without the negative effect of excess heat on seed germination.

**Development of an Environment-friendly Disinfection Device for Rice Seed Using Steam Condensation Heat (Part 2) -Development of Operation and Control Method Using Model Predictive Control**

Takahiro NODA, Yasuyuki HIDAKA, Hiroyuki IYOTA, Toru NAKAMURA, Yuki KARUBE

*Journal of the Japanese Society of Agricultural Machinery and Food engineer*, 78(1), pp.95-105(2016)

In a previous paper, we reported on the performance of a device developed for rice seed disinfection. To treat the rice seed such that its temperature after heating ( $T_{\text{fin}}$ ) is  $75 \pm 1^\circ\text{C}$ , the device elicits a control effect equivalent to or more effective than the conventional hot water treatment against rice seed-borne diseases, and without the negative effect of excess heat on seed germination. In this study, we aimed to develop a process control method for  $T_{\text{fin}}$  using Predictive Functional Control. In particular, we aimed to calibrate and validate a prediction model for  $T_{\text{fin}}$  using the process conditions of the device. We created a multiple linear regression model to predict  $T_{\text{fin}}$ , which uses gas humidity, heating time, and other process conditions as predictor variables. The model can predict  $T_{\text{fin}}$  within the standard error of  $0.5^\circ\text{C}$  in the range of  $66.0$  to  $82.7^\circ\text{C}$ . This result indicates that it is possible to apply the model for device operation and control.

**Technical Development of an Environment-friendly Disinfection Method for Rice Seed Using Steam Condensation Heat**

Takahiro NODA, Hiroyuki IYOTA, Yasuyuki HIDAKA, Tamotsu INOUE, Mio YOKOE

*Journal of the Japanese Society of Agricultural Machinery and Food engineer*, 76(6), pp.555-563(2014)

In order to raise efficiency and to reduce the costs associated with chemical-free, environment-friendly disinfection methods for rice seed, we propose a rice seed disinfection method that uses steam heating. This method aims to sterilize the surface of rice seeds with wet heat using steam condensation, and to simplify the

cooling and drying process compared with the conventional hot water treatment. To investigate the applicability of this method and determine the optimal conditions for rice seed disinfection, we examined the effects of heating air temperature, air humidity, air flow rate, and heating time on the sterilization rate and germination rate of rice seeds. We found that the optimal conditions were as follows: heating with an air temperature of 200 °C, and wet bulb temperature of 80 °C, a heating time of 2 s, an air flow rate of 1.8 m/s, and cooling by ventilation with ambient air for more than 60 s. Using these optimal conditions, the newly described disinfection method was as effective against blast and bacterial grain rot as the conventional hot water treatment.

#### **Study on Humidity-Measuring Method Using Wetted Porous Ceramics for High-Temperature Gas**

Kohei MIURA, Taiki MATSUMOTO, Hiroyuki IYOTA, Akihiro MORIKAWA, Tetsuo TSUJIOKA, Michiaki TANAKA and Naoki UESUGI

*Netsu Bussei*, Vol.30, No.1, pp.9-17(2016)

In the process of heat-treating of materials during food processing by employing hot air or high temperature steam, the gas flow temperature, humidity, and pressure significantly affect the processed materials. In this study, we developed a humidity-measuring device that can continuously measure hot air flow above the boiling point. The measuring method is based on the principle of the psychrometer. Porous ceramics processed by injection molding are used as the wetted material for a wet-bulb thermometer. Accuracy is evaluated by using a humidity generator that can generate arbitrary humidity over 100 °C of humid air to superheated steam. The measurements were conducted under gas flow temperatures ranging from 160 °C to 300 °C, and at a gas flow velocity of 3 m/s.

#### **Effect of Heating Capacity of Oven Plate, Heating Ability of Oven, and Duration of Covering the Meat on its Internal Temperature after Oven Cooking**

Kyoko OHISHI, Kimiko ISHIWATA, Sadako TAKASAKI, Keiko NAKAMURA, Yasuko MATSUDA, Hiroyuki IYOTA, Kuniko SUGIYAMA, Shoko SHIBUKAWA

*Journal of Cookery Science of Japan*, 49(1), pp.35-42(2016)

This study analysed the effects of the heating capacity of oven plates and the heating ability of ovens on the internal temperature of meat after oven cooking at 230 °C. The temperature of the samples increased with the increase in the heating ability of ovens. Further, the overall temperature after cooking increased with the increase in the heating capacity of the oven plates, and the time required to attain an internal temperature exceeding 75 °C also increased. As the duration of covering the samples after heating was reduced, the percentage of weight reduction decreased, and the samples became softer. These findings revealed that covering the cooked meat until a maximum internal temperature was attained kept it hygienic and enhanced its taste.

#### **Effects of Cooking and Placement Conditions, Heat Capacity of an Oven Plate, and Thickness of Meat Samples upon Change in their Internal Temperatures after Oven Cooking**

Keiko NAKAMURA, Keiko NAKAMOTO, Chizuru YAGI, Toyoko WATANABE, Kimiko ISHIWATA, Kyoko OHISHI, Sadako TAKASAKI, Yasuko MATSUDA, Junko YAMAGATA, Hiroyuki IYOTA, Kuniko SUGIYAMA, Shoko SHIBUKAWA

*Journal of Cookery Science of Japan*, 49(1), pp.26-34(2016)

The effects of cooking and placement conditions, heat capacity of oven plate, and thickness of the sample on the change of internal temperatures of meat sample after oven cooking were investigated. Internal temperature of the samples with the cover on oven plate after oven cooking maintained over 75 °C for longer time than that of the samples without the cover. Heat capacity of oven plate (weight and area ratio) effected on the 75 °C retention time of the center temperature of the samples. The thickness of samples had almost no effect on using remaining heat. The 75 °C retention time of the center temperature of the samples were predicted with improved calculation model. Calculated times were similar to those obtained from actual measurement, and which confirmed the validity of the heat transfer model.

#### **Effect of Moisture Content on Bubble Formation in Heat Sealing for Plastic Container**

T. INOUE, T. SHIONO, H. IYOTA

*Proc. of 20th International Drying Symposium (IDS 2016)*, C-5-6(7 pages on USB Memory), (7-10 August, 2016, Gifu, Japan)

Heat sealing technology is applied for plastic packaging. Multiple kinds of films are laminated together for barrier characteristics for the permeable component or to adjust stiffness with packaging materials using plastic films and sheets. Heat seal operation is completed by heating the heat-seal material and then immediately cooling it down. "Bubble formation" is one of defects caused by overheating of heat sealing. In the previous study, prevention method of bubble formation is investigated focusing on the relation of melting surface temperature of heat-seal

material and boiling temperature of water inside sample material. In addition, we confirm that bubbling never happen in case of dried material. In this study, an effect of initial moisture content on bubble formation using retort pouches as sample material. The material compositions are, in order of outmost layer / barrier layer / heat-seal material, polyester / nylon / polypropylene. In addition, the mechanism of bubble formation is investigated with the view of “viscous elasticity” and “barrier characteristics” of sample material. Furthermore, we considered the appropriate storage condition of retort pouch for manufacturing.

### **Estimation of Humidity in Drying Chamber from Wet-Material Temperature for Improved Utilization of Superheated Steam**

H. IYOTA, T. INOUE, J. YAMAGATA

*Proc. of 20th International Drying Symposium (IDS 2016)*, P2-39(7 pages on USB Memory), (7-10 August, 2016, Gifu, Japan)

Superheated steam at approximately atmospheric pressure has found increasing applications in industrial and domestic techniques like drying and food processing. The histories of humidity and temperature profiles inside the dryer chamber during heating significantly influence the quality of the processed material. In this study, we propose a modified psychrometric chart for evaluating the dryer characteristics using superheated steam. The steam mole fraction is presented on the ordinate of the chart to enable application to superheated steam. The adiabatic saturation temperature lines are based on a derived approximate expression. We developed a simple method for estimating humidity (steam mole fraction) at high temperatures using a wetted gauze sphere for measuring the wet-bulb temperature, and applied this method to estimate the humidity in the chamber of commercially available steam-convection oven as an example. The results confirmed that the proposed modified chart and the humidity estimate method can be used to visualize the histories of the heating conditions inside the chamber during drying.

### **Development of a Wireless Temperature/Humidity Sensor Node That Can Be Placed on Ovens**

T. Tsujioka, A. Morikawa, K. Kodama, T. Ozaki, H. Iyota

*Abstracts Book of Symposium on Temperature and Thermal Measurements in Industry and Science(TEMPMEKO 2016)*, p56 (June 2016, Zakopane, Poland)

Food processing ovens, including superheated steam convection ovens, are widely used in food factories. They have different distributions of temperature and humidity inside, therefore it is important to measure and analyze them to keep and improve the quality of food products. In mass production phase, the quality depends on each thermal environment of individual ovens in factories through the country, and then fine control by the master operators with special skills is required, even if the laboratory developed and provided complete recipes. If the history of thermal environment around the food can be measured, such special skills might not be necessary. There are many types of ovens, such as batch oven, reel oven, tunnel oven, and so on. So, it is necessary that a sensor node must be stand-alone with wireless transmission technology. Conventional wireless sensor nodes cannot run at high temperature of more than 200 °C. Thus, in this paper, the authors have designed and developed a wireless temperature/humidity sensor node that can be placed next to the food product in the food processing oven. The wireless technology enables real-time measurements of thermal environments, including temperature, humidity, radiation heat, internal temperature of the food products, vibration (acceleration) and pressure. The goal of the development is to achieve downsizing, high accuracy, high reliability such as low wireless transmission loss, wide range operation up to 300 °C, and long-time measurement. For the purpose above, the authors designed the node by using both the humidity sensor based on psychrometer and 920 MHz wireless band. The humidity sensor for high temperature with insulating characteristics has been investigated by the authors in the previous literatures. The 920 MHz wireless band has good properties like long distance transmission, diffracted radiation and small antenna, which are suitable for our node. The authors have implemented its electric circuit on a new small PCB (printed-circuit board) with size of 56 mm by 43 mm. Moreover, a three nested heat-insulating case is also developed for long-time measurement in the oven. The heat insulating material of outer layer is fine ceramics with the thickness of 10mm. Four small ice plates are placed inside the case, as cooling media. The actual dimensions of sensor node are length 130 mm, width 110 mm and height 90 mm. To evaluate performance of operable measurement time, accuracy and reliability, we have examined some experiments to measure the thermal environment in ovens and steamers. The results show that, in the ovens, more than 1 hour measurement time, and lossless wireless transmissions, by using the technique of diversity receiver, can be achieved. In the steamers, measurement time is decreased to about 30 minutes but it is enough time to measure during food processing. The accuracy seems to be also enough but it should be analyzed with the comparison to other sensor devices. We consider that the measurement of weight and surface color of food products is also quite important and it is one of our future works.

### **Development of Psychrometer Using Porous Ceramic Probe for Improved Utilization of Superheated Steam**

H. IYOTA, K. MIURA, H. YOSHIOKA, T. TSUJIOKA, M. TANAKA, N. UESUGI

*Abstracts Book of Symposium on Temperature and Thermal Measurements in Industry and Science (TEMPMEKO 2016)*, p280 (June 2016, Zakopane, Poland)

Utilization of superheated steam (water vapor above boiling point temperature) under approximately atmospheric pressure is gaining popularity in both industrial and domestic food processing applications such as steaming, baking, reheating, and sterilization. In this process, the temperature, humidity, and pressure of the heating media used in the chamber of the food processing machinery are all related to the final quality of the processed food. At the beginning of this process using this type of machinery, the humidity of the heating media decreases because air is mixed into the chamber when the food material is placed in the apparatus. After this beginning process, the humidity starts increasing because steam is supplied to the chamber from a steam generator. The humidity profiles during the process depend on several factors, such as chamber size, performance of the steam generator, chamber sealing conditions, and amount of food. Moreover, this time-dependent humidity profile greatly influences not only the temperature profiles but also the moisture profiles of the food during the process. Therefore, it is required to directly measure the humidity to improve these processes. However, the measuring conditions are extreme in that the temperature inside the chamber may exceed 250 °C and have extremely high humidity levels. Moreover, the sensor(s) may collect residue from the foodstuffs being processed. Therefore, there is no simple device that can measure humidity for an extended duration under these conditions. In this paper, we introduce a device developed for measuring wet-bulb temperature, which consists of a wetted porous ceramic probe with thermocouples and a water retention control system. The measured humidity (steam mole fraction) is calculated from the directly measured wet- and dry-bulb temperatures using the adiabatic saturation line equation on which we previously reported. The equation was further developed to enable its application to temperatures of up to 350 °C and to humidity levels of superheated steam. Accuracy measurements for this device were conducted using a humidity generator to generate humidity levels ranging from that of room air to superheated steam under atmospheric pressure. The cause of any errors and the uncertainties were investigated.

### **Development of Measuring Device Using Porous Ceramic Based on Principle of Psychrometer**

Kohei MIURA, Hiroyuki IYOTA, Taiki MATSUMOTO, Tetsuo TSUJIOKA, Akihiro MORIKAWA, Michiaki TANAKA, Naoki UESUGI

*Proceedings of 24th IIR International Congresses of Refrigeration*, (August 2015, Yokohama, Japan) (on CD-ROM)

Hot air, both dry and moist, has been widely used for heating and/or a reaction atmosphere in a broad range of industrial fields including food processing, material drying, and other heat treatments. In a process that uses hot air and superheated steam, the gas flow temperature, pressure, and humidity inside the treatment chamber have a major impact on the quality of the finished product. However, there is no simple method of measuring humidity that can be used over an extended duration in applications that use superheated steam at temperatures above 100 °C. In this paper, we introduce a device developed for measuring humidity, which consists of a wetted porous ceramic probe with thermocouples, a water retention control system, and computing devices. The measured humidity (steam mole fraction) is calculated from the measured wet- and dry-bulb temperatures using the adiabatic saturation line equation on which we previously reported. The equation was extended to enable its application to temperatures of up to 350 °C and a humidity up to that of superheated steam. Accuracy measurements were conducted with a humidity generator and a gas flow temperature of 200 °C, a gas flow velocity of 3 m/s, and steam mole fraction ranging from that of hot air to that of superheated steam. The cause of any errors was investigated.

### **Color Monitoring Method under High Temperature during Oven Cooking**

Yuji NAKAMORI, Hiroyuki IYOTA, Hideki SAKAI, Taiki MATSUMOTO and Shuhei NOMURA

*Proc. of AIC2015 (Midterm Meeting of the International Colour Association)*, pp.856-860 (May 2015, Tokyo, Japan)

The oven is one of the most popular appliances used for food processing tasks such as heating and baking, both in industry and domestic households. In general, the temperature of the oven chamber is monitored and regulated automatically during the baking process, and automated baking is performed using programmatic control. In this case, the only parameters used are those of time and temperature, without reference to color information. In contrast, when food is cooked manually (i.e. using a frying pan), we intuitively monitor the appearance of food visually, judging whether it is ready or not by its color, without measuring the time and temperature. This is because appearance monitoring in real-time, that is, in-situ color measurement, allows an optimization of the

appearance of food, and provides a result that can be aesthetically appealing. Appearance is in fact one of the most important factors for food consumers. For these reasons, we have developed color monitoring equipment, together with a method for baking in the oven. In our previous study, we reported on an in-situ color monitoring that comprised a halogen light, an optical fiber and a spectrometer, used as a light source and a measuring instrument, respectively. Sliced white bread was used as the sample material. In this study, we investigated this real-time monitoring method using a charge-coupled device (CCD) camera for color detection. We constructed a small oven for our experiments using a conventional home oven as a basis, and examined the monitoring method at a temperature of approximately 200°C. The cooking and previously reported prediction expressions were also used. As we were considering practical usage in the home, infrared heaters installed in a commercially available oven (100 V-600 W-2200 K) were used as the light source. The experimental results demonstrate their applicability for this purpose. Suitable methods for automatically determining the optimal conditions of the monitoring system, allowing for the preferences of users, are also proposed.

#### **Color Measurement of Meat in Cooking under LED Lightings with Different Spectral Distributions**

Akari KAGIMOTO, Risa SHIOMI, Shino OKUDA, Mami MASUDA, Katsunori OKAJIMA, Hideki SAKAI and Hiroyuki IYOTA

*Proc. of AIC2015 (Midterm Meeting of the International Colour Association)*, pp.877-880 (May 2015, Tokyo, Japan)

We measured the colors of meat during cooking under the standard illuminant D65 and several LED lighting conditions which differ in the spectral power distribution. First, we prepared three kinds of minced meat, beef, chicken and pork, which were shaped into 2 cm cubes. Each cube of the minced meats was baked with an oven at the temperature of 200 °C. We made a spherical dome for measuring average chromaticity values of an object in the condition of no shadow. The dome equipped fluorescent lamps of the standard illuminant D65 and two kinds of LED lamps: RGB LED lamps and white LED lamps. We measured the average chromaticity of the top surface of minced meat cubes at a raw stage and 22 cooking stages using a two-dimensional luminance colorimeter under eight lighting conditions in the spherical dome. According to the results, the chromaticity values gradually decreased with the increase in cooking time under all lighting conditions. It was also shown that the color appearance while the beef has been cooked depends on the lighting conditions.

#### **Numerical Analysis of Contact Line Dynamics Passing over a Single Wettable Defect on a Wall**

Yasufumi YAMAMOTO (Kansai Univ.), Shohei HIGASHIDA, Hiroyuki TANAKA, Tatsuro Wakimoto, Takahiro ITO (Nagoya Univ.), and Kenji KATOH

*Physics of Fluids*, Vol. 28, 082109, pp. 1-17 (2016)

In this study, the dynamics of a contact line passing a single defect, which was represented by a locally wettable part (whose static contact angle is less than the other part, namely, chemically heterogeneous and physically flat part), was analyzed using numerical simulations employing the front-tracking method and the generalized Navier boundary condition. We observed that the contact line was distorted with a logarithmic shape far from the defect; however, the distortion was dependent on the wall velocity. The apparent (averaged) dynamic contact angle of the wall with a defect was evaluated using a macroscopic energy balance. The apparent dynamic contact angles estimated from the energy balance agree well with the arithmetic averaged angles obtained from the present simulations. The macroscopic energy balance is useful to consider the effect of heterogeneity or roughness of the wall on the relation between the dynamic contact angle and contact line speed.

#### **Effect of Wetting Phenomenon on Oscillation of Liquid Column in a U-shaped Tube**

Tatsuro WAKIMOTO, Tomonori SUWA, Yoshiaki UEDA (Setsunan Univ.), Kenji KATOH and Manabu IGUCHI (Osaka Electro-Communication Univ.)

*Advanced Experimental Mechanics*, Vol. 1, pp. 58-62 (2016)

An experimental and theoretical study was conducted to investigate the liquid metal oscillation in a U-shaped tube. Since the surface tension of liquid metal is quite large as compared with usual liquids and its tangential component is dependent on the contact angle appearing at both ends of the liquid column, the characteristics of oscillation should be strongly influenced by the static and dynamic wetting behavior of the triple phase contact line. However, the past studies had considered only the inertia, viscous and gravitational force to analyze the dynamics of the oscillation. Here in this study, we proposed an equation of motion in which the hysteresis and velocity dependence of contact angles are properly taken into consideration to estimate the effect of surface tension. In the experiment, the angular frequency  $\omega_d$  and damping ratio  $\zeta$  of oscillation were measured for ethylene glycol-water solution and mercury in U-shaped glass tubes, as well as the dynamic contact angles dependent on the contact line

velocity. The experimental results were approximated well by the theoretical model proposed here and it is inevitable to include the wetting effect to accurately estimate  $\omega_d$  and  $\zeta$  for mercury.

### **Simultaneous Water Entry of Many Poorly-Wetted Solid Spheres**

Manabu IGUCHI (Osaka Electro-Communication Univ.), Akira SONOMOTO (Osaka Electro-Communication Univ.), Yoshiaki UEDA (Setsunan Univ.), Ryoji TSUJINO (Setsunan Univ.), Tatsuro WAKIMOTO and Kenji KATO

*Advanced Experimental Mechanics*, Vol. 1, pp. 219-223 (2016)

There are two types of desulphurization processes in the steelmaking industry: the KR process and injection process. In the former process refining agents such as CaO particles are initially placed on the bath surface and then dispersed in the bath using an impeller. Meanwhile, the refining agents in the latter process are introduced into the bath with a carrier gas such as Ar and N<sub>2</sub>. The efficiency of the two processes depends strongly on the dispersion pattern of the agents in the bath. The agents are usually poorly wetted by molten metal. The main objective of this water model study is to make clear the wettability effect of the agents on their dispersion pattern in the bath. As a first step, many poorly-wetted spheres were simultaneously introduced into a water bath. The dispersion patterns of the spheres were observed with a high-speed camera.

### **The Influence of Wettability on Simultaneous Water Entry of a Pair of Spheres**

Shota OTANI (Osaka Electro-Communication Univ.), Yoshiaki UEDA (Setsunan Univ.), Manabu IGUCHI (Osaka Electro-Communication Univ.), Ryoji TSUJINO (Setsunan Univ.), Tatsuro WAKIMOTO and Kenji KATO

*Advanced Experimental Mechanics*, Vol. 1, pp. 224-230 (2016)

As a fundamental study of enhancing the efficiency of the current desulphurization process, water model experiments were carried out to understand the behavior of refining agents entering a molten iron bath. The agents such as CaO particles are usually poorly wetted by molten iron and carried into the bath together with a carrier gas. The penetration depth and residence time of the agents in the bath is strongly responsible for the efficiency. The main objective of this water model study is to make clear the wettability effect of the agents on their entry in the bath. A pair of spheres of different wettability and different diameters was simultaneously introduced into a water bath. An air cavity was formed under every experimental condition. Its scale was mainly dependent on the larger sphere. The penetration depth of larger sphere was favorably compared with an analytical solution for a single sphere penetrating into a water bath.

### **Removal of Fine Particles on a Wall by High-Speed Air Jet Ejected from Cavity Nozzle (Optimization of Nozzle Shape)**

Tatsuro WAKIMOTO, Atsushi NAKAGAWA, Kazuhiko SOEMOTO (Shinco Co. Ltd.) and Kenji KATO

*Proc. of the 9th International Conference on Multiphase Flow*, USB-memory, No. 169, 3 pages (2016)

We developed a cleaning device which removes fine particles adhering on a wall by a high-speed impinging jet with strong fluctuation. In general, it is difficult to remove micrometer-sized particles by a simple air jet because they strongly adhere to the surface by van der Waals forces and remain immersed in a viscous sublayer. In this study, strong velocity and pressure fluctuations are added to the jet using a nozzle with triangular cavities to overcome the problem. In order to clarify the removal mechanism by the fluctuated jet and optimize nozzle shape, we considered hydrodynamic drag and local pressure gradient forces acting on a sphere particle and evaluated removal moment by numerical simulation. The removal moment evaluation for various types of nozzle revealed that the nozzle shape with the shortest throat length and one step cavity is the best for removal due to the strongly enhanced removal moment by velocity and pressure fluctuations.

### **Front-tracking Simulation of Electrowetting Droplet Manipulation**

Yasufumi YAMAMOTO (Kansai Univ.), Ryoko OTOMOTO (Kansai Univ.), Takahiro ITO (Nagoya UNIV.), Tatsuro WAKIMOTO and Kenji KATO

*Proc. of the 9th International Conference on Multiphase Flow*, USB-memory, No. 172, 6 pages (2016)

In this study, droplet manipulation utilizing electrowetting is numerically reproduced by the front-tracking method and the generalized Navier boundary condition. Voltage dependency of wettability is accounted by Young-Lippmann equation. Capacitors' series connection model can reproduce the droplet behaviors as being trapped between positive and negative electrodes and transported with electrode's switching, similar as observed in the experiments. The effect of switching frequency and voltage are evaluated and compared with experimental data. Furthermore, the effects of droplet properties (size, viscosity, and surface tension) are examined.

### **Development and Evaluation of a 300L Class Constant Temperature Bath for Temperature Sensors**

Shoichiro BABA (JAMSTEC), Kazuaki YAMAZAWA (AIST), Jun TAMBA (AIST), Tatsuro WAKIMOTO and Kenji KATO

*Transactions of the JSME*, Vol. 81, No. 832, pp. 1-14 (2015) (in Japanese)

Japan Agency for Marine-earth Science and Technology (JAMSTEC) has been developing a 300 L class constant temperature bath to calibrate temperature sensors monitoring ocean water temperatures. This system consists of a constant temperature bath which requires the temperature stability within  $\pm 1$  mK. The purpose of this study is to investigate experimentally the performance and accuracy of the 300 L class constant temperature bath. To evaluate the temperature distribution within the bath, we first evaluated the measurement uncertainty of a 12 channel thermometer to ensure the meaningful results with temperature differences at 1 mK level. Results using this 12 channel thermometer and another reference thermometer indicated that although temperature stability of the 300 L class constant temperature bath was within  $\pm 1$  mK at each measuring point, the total calibration time was longer than the targeted time. In order to elucidate the reason for this, the transient temperature distribution was measured with the 12 channel thermometer, and it was found that a region within the bath takes a longer time to reach stability. Moreover, measurement of the velocity distribution within the bath using Particle Image Velocimetry showed that a lack of turbulent flow in the bath caused this delay.

### **Primary Mechanism on the Determination of the Dynamic Contact Angle on an Accelerating Contact Line**

Takahiro ITO (Nagoya Univ.), Kenta YOKOI (Nagoya Univ.), Yoshiyuki TSUJI (Nagoya Univ.), Kenji KATOH, Tatsuro WAKIMOTO and Yasufumi YAMAMOTO (Kansai Univ.)

*Japanese Journal of Multiphase Flow*, Vol. 29, No. 5, pp. 421-459 (2016) (in Japanese)

Estimation of the contact angle on a moving contact line is one of the important factors for the prediction of the liquid surface geometry contacting with solid. In this study the dynamic contact angle on an accelerating vertical glass rod is investigated both experimentally and numerically to elucidate the effect of the acceleration of the contact line. The experiment was held by using ethylene-glycol and its aqueous solution as test fluid. The measured contact angle in the transient state clearly deviated from that for the steady state, depending on the acceleration of the rod. Numerical simulation shows that the acceleration and the gravity terms in the momentum equation, which are relatively remarkable in macroscopic scale, are not responsible for such deviation in the contact angle. Rather, the dependence of the microscopic contact angle on the acceleration, estimated with the viscous bending model, should be the primary factor on the deviation of the contact angle.

### **Numerical Simulation of Dynamic Wetting of a Solid Sphere by GNBC-Front-Tracking and Immersed Boundary Methods**

Ryoko OTOMO (Kansai Univ.), Yuya KITA (Kansai Univ.), Yasufumi YAMAMOTO (Kansai Univ.), Takahiro ITO (Nagoya Univ.), Tatsuro WAKIMOTO and Kenji KATOH

*Japanese Journal of Multiphase Flow*, Vol. 29, No. 5, pp. 443-450 (2016) (in Japanese)

Dynamic wetting of a solid sphere has been simulated numerically. We have developed the model for the description of the moving contact lines on curved solid surfaces by combining the GNBC-Front-tracking method and the immersed boundary method. The model was applied to the simulation of a quasi-static penetration of a water-repellent sphere into the water. As a result, the shape of the interface for different wettability is in good agreement with the previous experimental results. The residual bubble volume was evaluated under the different sphere size, static contact angle, and penetrating velocity conditions. The present results show a similar trend to the experimental and theoretical ones that the water-repellent sphere has a larger bubble since it incorporates more volume of air into the water, indicating the dynamic wetting of the sphere surface can be reproduced by the model.

### **Control of Droplet Movement on an Inclined Wall by Difference of Wettability**

Kenji KATOH, Hiroki TAMURA, Eriko SATO and Tatsuro WAKIMOTO

*Japanese Journal of Multiphase Flow*, Vol. 29, No. 5, pp. 451-459 (2016) (in Japanese)

Recently it is strongly demanded to manipulate a liquid droplet in lab-on-chip or micro reactors used in chemical engineering devices. This study concerns the control of the movement of liquid droplet on an inclined plate, using the difference of wettability caused by the chemical structure change of a polymer which is resulted from the irradiation of ultraviolet rays. The behavior of droplets was carefully observed experimentally when it enters into the irradiated area having an oblique boundary to the moving direction. Considering the surface tension acting on the perimeter with different contact angles, the movement of droplet was analyzed theoretically. The calculated results approximate well the actual behavior of droplet. Then we proposed a geometric pattern of irradiated area in which the droplet could be moved linearly with a constant angle to the gravitational direction. The experimental

observation shows that the droplet behavior was successfully controlled to be moved along on the line of geometric pattern.

### **Dryout of Falling Liquid Film Flowing on a Plate and a Vertical Cylinder**

Kenji KATOH, Tatsuya YAMASHITA, Yoshiaki ISO (IHI Corp.), Tatsuro WAKIMOTO and Mariko SAGA(IHI Corp.)

*Japanese Journal of Multiphase Flow*, Vol. 29, No. 5, pp. 467-476 (2016) (in Japanese)

The disappearance or dryout region observed in liquid film flowing on an inclined wall (50mm width) was investigated experimentally. The film surface profile on the cross section vertical to the flow direction was measured by the needle contact method to investigate the effect of side wall on the critical Weber number  $We_c$  at which the dryout region shrinks to disappear. The results show that there exists a minimum film thickness observed at few milli-meters from the side wall, which is much smaller than that of Nusselt's theory. To avoid such effect of side wall on the dryout phenomenon, the critical Weber number  $We_c$  was measured for the film flowing on the vertical plate (200mm width) without side wall and on the outer wall of vertical cylinder. The experimental results show that  $We_c$  is much smaller than that for the inclined plate. A simple theoretical consideration was conducted to consider the force balance including the gravitational force at the edge of the dryout region in order to expect the critical Weber number. The results approximate well the tendency of the experimental results dependent on the advancing contact angle and viscosity.

### **Residual Bubble Volume Left on a Spherical Particle Plunging into Molten Metal**

Tatsuro WAKIMOTO and Kenji KATOH

*Japanese Journal of Multiphase Flow*, Vol. 30, No. 3, pp. 274-281 (2016) (in Japanese)

Surfaces of common solids are hardly wet with molten metal. When such a hardly wetted object plunges into liquid, a cavity is formed behind the object. Furthermore, a residual bubble is left on the object after the break of the cavity. In metal refining process, the residual bubble attached to desulfurizing agents such as CaO particles interferes with deep immersion and desulfurization reaction. In this report, the volume of the residual bubble was theoretically estimated for the quasi-static and quite slow (but finite speed) immersion of a sphere as a reference condition. We calculated it from a simple energy minimum principle considering the interfacial energy and liquid potential energy. The calculated volumes can approximate fairly well the measured results for two kinds of contact angles of  $115^\circ$  and  $162^\circ$

### **Prediction of Quasi-Static Deformation of Gas-Liquid Interface by Energy Minimization Principle**

Tatsuro WAKIMOTO and Kenji KATOH

*Journal of JSEM*, Vol. 16, No. 1, pp.28-35 (2016) (in Japanese)

Wetting phenomenon has close relation to processes of condensation, evaporation, material production, separation, adhesion and so on. Therefore the performance of many industrial machines is determined by the wetting phenomenon. The wettability between solid and liquid is evaluated by contact angle, and main parameters governing the wetting phenomenon are the contact angle and surface tension. However, wetting phenomenon involving the move of contact line and liquid surface is very complicated, and is difficult to analyze. In this report, we propose a method to analyze the wetting phenomenon based on the principle of energy minimization considering the effect of the interfacial energy including the wetting behavior and the liquid potential energy. We predicted the volume of liquid droplet detaching from a sphere and residual bubble volume formed behind a sphere plunging into liquid based on this method. The predicted values agreed well with experimental values. This method is convenient and simple method to analyze the complicated wetting phenomenon.

### **Measuring Method of Dynamic Surface Tension of Surfactant Solutions**

Tatsuro WAKIMOTO and Kenji KATOH

*Journal of JSEM*, Vol. 16, No. 3, pp. 207-214 (2016) (in Japanese)

The surface tension of surfactant solution varies temporally when a fresh gas-liquid interface appears and the surfactant molecules are diffused to be trapped at the interface. In this study, a new method is proposed to measure the dynamic surface tension of surfactant solutions. The laminar jet injected from a horizontal capillary tube is used for the methods. First the momentum balance of capillary jet is discussed between surface tension, gravitational force, pressure and inertial force. The ordinary differential equation of motion is solved numerically by the simple Runge Kutta's method to obtain the profile of jet trajectory. The dynamic surface tension can be determined to coincide the theoretical jet trajectory with the measured profile. The method was actually applied to measure the dynamic surface tension of several kinds of surfactant aqueous solutions. The results agreed well with those measured by usual methods. The proposed method was also applied to estimate the growth rate of unstable

wave appearing on a planer sheet of surfactant solutions. The calculated wave amplitudes calculated from the measured dynamic surface tension approximate well the wave characteristics observed experimentally.

### **Performance of Very Small Robotics Fish Equipped with CMOS Camera**

Yang Zhao, Masaaki FUKUHARA, Takahiro USAMI, and Yogo TAKADA

*Robotics*, Vol. 4, Issue 4, pp.421-434 (2015).

Underwater robots are often used to investigate marine animals. Ideally, such robots should be in the shape of fish so that they can easily go unnoticed by aquatic animals. In addition, lacking a screw propeller, a robotic fish would be less likely to become entangled in algae and other plants. However, although such robots have been developed, their swimming speed is significantly lower than that of real fish. Since to carry out a survey of actual fish a robotic fish would be required to follow them, it is necessary to improve the performance of the propulsion system. In the present study, a small robotic fish (SAPPA) was manufactured and its propulsive performance was evaluated. SAPPA was developed to swim in bodies of freshwater such as rivers, and was equipped with a small CMOS camera with a wide-angle lens in order to photograph live fish. The maximum swimming speed of the robot was determined to be 111 mm/s, and its turning radius was 125 mm. Its power consumption was as low as 1.82 W. During trials, SAPPA succeeded in recognizing a goldfish and capturing an image of it using its CMOS camera.

### **Making a Three-dimensional Map in Complicated Environment by Using a Bridge Inspection Robot with a Laser Range Finder**

Naoto IMAJO, Tomoki TAJIRI, Mikiji KASHINOKI, and Yogo TAKADA

*Transactions of the JSME*, Vol.82, No.833 (2016) (in Japanese).

Many infrastructures such as bridges and tunnels had been constructed in various parts of Japan during the high economic growth period. They need periodic inspection because they are aging. Inspecting them by inspector is both costly and time-consuming. There is a strong demand for practical bridge inspection robots to reduce the costs and times. The inspection robot running autonomously on the bridge needs to determine moving route and to estimate self-position. The robot must have a three dimensional map of the bridge to take these actions. This paper proposes a method of making a three-dimensional occupancy grid map of the large scale infrastructure where the inspector cannot go easily such as an underside of the bridge. A bridge inspection robot equipped with magnets had been developed in present study. We attached a measuring device which consists of a small 2D laser range finder and a servo motor. Experiments were conducted to make the 3D map by using the robot. The robot climbed to target position on the wall without falling although it was equipped with the measuring device which is heavy. Moreover, the robot can make the 3D occupancy grid map and the map can be useful to inspect bridges.

### **Strategy for Lowering Electric Power Consumption Concerning Vertical Wall Inspection Robot HORNET**

Yuhei TOKURA and Yogo TAKADA

*Transactions of the JSME*, Vol.82, No.835 (2016) (in Japanese).

Many structures such as bridges, buildings, tunnels and dams had been constructed during the high economic growth period in Japan. The deterioration of these structures has become a big social problem. The maintenance method which finds the minor damages on the structures is important for the life extension of many structures before the progress of deterioration advances. When the inspections become frequent, the huge cost is needed. Robots are said to be useful for the management and maintenance of many old structures because the conventional method will intensify the strains on economy. In this study, we have created a flying robot HORNET with tilt-rotors and two wheels. HORNET can move on a vertical wall keeping a constant distance between the robot and a wall. Then, it is very easy and safe to control the robot manually. In addition, the electric power consumption of HORNET can be smaller than hovering robot like drones because HORNET can hang on wall with claws of the wheels. We have examined the effects of the state of wall surface and the tilt angle of rotor surface on the electric power consumption of HORNET. According to the experimental results, it has been confirmed that the electric power consumption is reduced when the state of wall surface is rougher and the tilt angle of rotors is more parallel to the ground. It is possible to become a practicable wall inspection robot by adding the improvement to HORNET.

### **Practical Applications of HORNET to Inspect Walls of Structures**

Yuhei TOKURA, Kohei TOBA, and Yogo TAKADA

*Journal of Robotics and Mechatronics*, Vol. 28, No. 3, pp.320-327 (2016).

During the high economic growth period in Japan, the development of new infrastructures was promoted and numerous bridges and buildings were constructed. Currently, the walls of bridges and buildings are inspected

manually. This manual inspection process is expensive and time-consuming, and inspectors may be placed in dangerous situation. In this study, a robot that moves stably on a wall while maintaining a distance from the wall was developed to enable low-cost, safe inspection. Several characteristics of the robot were measured, and the possibility of using the robot in practical applications was assessed based on the measurement results.

### **Examining the Relationship between Blood Flow Velocity and Movement of Erythrocytes in a Capillary using Laser Doppler Velocimetry**

Shunsuke AKIGUCHI, Hiroki ISHIDA, Yogo TAKADA, Tsunenobu TERANISHI, Tsugunobu ANDOH, and Tadashi HACHIGA

*IEEJ Transactions of Electrical and Electronic Engineering*, Vol. 11, Issue 4, pp. 451-456 (2016).

In this study, we consider the relationship between red blood cell velocity and the movement of erythrocytes. Many velocimeters measure fluid velocity by tracking the movement of tracer particles present in the fluid. Generally, in laser Doppler velocimetry, seeding particles of suitable density and size are added to the fluid being measured, but this is not possible for in vivo measurements. In the case of blood, erythrocytes are used as the tracer particles. It is unclear, however, whether the velocity of erythrocytes reflects actual red blood cell velocity. Therefore, we compare the results of flow velocity distribution measurements of blood in the ear vessels of mouse and in water containing tracer particles in a serpentine flow channel. Results of the comparison indicate that the velocity of moving erythrocytes does not correspond exactly to the velocity of the blood. The difference is due to the changes in the fringe pattern under the skin. However, we consider that it is possible to measure red blood cell velocity in any direction using these fringe changes. Moreover, we confirm that results obtained using the proposed method match those obtained using other methods.

### **In vivo visualization method by absolute blood flow velocity based on speckle and fringe pattern using two-beam multipoint laser Doppler velocimetry**

Tomoaki KYODEN, Shoji NARUKI, Shunsuke AKIGUCHI, Hiroki ISHIDA, Tsugunobu ANDOH, Yogo TAKADA, Noboru MOMOSE, Tomotaka HOMAE, and Tadashi HACHIGA

*Journal of Applied Physics*, Vol.120, 084701 (2016).

Two-beam multipoint laser Doppler velocimetry (two-beam MLDV) is a non-invasive imaging technique able to provide an image of two-dimensional blood flow and has potential for observing cancer as previously demonstrated in a mouse model. In two-beam MLDV, the blood flow velocity can be estimated from red blood cells passing through a fringe pattern generated in the skin. The fringe pattern is created at the intersection of two beams in conventional LDV and two-beam MLDV. Being able to choose the depth position is an advantage of two-beam MLDV, and the position of a blood vessel can be identified in a three-dimensional space using this technique. Initially, we observed the fringe pattern in the skin, and the undeveloped or developed speckle pattern generated in a deeper position of the skin. The validity of the absolute velocity value detected by two-beam MLDV was verified while changing the number of layers of skin around a transparent flow channel. The absolute velocity value independent of direction was detected using the developed speckle pattern, which is created by the skin construct and two beams in the flow channel. Finally, we showed the relationship between the signal intensity and the fringe pattern, undeveloped speckle, or developed speckle pattern based on the skin depth. The Doppler signals were not detected at deeper positions in the skin, which qualitatively indicates the depth limit for two-beam MLDV.

### **Frequency Dependence of Nonlinear Viscoelastic Relaxation in Glassy Poly(methyl methacrylate) (PMMA) Subjected to Constant-Speed Stretching**

Shin'ya YOSHIOKA, Masayuki TOYODA and Mariko IWAMOTO

*Nihon Reoroji Gakkaishi (J. Soc. Rheol., Jpn)*, Vol.44, pp.81-87 (2016). (in Japanese)

Variation of complex shear modulus of glassy poly(methyl methacrylate) (PMMA) was monitored during uniaxial stretching to investigate the frequency dispersion of strain-induced nonlinear relaxation. With increasing strain  $\epsilon_n$ , the storage modulus  $G'$  decreased to a steady value appearing at post-yield range of strain accompanied by a marked increase of the loss modulus  $G''$ , indicating that glassy structures changed into more unstable ones due to stretching. The variation of the moduli was more remarkable when the timescale of observation, *i.e.* frequency  $f$  of dynamic measurement, was closer to that of deformation, *i.e.* strain rate  $\dot{\epsilon}_n$ . Increment of  $G''$  as a function of  $\epsilon_n$  was identical independently of  $\epsilon_n$  when observed at a fixed condition of  $\alpha = \dot{\epsilon}_n/f$ . This observation indicates that  $\beta$  relaxation is not altered by imposition of large strain and that the frequency dispersion of the nonlinear stress relaxation is determined by relative distance from the timescale of deformation and the amount of imposed strain.

Relationships between  $\Delta G'$ , decrement of  $G'$ , and  $\epsilon_n$  were not superposable at a fixed  $\alpha$ , because of negative  $\epsilon_n$  dependence of  $\Delta G'$  in the post-yield regime. This presumably shows that strain aging, structural relaxation of the strain-induced unstable glassy structures under finite stress, occurs during deformation.

#### **Damage Behavior in CFRP Laminates containing Fiber Discontinuities of Different Sizes**

Hayato NAKATANI, Yu NAGATA, Ryuta KITAMURA, Akira MATSUBA, Yousuke KOUNO and Shinji OGIHARA

*Transactions of the JSME (in Japanese)*, Vol. 81, No. 831 (2015), DOI:10.1299/transjsme.15-00226

Mechanical properties and damage onset stress in 24 or 25-ply unidirectional CFRP laminates that contain different thicknesses and gap lengths of fiber discontinuity are investigated by tensile testing and analytical model. Same damage behavior, as with previously reported, that interlaminar delamination between fiber continuous and discontinuous plies follows after crack initiation at the edge of the discontinuous fibers is observed even if thinner and longer gap of the fiber discontinuities are introduced. It has been shown that the laminates with long gap fiber discontinuity show higher stress of crack onset than that with short gap, and the crack onset stress decreases with the number of the discontinuous plies. A similar trend can be seen for the onset stress of the interlaminar delamination though no delamination has been observed in the short and long gap 1-ply and long gap 2-ply discontinuous laminates. The crack onset stress is evaluated by representing the energy release rate with crack initiation by using stress change in shear-lag model. Due to the fact that the relation between the number of discontinuous plies and crack onset stress can be predicted for both short and long gaps of fiber discontinuity by assuming a certain value of critical energy release rate, it is shown that the crack onset behavior is not affected by thickness and gap length of the fiber discontinuity. Another analytical model with an assumed critical energy release rate has successfully predicted the delamination onset stress regardless of sizes of fiber discontinuities by applying the exact thicknesses of continuous and discontinuous plies. By comparing the predicted delamination onset stress and fracture stress of the laminates, it is concluded that two and more fiber discontinuous plies can affect the overall damage behavior of the laminates.

#### **Damage Behavior in Quasi-isotropic CFRP Laminates with Small Fiber Orientation Angle Mismatch**

Nurul Nabihah A. HAMID, Hayato NAKATANI and Shinji OGIHARA

*Mechanical Engineering Journal*, Vol. 3, No. 1 (2016), DOI:10.1299/mej.14-00422

The use of carbon fiber reinforced plastic (CFRP) has contributed in producing light-weighted and strong aircraft structures. However, the low impact resistance of CFRP makes it easier for internal damages to occur. By using thin-ply prepreg with thickness of less than 0.05 mm, laminates with smaller differences in fiber orientation angle and with the same thickness as the conventional laminates can be formed. This study investigates and compares the mechanical properties and damage behaviours between quasi-isotropic laminates with fiber orientation angle mismatch of 45 degrees (45QI) and laminates with small fiber orientation angle mismatch of 15 degrees (15QI). Both laminates are loaded in tension in 0, 7.5, 15 and 22.5 degrees. Low velocity impact tests are also conducted. From tensile testing, 15QI laminates shows more isotropic properties in strength than 45QI. Damages were observed by using microscopic and X-ray images. Crack propagation in width direction can be prevented in 15QI laminates. From low velocity impact testing, we understand that impact responses are not depending so much on the fiber orientation angle mismatch. In terms of internal damage, 15QI laminates has smaller delaminated area near the impact point compared to 45QI laminates.

#### **Effect of Distribution Media on Resin Impregnation Behavior during VaRTM Process**

Hayato NAKATANI, Kentaro ADACHI and Katsuhiko OSAKA

*Journal of the Society of Materials Science, Japan*, Vol. 65, No. 8 (2016), pp. 548-554.

Multipoint measurements for resin flow during VaRTM process are carried out by using embedded fiber optic sensors to evaluate the effect of a resin distribution medium which is incorporated on a fiber preform as a surface layer on resin impregnation behavior. By simultaneously infusing epoxy resin into two glass fiber preforms with or without a distribution medium that are separated by a plastic film, resin amount impregnated through in-plane flow and out-of-plane flow via the distribution medium are compared. It has been indicated that resin amount impregnated through the out-of-plane flow via the distribution medium is found to be dominant especially for thinner fiber preform and be constant at each evaluated region of the resin flow. Numerical calculation for resin impregnation during the VaRTM process is also performed using coefficient of permeability both in in-plane and through-the-thickness direction in the fiber preform. The simulated resin amount impregnated through out-of-plane flow via the distribution medium is found to be constant during the impregnation process due to a constant slope angle of flow front, and be comparable with the experimental results.

### **Damage Behavior Evaluation on Thermoplastic Resin Based CF/PA6 Laminate Composites with Fiber Discontinuity**

Koyo KOYANAGI, Ryuta KITAMURA, Akira MATSUBA, Yosuke KOUNO, Hayato NAKATANI, Takenobu SAKAI and Shinji OGIHARA

*Journal of the Society of Materials Science, Japan*, Vol. 65, No. 8 (2016), pp. 561-566.

The tensile tests of the unidirectional CFRP laminate composites (CF/PA6) with fiber discontinuity were performed, and mechanical properties were obtained. The laminate stacking sequence of the specimens is  $[0_{24}]$ , and the specimens have fiber discontinuity of 6, 12 and 18 layers. And, the damage growth behaviors were investigated by microscopic observation and acoustic emission (AE) monitoring. Furthermore, the delamination onset stresses were predicted by the simple analysis model. As a result, the stress-strain curves showed nonlinear behavior, and nonlinear starting points became early with increase of the fiber discontinuity layers. It is found that the initial damage of the specimen was the crack between fiber discontinuity end/resin interface by microscopic observation and AE monitoring. And, the delamination between continuous/discontinuous ply around the resin occurred. After that, the resin at the fiber discontinuity was broken at the time of maximum applied stress, then the delamination grew extensively in the specimen, finally the specimens were broken. In addition, the delamination onset stresses were predicted by analysis model using energy release rate, and these stresses were almost agree with experimental values.

### **Non-Destructive Damage Assessment in CFRP/Ti Laminates by Synchrotron Radiation Laminography**

Hayato NAKATANI, Kentaro KAJIWARA, Koichi AKITA and Shinji OGIHARA

*Proc. 14<sup>th</sup> Japan International SAMPE Symposium and Exhibition*, Kanazawa, Japan, Dec. 6-9, Paper No. 0055 (USB Memory) (2015).

One of the possibilities to ensure reliability of the carbon fibre composite structure that is susceptible to impact loading can be an introduction of Fibre-Metal Laminates (FMLs). FMLs are hybrid laminates that consist of alternately stacked layers of metal sheets and fibre-reinforced polymers. It is well-known that there is a difficulty in non-destructive assessment of damage in FMLs using laboratory radiography or X-ray computed tomography since transmission of X-ray in width direction of the FMLs cannot be achieved. Synchrotron radiation laminography at SPring-8 is employed to assess low velocity impact damage in CFRP/Ti laminates as one of the most interested FMLs. During computed laminography bright X-ray is irradiated to an object with the axis of rotation inclined at an angle and thus it is suitable for the laterally extended geometry of composite laminate plates. It is confirmed how each damage mode in the CFRP/Ti laminates can be imaged by synchrotron radiation laminography by using model specimens that contain artificially induced damage. Then 3-dimensional imaging of impact-induced damage where each damage mode shows complex distribution is demonstrated and that is to our knowledge a novel result.

### **Damage Suppression in UD-CFRP with Fibre Discontinuity by Interlaminar Toughening using Polyamide Mesh**

Hayato NAKATANI, Tatsuya IMAMURA and Katsuhiko OSAKA

*Proc. 17<sup>th</sup> European Conference on Composite Materials*, Munich, Germany, June 26-30, Paper ID TUE-1\_SEV\_3.03-08 (2016).

A fiber discontinuity in fibre reinforced composite laminates may act as a source of stress concentration that induces damage onset. A mesh made of thermoplastic polyamide (PA) as an interlayer is inserted between fiber continuous and discontinuous plies in order to suppress an interlaminar cracking in unidirectional CFRP laminates that contain fiber discontinuity at the centre of the laminates. It is experimentally shown that by inserting PA mesh the onset stress of the interlaminar crack increased significantly. The stabilized end notched flexure (ENF) tests using strain gages are carried out to obtain a continuous R-curve of the mode II interlaminar fracture toughness  $G_{II}$ . By inserting the PA mesh  $G_{II}$  for initial crack growth  $G_{IIC} = 1.60 \text{ kJ/m}^2$  and for during crack propagation  $G_{IIR} = 3.82 \text{ kJ/m}^2$  can be achieved. It is also indicated that an analytical model suggested here that incorporates energy release rate during the interlaminar crack growth can predict the stress of the interlaminar crack onset for different number of discontinuous plies by applying  $G_{IIR}$  not  $G_{IIC}$  for both the laminates with and without PA mesh.

### **Shortening in Process Time of VaRTM and Impact Damage Suppression for Fibre-Metal Laminates by inserting Polyamide Mesh**

Yosuke HANDA, Yasunori MATSUI, Hayato NAKATANI and Katsuhiko OSAKA

*Proc. 13<sup>th</sup> International Conference on Flow Processes in Composite Materials*, Kyoto, Japan, July 6-9, FPCM-13\_extended\_abstract\_57.pdf (USB Memory) (2016).

During VaRTM (Vacuum assisted Resin Transfer Molding) process a distribution medium, which is incorporated

on fibre preform as a surface layer, is utilized in order to shorten impregnation time of resin by increasing the flow rate of resin and is removed after molding. In this study, the distribution medium is replaced by a thermoplastic polyamide mesh, and the mesh is still remained in aluminum alloy / GFRP fibre-metal laminates after VaRTM process. The mesh is expected not only to improve the resin flow but also to suppress impact damage such as interfacial debonding between aluminum alloy and GFRP layers in the fibre-metal laminates after molding. Multipoint measurements for resin flow during VaRTM process are carried out by using embedded fibre optic sensors. It is confirmed that the polyamide mesh inserted between aluminum alloy and GFRP in the hybrid laminates as an interlayer increased the flow rate during the impregnation of resin by VaRTM process. Drop weight impact tests have been also conducted to show that impact responses are improved and the aluminum alloy / GFRP interfacial debonding is suppressed by the polyamide mesh inserted. From these results it is shown that improvements in both resin flow and impact damage suppression can be achieved by the single action of inserting the polyamide mesh.

### **Resin Impregnation Behavior in Thick Carbon Fibre Composite with a Corner during VaRTM Process**

Hayato NAKATANI, Kentaro ADACHI and Katsuhiko OSAKA

*Proc. 13<sup>th</sup> International Conference on Flow Processes in Composite Materials*, Kyoto, Japan, July 6-9, FPCM-13\_extended\_abstract\_56.pdf (USB Memory) (2016).

VaRTM process impregnates resin to fibre preform using difference in pressure between atmosphere and vacuum, and attracts attention as a method to mold FRP at relatively low cost. However, resin impregnation behavior in the fibre preform is not understood exactly, and the formation of dry spots is a problem to be avoided. It is said that a resin distribution media which is incorporated on the fibre preform as a surface layer has a significant effect on resin impregnation behavior by adding resin flow in out-of-plane direction. In this study, multipoint measurements for resin flow during VaRTM process for thick CFRP plates with corner are carried out by using embedded fibre optic sensors to understand the resin impregnation behavior in the preform. In addition, numerical calculation considering the resin amount impregnated via the resin distribution media during the VaRTM process for thick CFRP plates with corner is also carried out. The experimental and numerical results indicate that the resin arrival time at the bottom of corner is extremely late. However, resin flow rate obtained by experiment is much lower than that obtained by simulation at some points. It seems that resin amount impregnated via the distribution media is reduced because of the small cross-section area in the media for the resin flow due to the bending at the corner. Some gaps between each carbon fibre fabric which are produced due to waviness at the corner can also interrupt the out-of-plane resin flow in the fibre preform.

### **Technological Trend in Past 50 Years and New Technology of Scanning Electron Microscopy in Materials Characterization**

Y. KANEKO

*Special Issue for the 50<sup>th</sup> Anniversary the JSPS 136<sup>th</sup> Committee on Future-Oriented Machining (FORM)*, pp.154-157 (2016) (in Japanese)

Recent technological trends in scanning electron microscopy (SEM) and related technologies are reviewed. First, fundamentals of SEM imaging was explained from the viewpoint of secondary electron intensity that was sensitive to the angle between incident beam and surface. Then, the author described the channeling contrast and the z-contrast, where intensities of backscattered electrons were imaged. In addition to the imaging technique based on the scanning of incident beam, the electron backscatter diffraction (EBSD) technique enabling orientation analysis was introduced. A grain boundary map and a (100) pole figure of a severely-deformed nickel were presented. Finally, the SEM images of dislocations that were obtained by electron channeling contrast imaging (ECCI) were presented. In particular, availability of the ECCI technique was emphasized for the dislocation observation of fatigued materials.

### **Controlling strength and ductility: Dislocation-based model of necking instability and its verification for ultrafine grain 316L steel**

A. VINOGRADOV, I.S. YASNIKOV, H. MATSUYAMA, M. UCHIDA, Y. KANEKO, Y. ESTRIN

*Acta Materialia*, Vol. 106 pp.295-303 (2016).

A phenomenological dislocation-based approach is proposed to account for the necking phenomenon during tensile deformation of metals and alloys. The critical strain corresponding to the onset of tensile instability is predicted in a simple explicit form based on the Kocks-Mecking dislocation kinetics approach. The model strongly suggests that uniform elongation is controlled primarily by the rate of dislocation recovery. The role of the strain rate sensitivity in stabilizing uniform plastic flow is also elucidated. Model predictions are found to be in excellent agreement with experimental data obtained for ultrafine grained 316L steel produced by severe plastic

deformation. The approach presented provides general ques for designing materials with enhanced ductility, including ultrafine grained and bulk nanostructured metals and alloys. The proposed recipe is based on microstructural control of the rate of dynamic recovery of dislocation.

### **Computational simulation of macroscopic non-uniform deformation depending on the size of microscopic heterogeneous structure using second-order homogenization method**

M. UCHIDA and Y. KANEKO

*Proceedings of IWACOM-III*, p. 17 (2015), in CD-ROM

In the second-order homogenization method, microscopically displacement functions for macroscopic strain gradient are introduced into the conventional first-order homogenization method. Then, changes in the potential energy by macroscopic strain and strain gradient are used to solve the macroscopic boundary problem. In the second-order homogenization method, displacement field given to the representative volume element (RVE) changes with the size of RVE, homogenized macroscopic constitutive equation depends on the length scale of microscopic heterogeneous structure. The effect of crystalline grain size on the macroscopic non-uniform deformation of polycrystalline materials was evaluated by FEM simulation based on the rate-form second-order homogenization method. The conventional crystalline plasticity theory was applied to represent the scale-independent deformation behavior of microscopic crystalline structure. Numerical simulations of uniaxial tension of curved gage section specimen were performed to give the non-uniform deformation on the macroscopic region. Polycrystalline microstructures with different grain sizes were given to all Gauss integration points on macrostructure. Higher deformation localization in the macrostructure was observed when a larger tensile deformation was given to the curved gage section specimen with smaller crystal grain. This size effect on the non-uniform deformation of the polycrystalline materials was caused by non-uniform deformation in microstructure, which was strongly characterized by the macroscopic strain gradient and the size of the microstructure.

### **Scale-dependent multiscale modeling of deformation behavior of polymer foam using rate-form second order homogenization method**

M. Uchida and Y. Kaneko

*Symposium proceedings of the 22<sup>nd</sup> International Symposium on Plasticity and Its Current Applications*, (2016), in USB memory

Polymer foam, in which the microscopic voids are introduced in the polymer matrix, is one of ultra-lightweight solid material. Although the polymer foam shows many great functions such as heat resistance, toughness, electrical insulation etc., a lower strength of the material restricts the use of them as structural materials. To improve the strength of the polymer foam, a design of microscopic material structure consisting of void and polymer matrix is indispensable. It requires the accurate prediction of the micro- to macroscopic deformation behavior depending on the size, volume fraction and distribution of microscopic voids and mechanical property of polymer matrix. In the present study, a scale-dependent micro- to macroscopic computational model of the polymer foam is proposed using the rate-form second-order homogenization method. In the rate-form second order homogenization method, a microscopic characteristic displacement function for macroscopic strain gradient is added to the conventional first order homogenization method. Then, a procedure to solve a macroscopic boundary problem is established based on the principle of virtual work in the macroscopic scale represented by the microscopic characteristic displacement function. Using the proposed second-order homogenization method, computational simulations of micro- to macroscopic deformation behaviors of polymer foam FEM models having different sizes and volume fractions of the void were performed. In this study, macroscopic strain gradient and its work conjugate higher order stress were used to evaluate the evolutions of plastic work under the macroscopic non-uniform deformation. From the simulation results, higher deformation localization was seen in the polymer matrix when the size of the void was large, and it causes scale-dependent macroscopic non-uniform deformation behavior. Basically, the deformation behavior predicted by proposed homogenization model was qualitatively and quantitatively similar to that predicted by the full-scale model.

### **Multiscale modeling approach about degradation of mechanical properties for polymeric materials**

M. Kudo, J. Takahashi, T. Yamamoto, M. Uchida and Y. Tomita

*Symposium proceedings of the 22<sup>nd</sup> International Symposium on Plasticity and Its Current Applications*, pp. 91-93 (2016), in USB memory

Multiscale modeling method for the degradation behavior of fiber-reinforced polymer composites is developed in the present study. Degradation of the matrix polymer is modeled by using coarse-grained molecular dynamics (MD). Then, microscopic characteristic of molecular chain distribution by MD simulation is introduced into the

mesoscopic constitutive equation as a craze consisting voids and fibrils. FEM simulations are performed to examine the degradation of macroscopic mechanical properties of glass fiber-reinforced polymer (GFRP). Reduction in tensile strength against the aging time has good agreement with the experimental results.

### **Effect of welded part geometry and electrical conductivity on the crack evaluation of pipe-flange welded part by the direct-current potential difference method**

N. TADA, M. UCHIDA, M. KOSAKA and T. MUROMOTO

*Journal of JSNDI*, Vol. 65 pp. 340-347 (2016)

When the crack of the pipe-flange welded part is evaluated by the direct-current potential difference method (DC-PDM), the result is affected by the weld metal geometry and electrical conductivity. In this paper, a pipe-flange welded component was modeled and the detection of the crack by DC-PDM was discussed based on the results of electric field analyses using the finite element method. In the analysis, the depth of crack and the geometry and electrical conductivity of the weld metal were varied. In all conditions, increase in potential difference by the crack took the maximum value near the boundary of the flange and weld metal, and it was high enough for crack detection. Although the potential difference was affected by the weld metal geometry and electrical conductivity, the normalized potential difference was well correlated with the crack depth ratio, and the relation was formulated by a cubic equation. Based on the equation, the crack depth was evaluated successfully for all conditions with different weld metal geometries and electrical conductivities.

### **The Graph-Theoretic Minimum Energy Path Problem for Ionic Conduction**

Ippei KISHIDA

*AIP Advances*, 5(10), p.107107 (2015)

A new computational method was developed to analyze the ionic conduction mechanism in crystals through graph theory. The graph was organized into nodes, which represent the crystal structures modeled by ionic site occupation, and edges, which represent structure transitions via ionic jumps. We proposed a minimum energy path problem, which is similar to the shortest path problem. An effective algorithm to solve the problem was established. Since our method does not use randomized algorithm and time parameters, the computational cost to analyze conduction paths and a migration energy is very low. The power of the method was verified by applying it to  $\alpha$ -AgI and the ionic conduction mechanism in  $\alpha$ -AgI was revealed. The analysis using single point calculations found the minimum energy path for long-distance ionic conduction, which consists of 12 steps of ionic jumps in a unit cell. From the results, the detailed theoretical migration energy was calculated as 0.11-eV by geometry optimization and nudged elastic band method. Our method can refine candidates for possible jumps in crystals and it can be adapted to other computational methods, such as the nudged elastic band method. We expect that our method will be a powerful tool for analyzing ionic conduction mechanisms, even for large complex crystals.

### **Study on Tomographic Micro-Visualization of Erythrocyte Velocity distribution using High Frequency Modulated Low Coherence Interferometer (Optical Coherence Doppler Velocigraphy)**

Ryohei NISHINO, Souichi SAEKI, Suguru MISHIMA, Minoru YOSHIYAMA, Atsusi SHIBATA, Yudai YAMAGUCHI

*Eighth Asian-Pacific Conference on Biomechanics*, USB-memory, PS8-16, pp.365

Rheological behavior of interstitial fluid in epidermal tissue, including blood micro-circulation, can vary skin mechanics in micro scale, i.e. visco-elasticity. New growth in the micro-vascular network around cancerous tissue can be typically observed, i.e. angiogenesis and lymphangiogenesis, which should decide the proliferation and metastatic spreading of cancer cells. Therefore, an in vivo quantitative diagnosis of blood velocity is quite necessary to clarify their properties of skin care and cancerous tissue. In this paper, we propose OCDV (Optical Coherence Doppler Velocigraphy), which is a method of tomographic micro-visualizing Erythrocyte fluid velocity using a high frequency modulated low coherence interferometer. The tomographic detection of modulated Doppler frequency can determine Erythrocyte velocity profile within tissue. The detection of Doppler frequency, depending on blood velocity, was constructed on the signal processing of Hilbert transform. The proposed OCDV system was validated by measuring the fluid velocity of Intralipid solution (2%) and red blood cell suspension (HCT 40%) in micro channel. As a result, Hilbert transform has further advantages in the accuracy as well as sensitivity, even with a rapid scanning system than short time FFT. Erythrocyte velocity distribution of the RBCs' suspension was observed to be plug flow distribution according to Casson fluid, which is different from that of Newtonian intralipid solution. It was, therefore, concluded that OCDV system could offer tomographic blood velocity in micro-circulation having rheological properties of red blood cells, which was suggested to be an effective modality as in vivo tomographic diagnosing tool of blood flow velocity profiles in tissue.

### **Micro-Tomographic Study on Viscoelastic Behavior of articular cartilage using Dynamic Optical Coherence Straingraphy**

Hiroki NAKAYAMA, Souichi SAEKI, Kiichi HASEGAWA, Mitsuhiro IKEBUCHI, Nobuo NIIMI, Yoshihito TSUKAHARA

*Eighth Asian-Pacific Conference on Biomechanics*, USB-memory, PS4-10, pp.290

Articular cartilage has an important role for improvement of joint sliding and relaxation of the load impact, but there is no potential of self-healing itself without a blood supply. Many of the elderly are predisposed to develop osteoarthritis (OA). So, an OA diagnosis in the earlier stage has been being required, because its appropriate medical treatment has never been established exhaustively in addition to self-healing tissue properties. However, even the latest imaging modalities, e.g. X-ray and MRI, is quite difficult to diagnose the early OA due to insignificant morphological and physiochemical changes. In this study, taking account of the most essential characteristics of tissue degeneration in OA, i.e. mechanical properties, we have developed a non-invasive micro-tomographic visualizing system of viscoelastic properties in articular cartilage. This is namely Dynamic OCSA (Optical Coherence Straingraphy) composed of Optical Coherence Tomography (OCT) and a mechanical loading devise. Proposed Dynamic OCSA can discriminate mechanical propertied from continuous OCT images, which should contain huge hidden information as dynamical behavior of deformed cartilage by a mechanical loading devise. This technique is based on the speckle tracking algorithm, which is composed mainly of the recursive cross-correlation and the sub-pixel analysis, e.g. upwind gradient method and image deformation method. These are applied continuously to the synthetic OCT images, then can provide temporal and spatial distribution of not only deformation velocity but also strain rate. This was experimentally applied to comparatively both normal cartilages and cartilages degenerated by the enzyme treatment. Consequently, the strain rate was observed to be spatially localized within the superficial tangential zone. Additionally, the attenuation of time-varying strain rate was visualized. There appeared to be the significant increase in attenuation with increasing the treatment time. Consequently, it was concluded that Dynamic OCSA can non-invasively offer spatially and temporally dependent biomechanical properties as strain rate tomography, and could employ as an in vivo diagnosing technique of the early OA for Micro-Mechanical Biopsy.

### **Study on Micro-tomography of Temperature using FEM-based Inverse Analysis applied to Optical Coherence Straingraphy**

Ryuki KUNIMOTO, Daisuke FURUKAWA, Souichi SAEKI

*12th World Congress on Computational Mechanics (WCCM XII), 6th Asia-Pacific Congress on Computational Mechanics (APCOM VI)*, USB-memory, pp. 1290

Recently, it is quite necessary to perform the optimum thermal management and design of electronic devices, microscopically and non-destructively. Optical Coherence Tomography (OCT) has been improved as a biomedical diagnostic modality. This can tomographically visualize a spatial variation field of refractive index inside tissue at 1 to 10 micrometer resolution. In this study, non-destructive and tomographic micro-visualizing system of temperature is proposed, namely Optical Coherence Thermography (OCTH). This is composed of FEM-based inverse analysis as well as tomographic detection technique of thermal deformation from OCT speckle images, i.e. Optical Coherence Straingraphy (OCSA) [1]. OCSA is based on the speckle tracking algorithm, which is composed mainly of the recursive cross-correlation and the sub-pixel analysis. This can provide the 2-dimensional displacement vector distribution with further accuracy, by means of the sub-pixel analysis, e.g. upwind gradient method and image deformation method. So, the accuracy of tomographic detection can attain 0.2 micrometer deformation. OCTH is based on FEM-based inverse analysis using tomographic deformation vector field data obtained by OCSA. Inverse analyzing region of interest is set arbitrarily on OCT images, which is discretized to finite elements in consideration of FEM model such as material properties, e.g. Young's modulus, Poisson's ratio and thermal expansion coefficient. A global element equation subjected to thermal expansion can be built under 2-dimensional plane stress and deformation boundary problems. By interpolating tomographic deformation vectors to every nodes, temperature variation can be solved as a FEM-based inverse analysis due to given material properties. Moore-Penrose pseud inverse matrix, mainly defined by shape functions and element discretization, is used selectively to estimate the temperature variation field as a direct inverse analysis. The absolute temperature variation can be calculated from temperature calibration by local measurement. In order to validate OCTH, the numerical experiment was carried out using simulated OCT images constructed by both Monte Carlo simulation and FEM thermal stress analysis. FEM analysis was conducted using a chip embedded board model, in which a silicon CPU and a copper wire were embedded as heat sources in the both side and filled with an epoxy seal. As shown by Fig. 2. OCTH can tomographically visualize high and low temperature distribution around heat sources and the center of sealing material, respectively. This is agreed well with FEM results qualitatively, as a result of

accuracy verification, OCTH can visualize temperature tomography at the micrometer scale with suppressed 6.5% error, i.e. 7.5 degree C. OCTH can provide experimentally and non-destructively micro tomography of temperature distribution with high accuracy, taking no account of dynamic boundary condition.

**Power Electronics**

**Determination of band structure at GaAs/SiC heterojunctions**

Jianbo LIANG, Sae SHIMIZU, Manabu Arai (New Japan Radio Co. Ltd.), and Naoteru SHIGEKAWA

*ECS Trans.* 75 (9) 221 [7 pages] (2016).

The effects of thermal annealing process on the interface in p<sup>+</sup>-GaAs/n-4H-SiC heterojunctions fabricated by using surface-activated bonding (SAB) were investigated. It was found by measuring their current-voltage (*I-V*) characteristics that the reverse-bias current and the ideality factor were extracted to be  $7.57 \times 10^{-7}$  A/cm<sup>2</sup> and 1.33, respectively, for the junctions annealed at 400 °C. The flat-band voltage obtained from capacitance-voltage (*C-V*) measurements was found to be 1.29 eV, which is almost consistent with the turn-on voltage extracted from *I-V* characteristics. These results suggest that the SAB-based GaAs/4H-SiC heterojunctions are applicable for fabricating high-frequency power devices.

**Ultra-Thick Metal Contact Fabrication Using Surface Activated Bonding**

Jianbo LIANG, Katuya HURUNA, Moeko MATSUBARA (Toyo Aluminum K. K.), Marwan DHAMRIN (Toyo Aluminum K. K.), Yositaka NISHIO (Toyo Aluminum K. K.), and Naoteru SHIGEKAWA

*ECS Trans.* 75 (9) 25 [8 pages] (2016).

We successfully bonded aluminum foils to Si substrates to fabricate p-Si/Al, n-Si/Al, p<sup>+</sup>-Si/Al, and n<sup>+</sup>-Si/Al junctions by surface activated bonding (SAB). The effects of the annealing temperature process on the electrical properties of the junctions were investigated by measuring their current voltage (*I-V*) characteristics. It was found that the leakage current of the reverse bias of n-Si/Al junctions was improved and the *I-V* characteristics of p-Si/Al revealed excellent linearity properties after the junctions annealing at 400 °C. The interface resistance of p<sup>+</sup>-Si/Al, and n<sup>+</sup>-Si/Al junctions decreased with increasing annealing temperature and decreased to 0.021 and 0.032 Ω·cm<sup>2</sup> after the junction annealing at 300 and 400 °C, respectively. These results demonstrated that thick metal Ohmic contact in devices could be realized by SAB.

**Fabrication and characterization of Si/4H-SiC interfaces by surface activated bonding**

Jianbo LIANG, Manabu ARAI (New Japan Radio Co. Ltd.), and Naoteru SHIGEKAWA

*Extended Abstracts of 2016 EMN Surface and Interface Meeting, Kuala Lumpur*, pp. 63-64 (2016).

**Effects of Ar beam irradiation on Si-based Schottky contacts**

Shokei HISAMOTO, Jianbo LIANG, and Naoteru SHIGEKAWA

*Extended Abstracts of 2016 IEEE International Meeting for Future of Electron Devices, Kansai (IMFEDK)*, pp. 40-41 (2016). DOI: 10.1109/IMFEDK.2016.7521671

Effects of Ar beam irradiated during the surface activated bonding process on n-Si and p-Si based Schottky barrier diodes (SBDs) were investigated by atomic force microscope measurements. Changes in the electrical characteristics of SBDs were attributed to the variation in Schottky barrier heights due to the Ar beam irradiation.

**Electrical Characteristics of SAB-based n<sup>+</sup>-n Ge/4H-SiC Heterojunctions**

Sho MORITA, Takuya NISHIMURA, Jianbo LIANG, and Naoteru SHIGEKAWA

*Extended Abstracts of 2016 IEEE International Meeting for Future of Electron Devices, Kansai (IMFEDK)*, pp. 74-75 (2016). DOI: 10.1109/IMFEDK.2016.7521694

Effects of Ar beam irradiated during the surface activated bonding process on n-Si and p-Si based Schottky barrier diodes (SBDs) were investigated by atomic force microscope measurements. Changes in the electrical characteristics of SBDs were attributed to the variation in Schottky barrier heights due to the Ar beam irradiation.

### **Electrical characteristics of Al foil/Si junctions by surface activated bonding**

Katuya HURUNA, Jianbo LIANG, Moeko MATSUBARA (Toyo Aluminum K. K.), Marwan DHAMRIN (Toyo Aluminum K. K.), Yositaka NISHIO (Toyo Aluminum K. K.), and Naoteru SHIGEKAWA

*Extended Abstracts of 2016 IEEE International Meeting for Future of Electron Devices, Kansai (IMFEDK)*, pp. 86-87 (2016). DOI: 10.1109/IMFEDK.2016.7521688

We successfully fabricated Al-foil/p-Si junctions by surface activated bonding (SAB). We found that the junctions revealed Schottky properties by measuring their current-voltage characteristics. We also found that the reverse-bias current of the junctions was decreased, i.e., their electrical characteristics were improved by annealing at temperatures below 200 °C. These results demonstrate that the bonding of metal foils should be useful for fabricating several-ten- $\mu\text{m}$ -thick electrodes.

### **Effects of layered CdTe nano particles on Si solar cells**

Tomoki OGAWA, Jianbo LIANG, Shingo IMASAKI, Taichi WATANABE, Daegwi KIM, and Naoteru SHIGEKAWA

*Extended Abstracts of 2016 IEEE International Meeting for Future of Electron Devices, Kansai (IMFEDK)*, pp. 114-115 (2016). DOI: 10.1109/IMFEDK.2016.7521707

Layered CdTe nanoparticles were deposited on surfaces of n-on-p crystalline Si solar cells. Their short circuit current and conversion efficiency were enhanced due to the nanoparticle deposition. Measurements of reflectance and external-quantum-efficiency spectra as well as atomic-force-microscope observations implied that the enhancements in cell performances were attributable to textured structures of the deposited nanoparticle layers.

### **Improved electrical properties of n-n and p-n Si/SiC junctions with thermal annealing treatment**

Jianbo LIANG, Shota NISHIDA, Manabu ARAI (New Japan Radio Co. Ltd.), and Naoteru SHIGEKAWA

*J. Appl. Phys.* 120, 034504 [7 pages] 2016.

The effects of annealing process on the electrical properties of  $n^+$ -Si/n-SiC and  $p^+$ -Si/n-SiC junctions fabricated by using surface-activated bonding are investigated. It is found by measuring the current-voltage ( $I$ - $V$ ) characteristics of  $n^+$ -Si/n-SiC junctions that the reverse-bias current and the ideality factor decreased to  $2.0 \times 10^{-5}$  mA/cm<sup>2</sup> and 1.10, respectively, after the junctions annealing at 700 °C. The flat band voltages of  $n^+$ -Si/n-SiC and  $p^+$ -Si/n-SiC junctions obtained from capacitance-voltage ( $C$ - $V$ ) measurements decreased with increasing the annealing temperature. Furthermore, their flat band voltages are very close to each other irrespective of the annealing temperature change, which suggest that the Fermi level is still pinned at the bonding interface even for the junctions annealing at high temperature and the interface state density causing Fermi level pinning varies with the junctions annealing. The reverse characteristics of  $n^+$ -Si/n-SiC junctions are in good agreement with calculations based on thermionic field emission. In addition, the calculated donor concentration of 4H-SiC epi-layers and flat band voltage are consistent with the values obtained from  $C$ - $V$  measurements.

### **Thickness modulation and strain relaxation in strain-compensated InGaP/InGaP multiple-quantum-well structure grown by metalorganic molecular beam epitaxy on GaAs (100) substrate**

Manabu MITSUHARA (NTT Laboratories), Noriyuki WATANABE (NTT Laboratories), Haruki YOKOYAMA (NTT Laboratories), Lyuuzou IGA (NTT Laboratories), and Naoteru SHIGEKAWA

*J. Crystal Growth.* 449, 86 [6 pages] 2016.

We have investigated the structural features of a strain-compensated InGaP/InGaP multiple-quantum-well (MQW) structure on GaAs (100) substrate with a band-gap energy of around 1.7 eV for solar cell applications. In transmission electron microscopy images,

noticeable thickness modulation was observed in the barrier layers for a sample grown at the substrate temperature of 530 °C. Meanwhile, the X-ray diffraction patterns indicated that strain relaxation predominantly occurred in the well layers. Decreasing the substrate temperature from 530 to 510 °C was effective in suppressing both the thickness modulation and strain relaxation. Additionally, increasing the growth rate of the well layer further suppressed the thickness modulation. In room-temperature photoluminescence (PL) emission spectra, the sample grown at 510 °C showed approximately 50 times higher PL peak intensity than the one grown at 530 °C.

#### **Effects of annealing on the electrical characteristics of GaAs/GaAs junctions by surface-activated bonding**

Li CHAI, Jianbo LIANG, and Naoteru SHIGEKAWA

*Jpn. J. Appl. Phys.* 55, 068002 [3 pages] 2016.

The electrical properties of GaAs/GaAs junctions fabricated by surface-activated bonding (SAB) and annealing were examined on the basis of the charge neutral level model. The potential barrier height, the density of interface states, and the charge neutral level at GaAs/GaAs interfaces were estimated from the measured dependences of the electrical conductance of n-GaAs/n-GaAs and p-GaAs/p-GaAs junctions on ambient temperature. The barrier height and the density of interface states were lowered by increasing the annealing temperature to 400 °C, which suggested that the damage introduced during the SAB process was partly reduced.

#### **Low-temperature ( $\geq 400$ °C) growth of InN by metalorganic vapor phase epitaxy using an NH<sub>3</sub> decomposition catalyst**

Akio YAMAMOTO (Univ. of Fukui), Kazuki KODAMA (Univ. of Fukui), Naoteru SHIGEKAWA, Takashi MATSUOKA (Univ. of Tohoku), and Masaaki KUZUHARA (Univ. of Fukui)

*Jpn. J. Appl. Phys.* 55, 05FD04 [5 pages] 2016.

We report the metalorganic vapor phase epitaxial (MOVPE) growth of InN using a NiO-based pellet-type NH<sub>3</sub> decomposition catalyst. The use of the catalyst significantly changes the growth behavior of InN, which is dependent on the growth temperature ( $T_g$ ). Continuous InN films without the incorporation of metallic In and a cubic phase are grown at  $T_g = 400 - 480$  °C. An InN film grown at  $T_g \approx 450$  °C has a full-width at half maximum (FWHM) of 376 arcsec in the X-ray rocking curve for InN (0002) reflection. At  $T_g \geq 500$  °C, the deposition rate of InN rapidly decreases and the deposited films become discontinuous with large (ca. 1  $\mu\text{m}$ ) pyramidal grains of InN. Depositions are scarcely obtained at  $T_g \geq 600$  °C. Such changes in the growth behavior of InN are governed by the NH<sub>3</sub> decomposition.

#### **Mapping of Si/SiC hetero p-n Junctions Using Scanning Internal Photoemission Microscopy**

Masato SHINGO (Univ. of Fukui), Jianbo LIANG, Naoteru SHIGEKAWA, Manabu ARAI (New Japan Radio Co. Ltd.), and Kenji SHIOJIMA (Univ. of Fukui)

*Jpn. J. Appl. Phys.* 55, 04ER15 [4 pages] 2016.

We demonstrated the two-dimensional characterization of p<sup>+</sup>-Si/n-SiC heterointerfaces by scanning internal photoemission microscopy (SIPM). In internal photoemission spectra, a linear relationship was found between the square root of photoyield ( $Y$ ) and photon energy, and the threshold energy ( $qV_{\text{th}}$ ) was reasonably obtained to be 1.34 eV. From the SIPM results,  $Y$  and  $qV_{\text{th}}$  maps were successfully obtained, and nanometer-deep gaps in the junction were sensitively visualized as a pattern. These results suggest that this method is a powerful tool for investigating the inhomogeneity of heterojunctions as well as their carrier transport properties.

#### **Impact of optical properties of anti-reflection coatings on characteristics of InGaP/GaAs/Si hybrid triple-junction cells**

Naoteru SHIGEKAWA and Jianbo LIANG

*Proc. 2015 IEEE 42<sup>nd</sup> Photovoltaic Specialists Conference*, pp. 14-19 [5 pages] 2015  
DOI:10.1109/PVSC.2015.7356076.

InGaP/GaAs/Si hybrid triple-junction cells with 95-nm SiN/65-nm SiO<sub>2</sub> bilayer and 75-nm SiN monolayer films as anti-reflection (AR) coatings were investigated. A more marked imbalance in photo currents of subcells was observed in cells with SiN monolayer films. The difference in imbalance was attributed to the optical properties of coatings. The short-circuit currents of the two triple-junction cells were close to each other and were larger than photo currents in the Si bottom cells while the open circuit voltages were slightly different. These findings suggested that subcells might be electrically coupled to each other in multi-junction operations.

#### **Interaction between Plasmas and Liquids**

Tatsuru SHIRAFUJI and Nozomi Takeuchi

*J. Plasma Fusion Res.*, Vol. 92, pp. 693-699 (2016) (in Japanese)

The conventional medium which is in contact with plasma has been a solid. Since non-equilibrium low-temperature plasma can be generated under atmospheric pressure, the liquid or even the living tissue can also be the medium which makes contact with plasma. In this paper, we describe various new phenomena which are expected near the plasma-liquid interface.

#### **Matrix-assisted Laser Desorption Ionization Time-of-flight Mass Spectrometric Analysis of Degradation Products After Treatment of Methylene Blue Aqueous Solution with Three-dimensionally Integrated Microsolution Plasma**

Tatsuru SHIRAFUJI, Ayano NOMURA, Yui HAYASHI, Kenji TANAKA and Motonobu GOTO

*Jpn. J. Appl. Phys.*, Vol. 55, 01AH02 (5 pages) (2016)

Methylene blue can be degraded in three-dimensionally integrated microsolution plasma. The degradation products have been analyzed by matrix-assisted laser desorption ionization time-of-flight (MALDI TOF) mass spectrometry to understand the degradation mechanisms. The results of MALDI TOF mass spectrometry have shown that sulfoxide is formed at the first stage of the oxidation. Then, partial oxidation proceeds on the methyl groups left on the sulfoxide. The sulfoxide is subsequently separated to two benzene derivatives. Finally, weak functional groups are removed from the benzene derivatives.

DOI: 10.7567/JJAP.55.01AH02

#### **Acquisition of Cell-adhesion Capability of the Surface of Crosslinked Albumin Films Irradiated with Atmospheric-pressure Plasma Jets**

Tatsuru SHIRAFUJI, Mami IWAMURA, Ryosuke TAGA, Yukiyasu KASHIWAGI, Kota NAKAJIMA, Yuji OGATA, Kenji TANAKA, Akira TACHIBANA and Toshizumi TANABE

*Jpn. J. Appl. Phys.*, Vol. 55, 07LG03 (5 pages) (2016)

Crosslinked albumin films, to which L929 cells do not attach by nature, acquire the L929-cell-adhesion capability by irradiation of an atmospheric-pressure plasma jet (APPJ) of He gas. The number of attached cells was  $2.6 \times 10^4$  cells/cm<sup>2</sup> after the APPJ irradiation for 180 s, while conventional UV photolithography, which was performed in our previous work, required 2 h to obtain the same order of magnitude of the number of attached cells. The contact angle of samples decreased steeply from 105 to 38° in the first 10 s irradiation, but decreased quite gradually from 38 to 32° with increasing irradiation time from 10 to 180 s. In contrast to the nonlinear variation in the contact angles, the number of attached cells almost linearly increased from  $4.5 \times 10^3$  to  $2.6 \times 10^4$  cells/cm<sup>2</sup> with increasing treatment time. X-ray photoelectron spectroscopy of the samples indicated that hydrophilic functional groups of C-C=O gradually formed with increasing APPJ irradiation time up to 180 s. These results suggest that the cell-adhesion capability of the crosslinked albumin films is not simply explained by the decrease in contact angle but also by the formation of oxidized functional groups on the

surface. The effects of UV and vacuum UV light from APPJ were negligible, which indicates that the formation of oxidized functional groups on the surface is not caused by photon-assisted surface reactions but by reactions involving chemically active species supplied from APPJ.

DOI: 10.7567/JJAP.55.07LG03

#### **PECVD of SiOC Films Using a Sheet-type Atmospheric Pressure Plasma Jet**

Kota NAKAJIMA, Kenji TANAKA and Tatsuru SHIRAFUJI

*The 9th International Conference on Reactive Plasmas / The 68th Gaseous Electronics Conference / The 33rd Symposium on Plasma Processing, Oct. 12-16, 2015, Honolulu, USA, GT1.00143 (2 pages) (2015)*

We have developed a reactor for atmospheric pressure plasma-enhanced chemical vapor deposition (PECVD) which utilizes a unique gas-flow scheme for avoiding the particle formation. We deposited SiOC films by using this reactor, in which the source material was hexamethyldisiloxane and discharge/carrier gas was He. We have confirmed the deposition of SiOC films from the results of XPS measurements. We have also confirmed that no particulates are in and on the deposited films as long as observing the films with eye-observation and TEM.

#### **Characteristics of Solution Plasma Generated with Coaxial DBD**

Kentaro NISHIMOTO, Kenji TANAKA, Tatsuru SHIRAFUJI and Shin-ichi IMAI

*The 9th International Conference on Reactive Plasmas / The 68th Gaseous Electronics Conference / The 33rd Symposium on Plasma Processing, Oct. 12-16, 2015, Honolulu, USA, LW1.00087 (2 pages) (2015)*

We have applied a coaxial DBD to the treatment of water. While conventional solution plasma has shown a strong dependence on the electrical conductivity of water, the coaxial DBD has shown more robust characteristics within the conductivity range of 0.5-160  $\mu\text{S}/\text{cm}$ . The coaxial DBD has shown 3-fold higher energy efficiency in indigo carmine degradation than the conventional solution plasma.

#### **Mechanisms of Methylene Blue Degradation in Three-dimensionally Integrated Micro-solution Plasma**

Ayano NOMURA, Yui HAYASHI, Kenji TANAKA, Tatsuru SHIRAFUJI and Motonobu GOTO

*The 9th International Conference on Reactive Plasmas / The 68th Gaseous Electronics Conference / The 33rd Symposium on Plasma Processing, Oct. 12-16, 2015, Honolulu, USA, LW1.00088 (2 pages) (2015)*

We deduce possible mechanisms of methylene blue degradation in three-dimensionally integrated micro-solution plasma by analyzing products after the plasma treatment. We have analyzed the degradation products by using matrix-assisted laser desorption ionization time-of-flight (MALDI-TOF) mass spectrometry. The results of MALDI-TOF mass spectrometry have indicated the formation of the sulfoxide in the first stage of the oxidation. Then, partial oxidation proceeds on the methyl groups left on the sulfoxide. After that, the sulfoxide splits into benzene derivatives. Finally, weak functional groups are removed from the benzene derivatives.

#### **Time-resolved optical emission spectroscopy on DBD of Ar gas in contact with water**

Kazuhiko OBANA, Kenji TANAKA and Tatsuru SHIRAFUJI

*The 9th International Conference on Reactive Plasmas / The 68th Gaseous Electronics Conference / The 33rd Symposium on Plasma Processing, Oct. 12-16, 2015, Honolulu, USA, LW1.00089 (2 pages) (2015)*

Three-dimensionally integrated micro-solution plasma (3D IMSP) generates a large number of Ar microplasmas in contact with the aqueous solution flowing in a porous dielectric material. For the purpose of fundamental understanding of the 3D IMSP, we

have constructed a simple reactor that is considered to have an equivalent environment to that in one bubble in the 3D IMSP. We have performed optical emission spectroscopy (OES) on the plasma generated in the simple reactor. The OES results have shown that the optical emission of OH (A-X) lasts longer than that of Ar. We discuss its possible mechanisms together with numerical simulation of the DBD and detailed analysis of the spectral profiles of the OH (A-X) emission.

#### **Gold Nanoparticle Synthesis by 3D Integrated Micro-solution Plasma in a 3D Printed Artificial Porous Dielectric Material**

Naoya SOTODA, Kenji TANAKA and Tatsuru SHIRAFUJI

*The 9th International Conference on Reactive Plasmas / The 68th Gaseous Electronics Conference / The 33rd Symposium on Plasma Processing, Oct. 12-16, 2015, Honolulu, USA, LW1.00090 (2 pages) (2015)*

We have fabricated a 3D integrated micro-solution plasma (3D IMSP) reactor using an artificial porous dielectric material using 3D printer technology. We have successfully obtained microplasmas in this reactor by feeding the gas/liquid mixed medium of Ar and water. We have tried synthesis of gold nanoparticles by substituting the water to H<sub>2</sub>AuCl<sub>4</sub> aqueous solution. We have characterized the aqueous solution after the 3D IMSP treatment by optical absorption spectroscopy. We have confirmed a broad absorption peak at approximately 550 nm in the absorption spectrum, which corresponds to the plasmon resonance absorption by gold nanoparticles.

#### **Sterilization of *E. coli* using 3D integrated micro-solution plasma**

Junpei YAMAMOTO, Kenji TANAKA, Tatsuru SHIRAFUJI, Takeshi NAKANISHIT and Masaya KITAMURA

*The 9th International Conference on Reactive Plasmas / The 68th Gaseous Electronics Conference / The 33rd Symposium on Plasma Processing, Oct. 12-16, 2015, Honolulu, USA, LW1.00091 (2 pages) (2015)*

Three-dimensionally integrated micro-solution plasma (3D IMSP) generates a large number of microplasmas in contact with the aqueous solution flowing in a porous dielectric material. We have applied 3D IMSP to the sterilization of *E. coli* for the purpose of large-volume water sterilization. We have successfully sterilized the water (150 mL) with *E. coli* of 10<sup>6</sup> cells/mL within 6 min. We also discuss the effects of plasma-treated water on the sterilization of *E. coli*.

#### **In-water Plasma Generation and Its Performance Using a Coaxial DBD Device and Compact Power Supply**

Shin-ichi IMAI, Yoshihiro SAKAGUCHI, Yoshiko MIYAMOTO, Akihiro ODAGAWA and Tatsuru SHIRAFUJI

*The 9th International Conference on Reactive Plasmas / The 68th Gaseous Electronics Conference / The 33rd Symposium on Plasma Processing, Oct. 12-16, 2015, Honolulu, USA, TF1.00004 (2 pages) (2015)*

This paper describes in-water plasma generation and its characteristics using a coaxial tungsten electrode and a compact power supply. In-water plasma is formed in an air stream supplied from outside by an air pump. The power supply circuitry, which is based on LC series resonance, was designed using SPICE simulation. We were able to reduce the volume of the power supply to 1.5 liters. The behavior of the in-water plasma and voltage waveform generated by our device and the power supply were simultaneously observed using a high-speed camera system in conjunction with an oscilloscope. The device performance was estimated using the decoloration of indigo carmine during Plasma ON and OFF. The radicals and species in in-water plasma were measured using an ESR-spin-trap method. It was found that O<sub>2</sub><sup>-</sup> and OH radicals are generated during Plasma ON, and OH radicals remain after Plasma OFF.

### **Acquisition of Cell-adhesion Ability on the Surface of Crosslinked Albumin Films Irradiated with Atmospheric Pressure Plasma Jets**

Mami IWAMURA, Kota NAKAJIMA, Ryosuke TAGA, Kenji TANAKA, Tatsuru SHIRAFUJI, Akira TACHIBANA and Toshizumi TANABE

*The 9th International Conference on Reactive Plasmas / The 68th Gaseous Electronics Conference / The 33rd Symposium on Plasma Processing, Oct. 12-16, 2015, Honolulu, USA, WF4.00005 (2 pages) (2015)*

We have applied an atmospheric-pressure plasma jet (APPJ) of He gas to surface treatment on crosslinked albumin films. The crosslinked albumin films, to which L929 cells do not attach, acquire the L929 cell-adhesion ability by the APPJ irradiation in a quite short time of 300 s. We have confirmed the formation of hydrophilic chemical bonds on the APPJ irradiated samples through XPS measurements. The optical emission spectrum of the APPJ has not shown strong emission of O and OH. These results suggest that the causes of the hydrophilic chemical bonds are the dangling bond formation by abundant excited N<sub>2</sub> and He, and successive oxidation of the dangling bonds by ambient air and/or water vapor.

### **Time-resolved OES on Argon DBD with a Water Electrode - Experimental Results and Numerical Simulation -**

Tatsuru SHIRAFUJI, Kazuhiko OBANA and Kenji TANAKA

*The 37th International Symposium on Dry Process, Nov. 5-6, 2015, Awaji, Japan, P-61 (2 pages) (2015)*

Time-resolved OES has been performed on DBD of Ar with a water electrode for comparing our previously reported numerical simulation results of the unique temporal variation in OH(A) density due to dissociative recombination of low- $T_e$  electrons and H<sub>3</sub>O<sup>+</sup> after the discharge phase. Experimental results show good agreement to the results of numerical simulation although it is still qualitative agreement.

### **Blueshifted Flat Dispersion Relation of Exciton-Polariton Condensates in a CuBr Microcavity**

Masaaki NAKAYAMA, Katsuya MURAKAMI, and DaeGwi KIM

*Journal of the Physical Society of Japan* Vol.85, 054702 (2016)

We have investigated cavity-polariton condensation effects on the dispersion relation of the lower polariton branch (LPB) at 77 K in a CuBr microcavity by angle-resolved photoluminescence (PL) spectroscopy. The intrinsic cavity-polariton dispersion relations were characterized by the analysis of the incident light angle (in-plane wave vector  $k_{\parallel}$ ) dependence of cavity-polariton energies obtained using angle-resolved reflectance spectroscopy. It was found that a blueshifted PL band appears with a threshold-like nature as a function of excitation power density. The in-plane wave vector dependence of the blueshifted PL energy exhibits a flat dispersion relation in the  $k_{\parallel}$  range from 0 to  $\sim 4.4 \mu\text{m}^{-1}$ ,

which is clearly separated from the intrinsic LPB because of the large blueshift of  $\sim 15$  meV. We show that the blueshifted flat dispersion relation is possibly explained by the theory for a diffusive Goldstone mode peculiar to nonequilibrium cavity-polariton condensation.

DOI: 10.7566/JPSJ.85.05470

### **Polariton Dispersion Relations under Condensation in a CuBr Microcavity**

Masaaki NAKAYAMA, Katsuya MURAKAMI, and DaeGwi KIM

*Physica Status Solidi C* Vol. 13, pp. 81-84 (2016)

We have investigated the exciton-polariton condensation in a CuBr microcavity with HfO<sub>2</sub>/SiO<sub>2</sub> distributed Bragg reflectors, focusing on condensation effects on polariton dispersion relations. The polariton distribution as a function of in-plane wave vector  $k_{\parallel}$  under illumination was measured with angle-resolved photoluminescence (PL)

spectroscopy. In addition, we characterized the intrinsic polariton dispersion relations as reference data from analysis of the results obtained using angle-resolved reflectance spectroscopy. It was found that the polariton condensation causes a large blueshift of the lower polariton branch (LPB) and a flat dispersion relation around the ground state at  $k_{\parallel}=0$ . The renormalized dispersion relation of the LPB under the polariton condensation was quantitatively analyzed using a theory for a diffusive Goldstone mode peculiar to nonequilibrium condensation.

DOI: 10.1002/pssc.201510076

### **Dynamical Formation Process of Electron–Hole Droplets in a GaAs/AlAs type-II Superlattice**

Yoshiaki FURUKAWA and Masaaki NAKAYAMA

*Journal of the Physical Society of Japan* Vol. 85, 034701 (2016)

We have investigated photoluminescence (PL) dynamics at 10 K in a GaAs/AlAs type-II superlattice from the viewpoint of the dynamical formation of electron–hole droplets (EHDs) from electron-hole plasma (EHP) in a gas phase. From systematic time-resolved PL (TRPL) spectra, we found that only a broad PL band attributed to the EHP is observed in an initial time region within  $\sim 0.4$  ns, whereas the exciton- and biexciton-PL bands appear at  $\sim 0.7$  ns. The peak energy and width of the broad PL band hardly depend on time after  $\sim 14$  ns, associated with the fact that the effective temperature of carriers agrees with that of the excitonic system. This suggests the formation of EHDs in thermal quasi-equilibrium. We estimated the stability energy relative to the biexciton energy to be  $\sim 3.1$  meV from the line-shape analysis of the TRPL spectra. This is consistent with the result obtained from the line-shape analysis of the steady-state PL spectrum. Consequently, the above temporal changes of the TRPL spectra demonstrate the dynamical transition from the EHP to the EHD during the PL decay process.

DOI: 10.7566/JPSJ.85.034701

### **Photoluminescence from Exciton-Electron Inelastic Scattering in a GaAs/AlAs Multiple-Quantum-Well Structure**

Saeka NAKANISHI, Yoshiaki FURUKAWA and Masaaki NAKAYAMA

*Physica Status Solidi C* Vol.13, 109-112 (2016)

We have investigated the characteristics of photoluminescence (PL) from exciton-electron inelastic scattering in a GaAs (5.1 nm)/AlAs (5.1 nm) multiple-quantum-well structure. The excitation power dependence of PL spectra was measured in a wide temperature region from 10 to 285 K. We detected a PL band, which appears with a threshold-like nature at each temperature. In a low temperature region below  $\sim 80$  K, the energy spacing between the threshold-like appearance PL band and heavy-hole exciton almost agrees with the exciton binding energy. This indicates that the PL band originates from well-known exciton-exciton inelastic scattering. In contrast, in a high temperature region above  $\sim 90$  K, the energy spacing continuously increases with an increase in temperature. The temperature dependence of the energy spacing is explained by a theoretical model for exciton-electron inelastic scattering energy and momentum conservation in the scattering process. Thus, it is concluded that the mechanism of the threshold-like appearance PL band related to exciton inelastic scattering changes with temperature. In addition, we confirmed that the exciton-electron inelastic scattering produces an optical gain using a variable stripe length method for PL measurements.

DOI: 10.1002/pssc.201510126

### **Evidence for Formation of Self-Trapped Excitons in a $\beta$ -Ga<sub>2</sub>O<sub>3</sub> Single Crystal**

Suguru YAMAOKA and Masaaki NAKAYAMA

*Physica Status Solidi C* Vol. 13, 93–96 (2016)

We have investigated photoluminescence (PL) and absorption properties of a  $\beta$ -Ga<sub>2</sub>O<sub>3</sub> single crystal from the viewpoint of the stability of self-trapped excitons (STEs). A broad PL band with a large Stokes shift, which is conventionally assigned to the STE, was observed. To reveal the stability of the STE, we precisely measured the temperature dependence of the Urbach tails in absorption spectra. It was confirmed that the Urbach tails at all temperatures converge into a specific point, which verifies the validity of the treatment of the Urbach tail. We analyzed the temperature dependence of the exponential slope, the so-called steepness constant, of the Urbach tail and evaluated the exciton-phonon coupling constant  $g$ , which defines the stability of the STE, to be  $g = 5.4$ . Based on a previously reported theory for exciton-phonon interactions,  $g > 1$  generally results in that the STE is a stable state relative to a free exciton. Consequently, the above large  $g$  factor demonstrates that the STE formation is stable in  $\beta$ -Ga<sub>2</sub>O<sub>3</sub>.

DOI: 10.1002/pssc.201510124

### **Photoluminescence Dynamics of Formation of Electron-Hole Droplets in a GaAs/AlAs Type-II Superlattice**

Yoshiaki FURUKAWA and Masaaki NAKAYAMA

*Physica Status Solidi C Vol. 13*, 101-104 (2016)

We have investigated photoluminescence (PL) dynamics at 10 K in a GaAs/AlAs type-II superlattice from the viewpoint of the dynamical formation of electron-hole droplets (EHDs) from electron-hole plasma (EHP) in a gas phase. From systematic time-resolved PL (TRPL) spectra, we found that only a broad PL band attributed to the EHP is observed in an initial time region within  $\sim 0.4$  ns, whereas the exciton- and biexciton-PL bands appear at  $\sim 0.7$  ns. The peak energy and width of the broad PL band hardly depend on time after  $\sim 14$  ns, associated with the fact that the effective temperature of carriers agrees with that of the excitonic system. This suggests the formation of EHDs in thermal quasi-equilibrium. We estimated the stability energy relative to the biexciton energy to be  $\sim 3.1$  meV from the line-shape analysis of the TRPL spectra. This is consistent with the result obtained from the line-shape analysis of the steady-state PL spectrum. Consequently, the above temporal changes of the TRPL spectra demonstrate the dynamical transition from the EHP to the EHD during the PL decay process.

DOI: 10.1002/pssc.201510121

### **Unique Characteristics of Nonequilibrium Carrier Transport Dynamics in an Undoped GaAs/*n*-type GaAs Epitaxial Structure**

Takayuki HASEGAWA and Masaaki NAKAYAMA

*Applied Physics Express Vol. 9*, 071001 (2016)

We have investigated nonequilibrium carrier dynamics in an undoped GaAs/*n*-type GaAs epitaxial structure at room temperature using reflection-type pump-probe spectroscopy at different pump photon energies and Monte Carlo simulation. It was found that the transport process of photogenerated electrons in the undoped layer is characterized by the valance between the quasiballistic motion passing through the undoped layer and the intervalley scattering from the  $\Gamma$  valley to the L one as a function of the excess energy of photogenerated electrons. The  $\Gamma$ -L scattering component exhibits threshold-like appearance and then gradually increases with increasing excess energy.

DOI: 10.7567/APEX.9.071001

### **Detection Sensitivities of Photoluminescence Spectroscopy and Polariscopy to Residual Strains in a (110)-oriented ZnTe Single Crystal: Explore of Strain-Sensitive Inspection Techniques**

Hideo TAKEUCHI

*Physics Procedia* Vol. 76 4 -10 (2015)

We demonstrate that sensitivity of polariscopy to residual strains is higher than that of the photoluminescence spectroscopy in a (110)-oriented ZnTe single crystal. We carried out x-ray topography and micro  $\theta$ - $2\theta$  x-ray diffraction measurements in order to thoroughly clarify the crystal quality connecting with the residual strains. The two x-ray analyses revealed that there is misalignment from the [110] direction in some regions of the present sample. We found the following main results: The polariscopic analysis detects the residual strain formed by the misalignment, whereas the photoluminescence measurement cannot detect the residual strain. Thus, we conclude that polariscopy has the sensitivity to the residual strain higher than that of the photoluminescence spectroscopy. We confirmed that the polariscopic analysis can detect the internal strain less than 0.02% in the ZnTe crystal. In addition, we discuss the applicability of polariscopic analysis to other compound semiconductors.

DOI: 10.1016/j.phpro.2015.10.002

### **Control of Localized Surface Plasmon Resonance Energy in Monolayer Structures of Gold and Silver Nanoparticles**

Hiroki YOKOTA, Taichi TANIGUCHI, Taichi WATANABE and DaeGwi KIM

*Phys. Chem. Chem. Phys.* Vol. 17, pp. 27077-27081 (2015)

Monolayer structures of Au and Ag nanoparticles (NPs) were fabricated by a dipping method to realize the control of localized surface plasmon resonance (LSPR) energy. The mean inter-particle distance in the monolayer was controlled by changing the concentration of NPs in the colloidal solution used for monolayer assembly. The extinction-peak energy of the monolayer structure was red-shifted with decreasing inter-particle distance, reflecting plasmon coupling between NPs.

doi: 10.1039/c5cp03928b

### **Control of Photoluminescence Intensity in Nanostructured Layers of Lipid-Soluble Quantum Dots and Water-Soluble Gold Nanoparticles**

Kazuma OHSHIRO, Hang-Beom BU and DaeGwi KIM

*Chem. Lett.* Vol. 45, pp. 520-522 (2016)

We propose a new preparation method for layered structures consisting of lipid-soluble CdSe quantum dots (QDs) and water-soluble Au nanoparticles (NPs). The self-assembled monolayer of (3-mercaptopropyl)trimethoxysilane (MPTMS) was introduced as a “*binder*” of lipid-soluble QDs on a polyelectrolyte layer (PE). Furthermore, the separation distance between the CdSe QDs and the Au NP layers was controlled by the thickness of the PE layers, and the systematic change from PL quenching to PL enhancement of the CdSe QDs is observed.

doi:10.1246/cl.160096

### **Hydrothermal Synthesis of NAC-Capped II-VI Semiconductor ZnSe Quantum Dots in Acidic Condition**

Yong-Shin LEE, Hang-Beom BU, Taichi TANIGUCHI, Tomomi TAKAGI, Susumu SOBUE, Hitoshi YAMADA, Takao IWAKI, and DaeGwi KIM

*Chem. Lett.* Vol. 45, pp. 878-880 (2016)

Semiconductor ZnSe quantum dots (QDs) were hydrothermally prepared in the presence of *N*-acetyl-*L*-cysteine as a stabilizer. The photoluminescence (PL) properties were dramatically improved by selecting appropriately pH value of precursor solution, the PL intensity in the ZnSe QDs prepared at pH 6 was strongest irrespective of the size of ZnSe QDs. XRD pattern demonstrated the formation of cubic zinc blende ZnSe lattice structure and crystallinity.

doi:10.1246/cl.160431

### **Controls of Electronic Structures and Phonon Dynamics in Quantum Dot Superlattice by Manipulating Interior Nano Space**

I-Ya CHANG, DaeGwi KIM and Hyeon-Deuk KIM

*ACS Appl. Mater. Interfaces*, in press.

Quantum dot (QD) superlattice, a periodically ordered array structure of QDs, is expected to provide novel photo-optical functions owing to resonant couplings between adjacent QDs. Here, we computationally demonstrated that electronic structures and phonon dynamics of QD superlattice can be effectively and selectively controlled by manipulating its interior nano space where quantum resonance between neighboring QDs appears rather than by changing component QD size, shape, compositions, etc. A simple H-passivated Si QD was examined to constitute one-, two- and three-dimensional QD superlattice, and thermally fluctuating band energies and phonon modes were simulated by finite-temperature ab initio molecular dynamics (MD) simulations. The QD superlattice exhibited decrease of the band-gap energy enhanced by thermal modulations and also selective extraction of charge carriers out of the component QD, indicating its advantage as a promising platform to be implemented in solar cells. Our dynamical phonon analyses based on the ab initio MD simulations revealed that THz-frequency phonon modes were created by inter-QD crystalline lattice formed in the QD superlattice, which can contribute to thermoelectric conversion of low energy and will be useful for direct observation of the dimension-dependent superlattice. Further, we found that crystalline and ligand-originated phonon modes inside each component QD can be independently controlled by asymmetry of the superlattice and by restriction of the interior nano space, respectively. Taking into account the thermal effects at the finite temperature, we proposed guiding principles for designing efficient and space-saving QD superlattice to develop functional photovoltaic and thermoelectric devices.

### **Typical Pure States and the Analysis of Nonequilibrium Processes of Mesoscopic Systems**

Takaaki MONNAI and Ayumu SUGITA

*J. Stat. Mech.* 2016, 054004 (2016)

For isolated quantum many-body systems, we extend the availability of the intrinsic thermal nature of typical pure states to a class of nonequilibrium processes which start from an initial equilibrium. For concreteness, we calculate the spectral distribution of the work done on the system on the basis of a single pure state. It means that we can accurately calculate the entire fluctuation of the energy only from a single pure state instead of the thermodynamic ensembles.

### **Origin of Temperature Gradient in Nonequilibrium Steady States in Weakly Coupled Quantum Spin Systems**

Toyohiko ISHIDA, and Ayumu SUGITA

*J. Phys. Soc. Jpn.* 85, 074006 (10 pages) (2016)

We study nonequilibrium steady states (NESSs) in quantum spin-1/2 chains in contact with two heat baths at different temperatures. We consider the weak-coupling limit both for spin-spin coupling in the system and for system-bath coupling. This setting allows us to treat NESSs with a nonzero temperature gradient analytically. We develop a perturbation theory for this weak-coupling situation and show a simple condition for the existence of nonzero temperature gradient. This condition is independent of the integrability of the system.

### **Dynamics of Charge Carriers on Hexagonal Nanoribbons with Vacancy Defects**

Wiliam Ferreira da CUNHA, Pedro Henrique de Oliveira NETO, Akira TERAJ, and Geraldo Magela e SILVA

*Phys. Rev. B* 94, 014301 (10 pages) (2016)

We develop a general model to investigate the dynamics of charge carriers in vacancy endowed honeycomb two-dimensional nano lattices. As a fundamental application, results concerning the influence of vacancies placed on different sites of semiconducting armchair graphene nanoribbons (AGNR) over the transport of polarons are presented. It is observed that the positioning of vacancies plays a major role over the scattering of the charge carriers, in the sense that their overall mobility is determined by where the defect is allocated.

By considering different structural configurations of the system, the arising polaron can either move freely or be reflected. Therefore, our work provides a phenomenological understanding of the underlying mechanism responsible for the change of conductivity experienced by systems in which structural defects are present, a fact that has been reported for different nanostructures of the same

symmetry. Because vacancies are one of the most common kinds of defects and are, in practice, unavoidable, the kind of description proposed in the present paper is crucial to correctly address transport and electronic properties in more realistic electronic devices based on two-dimensional nanolattices.

## **Electrical and Information Engineering**

### **A Method of Wavelength Selection of Multispectral Image for the Separation of Tumor Region**

Kayo YOSHIMOTO, Hideya TAKAHASHI, Kenji YAMADA (Osaka University), and Shigeto Yoshida (Hiroshima University)

*Proc. Ninth Int. Conf. Genetic and Evolutionary Computing*, Yangon, Aug. 26-28, pp.199-208 (2015)

Endoscopy is widely used for examinations and diagnosis of cancer. However, it is difficult to accurately identify the tumor region from the endoscopic image unless experienced experts. In this paper, we propose a method of the separation of tumor region for endoscope surgery and examination by using multispectral images. By selecting the effective wavelength to identify from multispectral images, the tumor region can be separate. We confirm the proposed method by several test targets. The proposed method would help for endoscopic surgery.

### **Retinal projection type 3D head-mounted display using an HOE lens array**

Yasuhiro TAKATSUKA, Kayo YOSHIMOTO, and Hideya TAKAHASHI

*Proc. IS&T Int. Symp. Electronic Imaging 2016 Stereoscopic Display and Applications XXVII*, San Francisco, Feb. 17, pp.SDA-428.1-SDA-428.6 (2016)

We propose a retinal projection type super multi-view (SMV) HMD using a 2D microlens array. The smooth motion parallax is provided by SMV technique. Moreover, if a viewer focuses his or her eyes on the displayed 3D image, the stimulus of accommodation of the human eye is reproduced naturally by SMV technique. Therefore, although the proposed HMD is a monocular HMD, it provides observers with natural 3D images. To verify the effectiveness of the proposed HMD by using camera, we constructed the prototype holographic optical element (HOE). The number of microlenses is 9, and the focal length and the size of each microlens of the prototype HOE were 11.1 mm and 20 mm × 20 mm, respectively. The distance between each convergence point was 6.67 mm. We displayed 3D images at the distance from 200mm to 2000mm in front of the camera, and confirmed the accommodation by the prototype HMD.

### **360-degree three-dimensional display with virtual display surface**

Hodaka YAMADA, Kayo YOSHIMOTO, Hideya TAKAHASHI, and Kenji YAMADA (Osaka University)

*Proc. IS&T Int. Symp. Electronic Imaging 2016 Stereoscopic Display and Applications XXVII*, San Francisco, Feb. 15, pp.SDA-452.1-SDA-452.6 (2016)

We propose the omnidirectional 3D display system which displays directly touchable 3D images. The display surface of the proposed display is cylindrical, and displayed 3D images are observed around the cylindrical display surface. The proposed system composed of multiple basic display units. Each basic display unit consists of an LCD and a holographic optical element which works as a microlens array. The display surface of the proposed system is the virtual screen which is composed of multiple light focusing points (3D pixels) equally spaced in a cylindrical shape. Therefore, the display surface is not the physical obstruction when observers touch 3D images directly. In order to verify the effectiveness of the proposed system, we constructed the 144-degree prototype system. The virtual cylindrical display surface was composed of 8 basic display units. The angle of view of each 3D pixel which formed the virtual cylindrical display surface was 15°, and each 3D pixel irradiated 6 light rays at 3° intervals. The diameter and the height of the virtual cylindrical display surface were 42.6 mm and 50 mm, respectively. A displayed 3D image was directly touchable and was observed from 144° directions.

### **Evaluation of motion compensation method for assessing the gastrointestinal motility using three dimensional endoscope**

Kayo YOSHIMOTO, Kenji YAMADA (Osaka University), Kenji WATANABE (Osaka University), Tetsuji FUJINAGA (Osaka University), Michiko KIDO (Osaka University), Toshiaki NAGAKURA (Osaka Electro-Communication University), Hideya TAKAHASHI, Hideki IJIMA (Osaka University), Masahiko TSUJII (Osaka University), Tetsuo TAKEHARA (Osaka University), and Yuko OHNO (Osaka University)

*Proc. SPIE Advanced Biomedical and Clinical Diagnostic and Surgical Guidance Systems XIV*, San Francisco, Feb. 13, Vol.9698, CD-ROM (2016).

Functional gastrointestinal disorders (FGID) are the most common gastrointestinal disorders. The term "functional" is generally applied to disorders where there are no structural abnormalities. Gastrointestinal

dysmotility is one of the several mechanisms that have been proposed for the pathogenesis of FGID and is usually examined by manometry, a pressure test. There have been no attempts to examine the gastrointestinal dysmotility by endoscopy. We have proposed an imaging system for the assessment of gastric motility using a three-dimensional endoscope. After we newly developed a three-dimensional endoscope and constructed a wave simulated model, we established a method of extracting three-dimensional contraction waves derived from a three-dimensional profile of the wave simulated model obtained with the endoscope. In the study, the endoscope and the wave simulated model were fixed to the ground. However, in a clinical setting, it is hard for endoscopists to keep the endoscope still. Moreover, stomach moves under the influence of breathing. Thus, three-dimensional registration of the position between the endoscope and the gastric wall is necessary for the accurate assessment of gastrointestinal motility. In this paper, we propose a motion compensation method using three-dimensional scene flow. The scene flow of the feature point calculated by obtained images in a time series enables the three-dimensional registration of the position between the endoscope and the gastric wall. We confirmed the validity of a proposed method first by a known-movement object and then by a wave simulated model.

### **Spin-pump-induced spin transport in a thermally-evaporated pentacene film**

Yasuo TANI, Yoshio TEKI and Eiji SHIKOH

*Applied Physics Letters*, Vol.107, pp.242406 (4 pages) (2015).

We report the spin-pump-induced spin transport properties of a pentacene film prepared by thermal evaporation. In a palladium(Pd)/pentacene/ $\text{Ni}_{80}\text{Fe}_{20}$  tri-layer sample, a pure spin-current is generated in the pentacene layer by the spin-pumping of  $\text{Ni}_{80}\text{Fe}_{20}$ , which is independent of the conductance mismatch problem in spin injection. The spin current is absorbed into the Pd layer, converted into a charge current with the inverse spin-Hall effect in Pd, and detected as an electromotive force. This is clear evidence for the pure spin current at room temperature in pentacene films prepared by thermal evaporation.

### **Carrier Concentration Dependence of Spin Transport in P-Si Induced by Spin Pumping**

Hiroki KURIYAMA, Kazuki KUBO (Osaka University), Yoshio TEKI, Hiroaki TSUJIMOTO, Masashi SHIRAIISHI (Kyoto University), and Eiji SHIKOH

*IUMRS-ICEM 2016 4-8 July, Singapore (2016), ICEM16-A-0879.*

Spin transport in the nondegenerate p-type Si with the carrier concentration  $N$  of  $1.0 \times 10^{17} \sim 1.0 \times 10^{19} \text{ cm}^{-3}$  has recently been achieved at room temperature. In this study, the  $N$  dependence of spin transport characteristic in the p-Si was studied including a degenerate Si with the  $N$  of  $1.0 \times 10^{20} \text{ cm}^{-3}$ . A  $\text{Ni}_{80}\text{Fe}_{20}$  (25 nm in thick) film as the spin current generator and a Pd (10 nm) wire as the spin current detector on p-Si substrates were separately formed by using laser lithography and electron-beam deposition systems. The gap length between the Pd wire and  $\text{Ni}_{80}\text{Fe}_{20}$  film  $L$  was set to be below 1  $\mu\text{m}$ . When the ferromagnetic resonance FMR of the  $\text{Ni}_{80}\text{Fe}_{20}$  was excited, a spin current was generated in the p-Si by the spin-pumping and the spin current was transport through the p-Si and absorbed into the Pd. Then, the spin current was converted to a charge current by the inverse spin-Hall effect (ISHE) in the Pd, and detected as an electromotive force. For the sample with the  $L$  of 586 nm, the output voltage of 0.25  $\mu\text{V}$  from the Pd wire was obtained under the FMR of the  $\text{Ni}_{80}\text{Fe}_{20}$  film with the microwave power of 200mW, and the inversion symmetry of the output voltage signs to the magnetization reversal of the  $\text{Ni}_{80}\text{Fe}_{20}$  film as an evidence of the ISHE has been shown. This phenomenon may be caused by high career doping concentration and/or thermal effect. The spin diffusion length of the p-Si with the  $N$  of  $1.0 \times 10^{20} \text{ cm}^{-3}$  was estimated to be 119 nm under an assumption of an exponential decay of the spin signals and its value was almost consistent with the values of other p-Si.

### **Spin Transport Characteristic of Thermally Evaporated Pentacene Films by Using Spin Pumping**

Yasuo TANI, Yoshio TEKI, and Eiji SHIKOH

*IUMRS-ICEM 2016 4-8 July, Singapore (2016), ICEM16-A-0922.*

Carbon-based molecules are promising materials from the viewpoint of spin transport because of the small spin-orbit interaction. The pentacene, which is known as a p-type organic semiconductor, has high conductivity and good crystallinity even in the evaporated films. In this study, the spin transport characteristic of thermally-evaporated pentacene films was investigated by using spin-pumping induced by ferromagnetic resonance (FMR). Pd/pentacene/ $\text{Ni}_{80}\text{Fe}_{20}$  trilayer samples were formed as follows: On a Si/SiO<sub>2</sub> substrate, a Pd layer (the thickness of 10 nm) was formed by using an electron-beam deposition

under a vacuum of  $<10^{-6}$  Pa. Next, pentacene molecules were thermally-evaporated. The pentacene layer thickness was varied between 0 to 100 nm. Finally, a  $\text{Ni}_{80}\text{Fe}_{20}$  layer (25 nm) was formed by using an EB deposition under a vacuum of  $<10^{-6}$  Pa. The pure spin current is injected into the Pd layer from the  $\text{Ni}_{80}\text{Fe}_{20}$  layer via the pentacene film under the FMR of the  $\text{Ni}_{80}\text{Fe}_{20}$  film. Then, the spin current is converted to a charge current due to the inverse spin-Hall effect (ISHE) in the Pd layer and detected as an electromotive force. For a control experiment, samples with a Cu layer instead of the Pd layer were prepared because Cu has smaller spin-orbit interaction than Pd. Output voltages from the samples with Pd were observed under the FMR of  $\text{Ni}_{80}\text{Fe}_{20}$  film and the output voltage sign was inverted at the magnetization reversal of the  $\text{Ni}_{80}\text{Fe}_{20}$  film. Meanwhile, no output voltages from the samples with Cu were observed under the FMR of the  $\text{Ni}_{80}\text{Fe}_{20}$  film. These indicate that the output voltage observed from the samples with the Pd is due to the ISHE. That is, spin transport in evaporated pentacene films was achieved at room temperature by using the spin-pumping.

### **Electromotive Forces Generated in Various Ferromagnetic Metal Films Under Their Ferromagnetic Resonance**

Kazunari KANAGAWA, Yoshio TEKI, and Eiji SHIKOH

*IUMRS-ICEM 2016 4-8 July, Singapore (2016), ICEM16-A-1079.*

In ferromagnetic  $\text{Ni}_{80}\text{Fe}_{20}$  films, an electromotive force due to the inverse spin-Hall effect (ISHE) in the  $\text{Ni}_{80}\text{Fe}_{20}$  film itself is generated under the ferromagnetic resonance (FMR) of the  $\text{Ni}_{80}\text{Fe}_{20}$  film. This can be used as a new power-saving technology of electronics devices by using high frequency electromagnetic waves in general environments. In this study, the characteristics of electromotive forces generated in ferromagnetic metal Fe, Co and  $\text{Ni}_{80}\text{Fe}_{20}$  films under the respective FMR conditions were investigated at room temperature. Rectangular-shaped thin film samples with the thickness of 25 nm were formed by using a DC sputtering system. Conducting wires for measuring the electromotive forces generated in the ferromagnetic films were directly connected to the both edges of the rectangular samples by using silver paste. A sample was set into a microwave cavity of an electron spin resonance system to excite the FMR. Electromotive forces were observed for all ferromagnetic metal samples under the respective FMR conditions. The obtained electromotive forces were analyzed by using an equation taking into account the ISHE, the anomalous Hall effect (AHE) in the ferromagnetic film, and so on. The AHE was dominantly detected from the Fe films, while the ISHE was dominant for the  $\text{Ni}_{80}\text{Fe}_{20}$  films. This tendency was almost consistent with a theoretical study of the spin-Hall conductivity of 3d-transition metals. The characteristic of electromotive forces generated in Co films was strongly affected to the experimental conditions.

*Applied Chemistry*

**Seawater Usable for Production and Consumption of Hydrogen Peroxide as a Solar Fuel**

Kentaro MASE, Masaki YONEDA, Yusuke YAMADA and Shunichi FUKUZUMI

*Nature Commun.*, Vol. 7, 11470 (7 pages) (2016)

Hydrogen peroxide ( $\text{H}_2\text{O}_2$ ) in water has been proposed as a promising solar fuel instead of gaseous hydrogen because of advantages on easy storage and high energy density, being used as a fuel of a one-compartment  $\text{H}_2\text{O}_2$  fuel cell for producing electricity on demand with emitting only dioxygen ( $\text{O}_2$ ) and water. It is highly desired to utilize the most earth-abundant seawater instead of precious pure water for the practical use of  $\text{H}_2\text{O}_2$  as a solar fuel. Here we show efficient photocatalytic production of  $\text{H}_2\text{O}_2$  from the most earth abundant seawater instead of precious pure water and  $\text{O}_2$  in a two-compartment photoelectrochemical cell using  $\text{WO}_3$  as a photocatalyst for water oxidation and a cobalt complex supported on a glassy-carbon substrate for the selective two-electron reduction of  $\text{O}_2$ . The concentration of  $\text{H}_2\text{O}_2$  produced in seawater reached 48 mM, which was high enough to operate an  $\text{H}_2\text{O}_2$  fuel cell.

**Photocatalytic Hydroxylation of Benzene by Dioxygen to Phenol with a Cyano-Bridged Complex Containing  $\text{Fe}^{\text{II}}$  and  $\text{Ru}^{\text{II}}$  Incorporated in Mesoporous Silica-Alumina**

Yusuke ARATANI, Kohei OYAMA, Tomoyoshi SUENOBU, Yusuke YAMADA and Shunichi FUKUZUMI

*Inorg. Chem.*, Vol. 55, pp. 5780-5786 (2016)

Photocatalytic hydroxylation of benzene to phenol has been achieved by using  $\text{O}_2$  as an oxidant as well as an oxygen source with a cyano-bridged polynuclear metal complex containing  $\text{Fe}^{\text{II}}$  and  $\text{Ru}^{\text{II}}$  incorporated in mesoporous silica-alumina ( $[\text{Fe}(\text{H}_2\text{O})_3]_2[\text{Ru}(\text{CN})_6]@\text{sAl-MCM-41}$ ). An apparent turnover number (TON) of phenol production per the monomer unit of  $[\text{Fe}(\text{H}_2\text{O})_3]_2[\text{Ru}(\text{CN})_6]$  was 41 for 59 h. The cyano-bridged polynuclear metal complex,  $[\text{Fe}(\text{H}_2\text{O})_3]_2[\text{Ru}(\text{CN})_6]$ , exhibited catalytic activity for thermal hydroxylation of benzene by  $\text{H}_2\text{O}_2$  in acetonitrile (MeCN), where the apparent TON of phenol production reached 393 for 60 h. The apparent TON increased to 2500 for 114 h by incorporating  $[\text{Fe}(\text{H}_2\text{O})_3]_2[\text{Ru}(\text{CN})_6]$  in sAl-MCM-41. Additionally,  $[\text{Fe}(\text{H}_2\text{O})_3]_2[\text{Ru}(\text{CN})_6]$  acts as a water oxidation catalyst by using  $[\text{Ru}(\text{bpy})_3]^{2+}$  (bpy = 2, 2'-bipyridine) and  $\text{Na}_2\text{S}_2\text{O}_8$  as a photosensitizer and a sacrificial electron acceptor as evidenced by  $^{18}\text{O}$ -isotope labeling experiments. Photoirradiation of an  $\text{O}_2$ -saturated MeCN solution containing  $[\text{Fe}(\text{H}_2\text{O})_3]_2[\text{Ru}(\text{CN})_6]@\text{sAl-MCM-41}$  and scandium ion provided  $\text{H}_2\text{O}_2$  formation, where photoexcited  $[\text{Ru}(\text{CN})_6]^{4-}$  moiety reduces  $\text{O}_2$  as indicated by laser flash photolysis measurements. Thus, hydroxylation of benzene to phenol using molecular oxygen photocatalyzed by  $[\text{Fe}(\text{H}_2\text{O})_3]_2[\text{Ru}(\text{CN})_6]$  occurred via a two-step route; 1) molecular oxygen was photocatalytically reduced to peroxide by using water as an electron donor, and then, 2) peroxide thus formed is used as an oxidant for hydroxylation of benzene.

**Homogeneous and Heterogeneous Photocatalytic Water Oxidation by Persulfate**

Shunichi FUKUZUMI, Jieun JUNG, Yusuke YAMADA, Takahiko KOJIMA and Wonwoo NAM

*Chem. Asian J.*, Vol. 11, pp. 1138-1150 (2016)

Photocatalytic water oxidation by persulfate ( $\text{Na}_2\text{S}_2\text{O}_8$ ) with  $[\text{Ru}(\text{bpy})_3]^{2+}$  (bpy = 2,2'-bipyridine) as a photocatalyst provides a standard protocol to study the catalytic reactivity of water oxidation catalysts. The yield of evolved oxygen per persulfate is regarded as a good index for the catalytic reactivity because the oxidation of bpy of  $[\text{Ru}(\text{bpy})_3]^{2+}$  and organic ligands of catalysts competes with the catalytic water oxidation. A variety of metal complexes act as catalysts in the photocatalytic water oxidation by persulfate with  $[\text{Ru}(\text{bpy})_3]^{2+}$  as a photocatalyst. The catalytic mechanisms are discussed for the homogeneous water oxidation catalysis. Some metal complexes are converted to metal oxide or hydroxide nanoparticles during the photocatalytic water oxidation by persulfate, acting as precursors for the actual catalysts. The catalytic reactivity of various metal oxides is compared based on the yield of evolved oxygen and turnover frequency. A heteropolynuclear cyanide complex is the best catalyst reported so far for the photocatalytic water oxidation by persulfate and  $[\text{Ru}(\text{bpy})_3]^{2+}$ , affording 100% yield of  $\text{O}_2$  per persulfate.

**Photocatalytic Production of Hydrogen Peroxide from Water and Dioxygen Using Cyano-Bridged Polynuclear Transition Metal Complexes as Water Oxidation Catalysts**

Yusuke ISAKA, Kohei OYAMA, Yusuke YAMADA, Tomoyoshi SUENOBU and Shunichi FUKUZUMI  
*Catal. Sci. Technol.*, Vol. 6, pp. 681-684 (2016)

Hydrogen peroxide was produced efficiently from water and dioxygen using  $[\text{Ru}^{\text{II}}(\text{Me}_2\text{phen})_3]^{2+}$  ( $\text{Me}_2\text{phen}$  = 4,7-dimethyl-1,10-phenanthroline) as a photocatalyst and cyano-bridged polynuclear transition metal complexes composed of Fe and Co as water oxidation catalysts in the presence of  $\text{Sc}^{3+}$  in water under visible light irradiation.

### **Production of Hydrogen Peroxide by Combination of Semiconductor-Photocatalysed Oxidation of Water and Photocatalytic Two-Electron Reduction of Dioxygen**

Yusuke ISAKA, Yusuke YAMADA, Tomoyoshi SUENOBU, Tatsuo NAKAGAWA and Shunichi FUKUZUMI

*RSC Adv.*, Vol. 6, pp. 42041-42044 (2016)

Production of hydrogen peroxide from water and dioxygen was achieved by combination of semiconductor-photocatalysed oxidation of water and photocatalytic two-electron reduction of dioxygen with  $[\text{Ru}^{\text{II}}(\text{MeO})_2\text{bpy}]_3^{2+}$  ( $(\text{MeO})_2\text{bpy}$  = 4,4'-dimethoxy-2,2'-bipyridine) in the presence of  $\text{Sc}^{3+}$  in water under visible light irradiation.

### **A Composite Catalyst of Pt Nanoparticles and an Organic Photocatalyst Incorporated in Interparticle Mesospaces of Silica-Alumina Nanoparticle Ensembles for Hydrogen Evolution in Water**

Yusuke YAMADA, Hideyuki TADOKORO, Masood NAQSHBANDI, John CANNING, Maxwell J. CROSSLEY, Tomoyoshi SUENOBU and Shunichi FUKUZUMI

*ChemPlusChem*, Vol. 81, pp. 521-525 (2016)

Room temperature self-assembly is used to fabricate a periodic array of uniformly sized  $\text{Al}^{3+}$ -doped  $\text{SiO}_2$  nanoparticles ( $\text{Al-SiO}_2\text{NPs}$ , 20-30 nm). The uniform mesoporous structure is suitable for uniformly incorporating and distributing Pt nanoparticles (PtNPs), which are used as hydrogen evolution catalysts in artificial photosynthetic systems, without agglomeration during the catalytic reaction. When the surfaces of the  $\text{Al-SiO}_2\text{NPs}$  are covered with an organic photocatalyst (2-phenyl-4-(1-naphthyl)quinolinium ion,  $\text{QuPh}^+-\text{NA}$ ), each PtNP is surrounded by multiple  $\text{QuPh}^+-\text{NA}$  ions. The structure allows the PtNP to receive multiple electrons from  $\text{QuPh}^+-\text{NA}$  molecules, which are generated by reduction of the photoexcited state of  $\text{QuPh}^+-\text{NA}$  ions ( $\text{QuPh}^+-\text{NA}^+$ ) with  $\beta$ -dihydronicotinamide adenine dinucleotide (NADH), resulting in efficient photocatalytic  $\text{H}_2$  evolution.

### **Metal-Free Hydrogen Evolution with Nanoparticles Derived from Pyrene via Two-Photon Ionization Induced by Laser Irradiation**

Kei OHKUBO, Naoki KOHNO, Yusuke YAMADA and Shunichi FUKUZUMI

*Chem. Commun.*, Vol. 51, pp. 11515-11518 (2015)

Laser irradiation of a cyclohexane solution containing pyrene resulted in hydrogen evolution as pyrene was converted to a metal-free nanoparticle photocatalyst. When  $\text{C}_6\text{H}_{12}$  was replaced by  $\text{C}_6\text{D}_{12}$ ,  $\text{D}_2$  was mainly evolved. This result suggests that hydrogen source is cyclohexane used as a solvent. Photocatalytic hydrogen evolution was also observed in an aqueous solution by using a water-soluble pyrene derivative.

### **New Developments of X-Ray Fluorescence Imaging Techniques in Laboratory**

Kouichi TSUJI, Tsuyoshi MATSUNO, Yuki TAKIMOTO, Masaki YAMANASHI, Noritsugu KOMETANI, Yuji C. SASAKI, Takeshi HASEGAWA, Shuichi KATO, Takashi YAMADA, Takashi SHOJI and Naoki KAWAHARA

*Spectrochim. Acta Part B*, Vol.113, pp. 45-53 (2015)

X-ray fluorescence (XRF) analysis is a well-established analytical technique with a long research history. Many applications have been reported in various fields, such as in the environmental, archeological, biological, and forensic sciences as well as in industry. This is because XRF has a unique advantage of being a nondestructive analytical tool with good precision for quantitative analysis. Recent advances in XRF analysis have been realized by the development of new x-ray optics and x-ray detectors. Advanced x-ray focusing optics enables the making of a micro x-ray beam, leading to micro-XRF analysis and XRF imaging. A confocal micro-XRF technique has been applied for the visualization of elemental distributions inside the samples. This technique was applied for liquid samples and for monitoring chemical reactions such as the

metal corrosion of steel samples in the NaCl solutions. In addition, a principal component analysis was applied for reducing the background intensity in XRF spectra obtained during XRF mapping, leading to improved spatial resolution of confocal micro-XRF images. In parallel, the authors have proposed a wavelength dispersive XRF (WD-XRF) imaging spectrometer for a fast elemental imaging. A new two dimensional x-ray detector, the Pilatus detector was applied for WD-XRF imaging. Fast XRF imaging in 1 s or even less was demonstrated for Euro coins and industrial samples. In this review paper, these recent advances in laboratory-based XRF imaging, especially in a laboratory setting, will be introduced.

### **Study of Metal Release from Stainless Steels in Simulated Food Contact by Means of Total Reflection X-Ray Fluorescence**

Rogerta DALIPI, Laura BORGESSE, Andrea CASAROLI, Marco BONIARDI, Ursula FITTSCHEN, Kouichi TSUJI and Laura E. DEPERO

*Journal of Food Engineering*, Vol.173, pp. 85-91 (2016)

This study shows a reliable procedure to prescribe the preferential use of a material for food contact. Release tests with optimized parameters were performed on six different stainless steel accepted for the use in food contact: AISI 420, AISI 430, AISI 202, AISI 303, AISI 304, and AISI 316. Total reflection X-ray fluorescence spectroscopy was used to measure the concentration of Cr, Mn and Ni in contact solutions from release tests. Results show that AISI 202 and 430 release the lowest amount of Mn, Cr and Ni. While, AISI 420 is the worst material, exceeding the limit set in the Italian regulation for all the three metals of interest. One sample was selected to test the reproducibility of TXRF measurements performed in three different laboratories around the world. Results show that quantitative analyses by means of TXRF satisfy the requirements of this field of application.

### **Visualizing a Black Cat Drawing Hidden inside the Painting by Confocal Micro-XRF Analysis**

Kazuhiko NAKANO, Atsushi TABE, Susumu SHIMOYAMA and Kouichi TSUJI

*Microchemical Journal*, Vol.126, pp. 496-500 (2016)

Identification of pigments is one of the essential issues for the painting restoration or art appraisal. We investigated the nondestructive 3D elemental analysis of a paint sample using a confocal 3D-XRF spectrometer. The confocal 3D-XRF spectrometer combined with two polycapillary X-ray lenses was constructed in the laboratory. To confirm the analytical performance of the confocal 3D-XRF spectrometer, we analyzed several pigment mixtures of Emerald green (EG) and Prussian blue (PB). XRF intensities of Cu and Fe in the pigment mixtures showed good correlation with the content percentage of PB. In addition, we analyzed the replica paint in Daubigny's garden by Vincent Van Gogh to visualize a hidden painting beneath the surface. 3D elemental map of Fe by confocal 3D-XRF showed characteristic distributions indicating the PB. The obtained 3D-XRF intensity imaging reflected the distribution of specific elements in the paint layers resulting in the successful visualization of the hidden cat.

### **Homogeneity of Reference Material for X-Ray Fluorescence Analysis and Application to Micro X-Ray Fluorescence Spectroscopy**

Masaki YAMANASHI, Atsushi GOTO and Kouichi TSUJI

*Adv. X-ray. Chem. Anal., Japan*, Vol.47, pp. 263-270 (2016) (in Japanese)

X-ray fluorescence analysis is widely applied for measuring steel samples because qualitative and quantitative analysis is performed. Recently, X-ray focus optics and X-ray analysis spectrometer are significantly developed. Micro X-ray fluorescence spectrometer with attached X-ray focus optics is used to obtain information of elements in micro area. When quantitative analysis is performed by using X-ray analysis spectrometers, reference materials described the purpose for uses (evaluation of chemical, instrumental methods of analysis and calibration of instrumental methods of analysis) are needed. The certificate of reference materials for X-ray fluorescence analysis does not ensure to apply to micro X-ray fluorescence spectroscopy. Actually, it is known that small inclusions produced in manufacturing process are included in steel reference materials. The segregation in micro size exists in steel reference materials. Since the analytical area of micro X-ray fluorescence spectrometer is micro scale, the segregation in micro size affects the analytical values. In this study, we studied the influence of inclusions to quantitative micro XRF analysis in calibration method. In order to resolve the problem by micro inclusion, multipoint and area analyses were applied. These analysis methods reduced the influence of micro inclusions in steel reference

materials.

### **Calculation of Fluorescent X-Ray Intensity for Confocal Micro XRF Analysis**

Naoki KAWAHARA, Tsuyoshi MATSUNO and Kouichi TSUJI

*Adv. X-ray. Chem. Anal., Japan*, Vol.47, pp. 293-300 (2016) (in Japanese)

Intensities of fluorescent X-rays from a composite block of Cu and Fe with a vertical border in a confocal micro-XRF configuration are calculated by a simple model but with absorption and secondary excitation effects considered. The simulation indicated that only the secondary excited fluorescent X-rays can be observed with a confocal point outside the sample. Experimental evaluations were also performed and the simulation and the measurements are qualitatively agreed at some points.

### **TXRF Intensity Dependence on Position of Dried Residue on Sample Carrier and TXRF Determination of Halogen in Liquid Samples**

Yuri TABUCHI and Kouichi TSUJI

*X-Ray Spectrometry*, Vol.45, pp. 197-201 (2016)

Total reflection X-ray fluorescence (TXRF) spectroscopy is an effective technique for simultaneous multi-elemental trace analysis of a small volume of a sample placed on a flat substrate. An internal standard method is usually applied for quantitative TXRF analysis of liquid samples such as drinking water and environmental samples. However, it was difficult to determine Cl and Br because they were lost as volatile hydrogen halide compounds by adding an acid internal standard solution. Thus, we attempted to apply the traditional calibration curve method for the determination of halogens without internal standard. If internal standard method is not applied, the TXRF intensity drastically changes depending on the relative position of the dried residue to the detector. Therefore, we investigated the relationship between TXRF intensity and the position of dried residue relative to the detector. As a result, it was confirmed that TXRF intensity critically depended on the position of the dried residue on the sample carrier. The position of the droplet of the sample solution was carefully controlled by using an air blower in order to place the dried residue at the most effective position on the sample carrier. We could successfully make a calibration curve for Cl with a good relationship without internal standard. Finally, Cl in the NaCl solutions (0-5ppm, 10 $\mu$ l) was successfully determined by the calibration curve method using a table-top TXRF instrument. The limit of detection of Cl was 63 ppb (ng/ml).

### **Secondary Excitation Observed in Lateral Scan Using Confocal Micro-XRF**

Naoki KAWAHARA, Tsuyoshi MATSUNO, Yuki TAKIMOTO and Kouichi TSUJI

*Advances in X-ray Analysis*, Vol.59, pp. 77-84 (2016)

The vertical border of Cu and Fe blocks was measured by the confocal micro-XRF method. A lateral scan near the border was performed at different depths. Characteristic secondary excitation of iron was observed in the Fe K $\alpha$  intensity profile at 40  $\mu$ m in depth, while it was not observed by lateral scan near the surface. In addition, we simulated the XRF intensity to explain the lateral scan profiles as the confocal position changed. The simulated results qualitatively agreed with experimental profiles. Furthermore, the simulation indicated the possibility of observing secondary excitation intensity separately from primary excitation intensity with the sample structure of this study.

### **Sample Preparation for TXRF Analysis of Metal Particles in Used Machine Oils and Preliminary Research for Application of Principal Component Analysis**

Tsuyoshi MATSUNO, Yuri TABUCHI, Ryohei HOSOMI, Takeshi HASEGAWA, Noritsugu KOMETANI and Kouichi TSUJI

*Advances in X-ray Analysis*, Vol.59, pp. 112-119 (2016)

Total reflection x-ray fluorescence (TXRF) is well known as a trace analysis. When used vacuum pump oil was measured by TXRF, quantitative TXRF analysis was difficult with internal standard technique because homogeneous solution was not obtained. Thus, a surfactant was added to the sample to mix the oil and the solution homogeneously. As a result, quantitative values were obtained for particles in oil by TXRF internal standard method. TXRF spectra have still small background. Thus, we considered to apply principal component analysis (PCA) for noise reduction from the spectra. Several spectra were obtained at different glancing angles. The eigenvalues and eigenvectors were calculated for TXRF spectra matrix using Scilab

software. The noise components were found from the contributing rate of eigenvalues. Removing the noise components, the new data set was obtained. Finally the re-constructed spectra were obtained with smoother background.

#### **WD-XRF Imaging with Polycapillary Optics under Glancing Incidence Geometry**

Yuki TAKIMOTO, Masaki YAMANASHI, Shuichi KATO, Takashi SHOJI, Noritsugu KOMETANI and Kouichi TSUJI

*Advances in X-ray Analysis*, Vol.59, pp. 120-124 (2016)

A new wavelength-dispersive X-ray fluorescence (WD-XRF) imaging spectrometer equipped with a highly sensitive two-dimensional detector was developed in our laboratory. In this spectrometer, a straight type polycapillary optic was applied instead of a Soller slit which is used in conventional WD-XRF spectrometers. The straight type polycapillary optic worked as a 2D collimator for fluorescent X-rays to keep the information of the elemental distribution in the sample. The primary X-rays were irradiated to the sample at glancing angles. Fluorescent X-rays were introduced to the analyzing crystal (LiF(200)). Analyzing element could be selected by adjusting the diffraction angle. XRF images were successfully obtained with a short exposure time less than 1 s. This WD-XRF image was obtained under glancing incidence condition. It was confirmed that surface sensitivity for XRF elemental imaging was improved under glancing incidence geometry.

#### **X-Ray Fluorescence Analysis (Chapter 11-1)**

Kouichi TSUJI

In *A Guide to Synchrotron Radiation Science*, edited by Makoto Watanabe, Shigeo Sato, Ian Munro and G. S. Lodha, Narosa Publishing House Pvt. Ltd. (2016)

#### **Soft and Hard X-Ray Microscopes and Their Applications (Chapter 14-2-2)**

Kouichi TSUJI

In *A Guide to Synchrotron Radiation Science*, edited by Makoto Watanabe, Shigeo Sato, Ian Munro and G. S. Lodha, Narosa Publishing House Pvt. Ltd. (2016)

#### **Total Reflection X-Ray Fluorescence Analysis (Chapter 8)**

Kouichi TSUJI

In *The 2<sup>nd</sup> edition "Practical X-ray Fluorescence Analysis"*, edited by Izumi Nakai, Asakura Publishing Co., Ltd. (2016) (in Japanese)

#### **Grazing Emission X-Ray Fluorescence Analysis (Chapter 14-1)**

Kouichi TSUJI

In *The 2<sup>nd</sup> edition "Practical X-ray Fluorescence Analysis"*, edited by Izumi Nakai, Asakura Publishing Co., Ltd. (2016) (in Japanese)

#### **Polycapillary X-Ray Lens and Micro X-Ray Fluorescence Analysis (Chapter 14-2)**

Kouichi TSUJI

In *The 2<sup>nd</sup> edition "Practical X-ray Fluorescence Analysis"*, edited by Izumi Nakai, Asakura Publishing Co., Ltd. (2016) (in Japanese)

#### **Confocal Micro X-Ray Fluorescence Analysis (Chapter 14-3)**

Kouichi TSUJI

In *The 2<sup>nd</sup> edition "Practical X-ray Fluorescence Analysis"*, edited by Izumi Nakai, Asakura Publishing Co., Ltd. (2016) (in Japanese)

#### **Advanced Treatment of Polluted Water Containing Chlorinated Organic Compounds by the Hydrothermal Oxidation Technique Using Copper Oxide Catalyst**

Noritsugu KOMETANI, Reina TAKAMI and Kyohei NAKAO

*Japanese Journal of Multiphase Flow*, Vol.29, No.4, pp.302-308 (2015).

It has been revealed that hydrothermal oxidation of persistent organochlorine substances is dramatically

facilitated with the aid of Cu-based catalysts such as Cu-supported  $\text{WO}_3$ , because the Fenton-type reaction catalyzed by Cu ions undergoes substantial acceleration under subcritical conditions of water at around 200–300°C, leading to the increased formation of hydroxyl radicals which possess a strong oxidative power. In this study, the catalytic hydrothermal oxidation of 4-chlorophenol with CuO or  $\text{Cu}_2\text{O}$  has been examined using the slurry flow and catalyst packed-bed reactor systems. It is found that  $\text{Cu}_2\text{O}$  has a remarkable catalytic activity for the hydrothermal oxidation of 4-chlorophenol compared with those of CuO and Cu-supported  $\text{TiO}_2$ . The conversion of 4-chlorophenol reached nearly 100% at reaction temperatures around 130°C when  $\text{Cu}_2\text{O}$  was used as catalyst, indicating that it is possible to substantially reduce the reaction condition required for the complete decomposition of persistent organochlorine substances by the hydrothermal oxidation. The continuous treatment of 4-chlorophenol has been also conducted using the packed-bed reactor system with  $\text{Cu}_2\text{O}$ . The results demonstrated that 4-chlorophenol could be degraded for up to 22 hours without significant loss of the catalytic activity.

### **Reaction Mechanism of the Oxidative Decomposition of Organochlorine Compounds By Fenton-like Reaction in Subcritical Water**

Noritsugu KOMETANI, and Reina TAKAMI

*Proceedings of 2015 AIChE Annual Meeting*, Salt Lake City, USA, November 8-13 (2015)

We have developed new technique to treat polluted water containing recalcitrant organochlorine compounds by combination of hydrothermal oxidation and Fenton-like reaction using  $\text{Cu}_2\text{O}$  as a catalyst. In this study, the treatment of model polluted water containing 4-chlorophenol (CP) was conducted using the slurry flow reactor system and the reaction mechanism of oxidative decomposition of CP was investigated. The mixed suspension containing CP,  $\text{Cu}_2\text{O}$  and  $\text{H}_2\text{O}_2$  was reacted with pressure, temperature and flow rate controlled at 10 MPa, 133–200°C and 1.0–16.0 ml/min, respectively. It was found that the enhancement of CP decomposition by  $\text{Cu}_2\text{O}$  catalyst was highest at 166°C. According to the calculation of the rate of  $\text{H}_2\text{O}_2$  conversion, it was found that the rate of Fenton-like reaction was almost independent of the reaction temperature and the thermal decomposition of  $\text{H}_2\text{O}_2$  became dominant at higher temperatures.

### **Photocatalytic Reduction of $\text{CO}_2$ by Pt-Loaded $\text{TiO}_2$ in the Mixture of Sub- and Supercritical Water and $\text{CO}_2$**

Noritsugu KOMETANI, Shoutarou HIRATA, and Masashi CHIKADA

*11th International Symposium on Supercritical Fluids*, Invited Lecture, Seoul, South Korea, October 11-14, 2015; Preprints.

### **Anti-Selective Asymmetric Nitro-Michael Reaction of Furanones: Diastereocontrol by Catalyst**

Tohru SEKIKAWA, Takayuki KITAGUCHI, Hayato KITAURA, Tatsuya MINAMI and Yasuo HATANAKA  
*Org. Lett.*, Vol. 18, pp. 646-649 (2016)

Catalyst-controlled switching of diastereoselectivity from the high syn-selectivity (>98 dr, syn) to the anti-selectivity (up to 96/4 dr, anti) of the asymmetric nitro-Michael reaction of furanones is described. Anti-diastereoselectivity of the nitro-Michael reaction has been very rare. With 0.1-5 mol % loadings of epi-quinine catalyst, the reaction of 5-substituted 2(3-H)-furanones with nitroalkenes smoothly proceeded to give the anti-Michael adducts in good yields (up to 95%) with excellent diastereo- and enantioselectivity (up to 96/4 dr, anti; up to 99% ee). DFT calculation was carried out to account for the high anti-diastereoselectivity.

### **Syn-Selective Nitro-Michael Addition of Furanones to $\beta,\beta$ -Disubstituted Nitroalkenes Catalyzed by Epi-Quinine Derivatives**

Tohru SEKIKAWA, Hayato KITAURA, Takayuki KITAGUCHI, Tatsuya MINAMI, Yasuo HATANAKA  
*Tetrahedron Lett.*, Vol. 57, pp. 2985-2988 (2016)

Epi-quinine-catalyzed asymmetric nitro-Michael addition of furanones to  $\beta,\beta$ -disubstituted nitroalkenes is described. The reaction proceeded smoothly with 1-5 mol % loadings of epi-quinine catalysts at room temperature, giving the corresponding Michael adducts in high yields (72-93%) with extremely high diastereo- and enantioselectivities (>98/2 dr, syn major; 95-99% ee). This reaction provides an effective and straightforward method for constructing all-carbon quaternary stereogenic centers adjacent to oxygen-containing quaternary stereogenic centers.

### **Oxygen Additive Amount Dependence of Rate of Photoresist Removal by H Radicals Generated on a Tungsten Hot-Wire Catalyst**

Masashi YAMAMOTO, Hironobu UMEMOTO, Keisuke OHDAIRA, Tomokazu SHIKAMA, Takashi NISHIYAMA and Hideo HORIBE

*Jpn. J. Appl. Phys.*, Vol. 55, 076503 (2016)

We examined an environmentally friendly photoresist removal method using radicals produced by decomposing mixtures of hydrogen and oxygen on a hot tungsten catalyst. The photoresist removal rate increased with the oxygen additive amount (the flow rate ratio of oxygen to hydrogen) up to an optimal amount and then decreased gradually. When the catalyst temperature was 1600 °C, the optimal oxygen additive amount was 1.0% and the removal rate was 1.7 times higher than that in the pure hydrogen system. At 2000 °C, the optimal amount increased to 2.5% but the increase ratio decreased by 1.3 times. At high catalyst temperatures, the absolute removal rate as well as the optimal oxygen additive amount is high, but the increase ratio is low. At the optimal oxygen additive amount, H, O, and OH radicals may exert their effects together to decompose photosensitive polymers.

### **Removal Technology of Poly-Vinyl Phenol Using Laser Irradiation**

Tomosumi KAMIMURA, Kosuke KUNO, Yuta KUROKI, Takayuki YAMASHIRO, Shingo TSUJIMOTO, Ryosuke NAKAMURA, Seiji TAKAGI, Takashi NISHIYAMA and Hideo HORIBE

*J. Photopolym. Sci. Technol.*, Vol. 29, pp. 633-637 (2016)

Removal by using laser irradiation was investigated in Poly-Vinyl Phenol (PVP). The laser irradiation in the water can improve the PVP stripping effect as compared with that of normal atmosphere irradiation. The surface laser damage threshold of Si wafer was 0.13 J/cm<sup>2</sup>, and the PVP stripping threshold was 0.06 J/cm<sup>2</sup>. The PVP stripping threshold decreased to approximately 50% of the surface laser damage threshold. The PVP strips from the Si wafer just as shown in a positive-tone DNQ / novolak resist. However, removal efficiency decreased at a large irradiation beam diameter. The stripped area decreases at the beam diameter of 1.5 mm or more. Irradiation with multiple laser beams with a small beam diameter could improve the PVP stripping rate with high efficiency.

### **Enhancement of Removal Uniformity by Oxygen Addition for Photoresist Removal Using H Radicals Generated on a Tungsten Hot-Wire Catalyst**

Masashi YAMAMOTO, Kazuma MAEJIMA, Hironobu UMEMOTO, Keisuke OHDAIRA, Tomokazu SHIKAMA, Takashi NISHIYAMA and Hideo HORIBE

*J. Photopolym. Sci. Technol.*, Vol. 29, pp. 639-642 (2016)

We examined an environmentally friendly photoresist removal method using radicals produced by decomposing a mixture of hydrogen and oxygen on hot tungsten catalysts. Results show that the photoresist removal uniformity is enhanced remarkably with the optimal amount of oxygen addition. By further optimizing conditions, the removal uniformity and the inclusive removal rate might become comparable to those achieved when chemicals are used.

### **Effects of Oxygen Microbubbles on Photoresist Layers under Hot Water Conditions**

Masayoshi TAKAHASHI, Yasuyuki SHIRAI, Akinobu TERAMOTO, Tunejiro TAKAHASHI, Katsumi TATERA, Kohei MATSUURA and Hideo HORIBE

*J. Photopolym. Sci. Technol.*, Vol. 29, pp. 643-646 (2016)

We need to enhance the removing ability of microbubbles through the clear understanding of the functional mechanisms of microbubbles for the removal of photoresist layers. The purpose of the present study is to clarify the effect of microbubble on the surface of photoresist layers.

### **Effect of Temperature on Degradation of Polymers for Photoresist Using Ozone Microbubbles**

Kohei MATSUURA, Takashi NISHIYAMA, Eriko SATO, Masashi YAMAMOTO, Tomosumi KAMIMURA, Masayoshi TAKAHASHI, Kunihiko KOIKE and Hideo HORIBE

*J. Photopolym. Sci. Technol.*, Vol. 29, pp. 623-627 (2016)

We studied about an effect of temperature on degradation of polymers for photoresist using ozone microbubbles as an environmentally friendly cleaning technique. The dissolved ozone concentration of ozone microbubbles was decreased with the increasing temperature because the solubility of ozone gas was decreased and self-decomposition of ozone in water was promoted. While the reactivity between ozone and novolak resin was increased with the increasing temperature. Consequently, novolak resin was most efficiently removed at around 23 °C. The activated energy for removal of novolak resin using ozone microbubbles was 23 kJ/mol determined from Arrhenius plots. Polyvinyl phenol was removed by ozone microbubbles, and its removal rate was comparable with that of novolak resin. Polymethyl methacrylate

without C=C bond or benzene ring structure could not be removed by ozone microbubbles.

### **Decomposition Process of PMMA-Based Polymer Using Atomic Hydrogen Generated by a Tungsten Hot-Wire Catalyst**

Seiji TAKAGI, Takashi NISHIYAMA, Masashi YAMAMOTO, Eriko SATO, Tomosumi KAMIMURA, Toshiyuki OGATA and Hideo HORIBE

*J. Photopolym. Sci. Technol.*, Vol. 29, pp. 629-631 (2016)

We investigated the formation of microstructure on the surface of Poly(methyl methacrylate)-based polymer (PMMA-based polymer), which is a polymer for the ArF photoresist, in decomposition process by using atomic hydrogen generated by a tungsten hot-wire catalyst.

### **Crystalline Structure Control of Poly(vinylidene fluoride) Films with the Antisolvent Addition Method**

Takashi NISHIYAMA, Takayuki SUMIHARA, Yasutaka SASAKI, Eriko SATO, Masafumi YAMATO and Hideo HORIBE

*Polym. J.*, in press (DOI:10.1038/pj.2016.62)

In this paper, we demonstrate a simple method for the preparation of poly(vinylidene fluoride) (PVDF) films by antisolvent addition performed by immersing a PVDF solution casted substrate into antisolvents for PVDF such as deionized water and the control of their crystalline structure. A PVDF film was easily obtained for approximately two hours in the evaporation process, and PVDF  $\beta$  phase could be obtained by utilizing hexamethylphosphoramide and propylene carbonate as good solvents for PVDF. The crystalline structure of the PVDF films changed in the order of  $\alpha$ ,  $\gamma$  and  $\beta$  phases with increasing dipole moment of good solvents for PVDF. It was found that the crystalline structure of the PVDF films prepared was strongly affected by the electrostatic interaction between PVDF polymer chain and good solvents for PVDF in the antisolvent addition.

### **Quantification of Positive Temperature Coefficient Effect on Polymers Filling with Conductive Particles**

Takashi NISHIYAMA, Eriko SATO, Masafumi YAMATO and Hideo HORIBE

*Seikei-Kakou*, accepted (in Japanese)

Polymer composites filled with conductive particles such as metal, carbon black (CB) and nanotube (CNT) exhibit electro conductivity, and their resistivity significantly increases with raising temperature. Particularly, semicrystalline polymer composites possess superior electro conductivity and positive temperature coefficient (PTC) effect, because conductive particles effectively connect by localizing in the amorphous phase and disconnect by a greater volume expansion near the melting point. In this study, we quantitatively analyzed the PTC effect of various composites consisting of semi- or non-crystalline polymers filled with metal or carbon particles by calculating their filler contents considering thermal volume expansion rate and degree of crystal, as a guideline for design of sensor and circuit protection devices. The revised filler content at room temperature,  $\phi$  (R.T.) of poly(vinylidene fluoride) (PVDF)/nickel, CB and CNT as semicrystalline polymer composites became higher than the amount of filler loading in preparation and drastically decreased as temperature increased. In contrast,  $\phi$  (R.T.) of poly(methyl methacrylate) (PMMA)/ CB and CNT as noncrystalline polymer composites gradually decreased with temperature. The rate of the revised filler content at PTC,  $\phi$  (PTC) and  $\phi$  (R.T.) at various amounts of filler loading in preparation was a constant value in each composite, and  $\phi$  (PTC)/ $\phi$  (R.T.) values of PVDF/Ni, PVDF/CB, PVDF/CNT, PMMA/CB and PMMA/CNT were 0.93, 0.78, 0.74, 0.95 and 0.96, respectively. These values indicate the filler content necessary to occurring PTC effect. In comparison of each  $\phi$  (PTC)/ $\phi$  (R.T.) value, semicrystalline polymer and carbon filler systems were lower. The results well represent the effect of particle localization in the amorphous phase of semicrystalline polymer and strong interaction of carbon nanofillers for the PTC characteristics.

### **Liquid Marbles as a Micro-Reactor for Efficient Radical Alternating Copolymerization of Diene Monomer and Oxygen**

Eriko SATO, Michihiro YURI, Syuji FUJII, Takashi NISHIYAMA, Yoshinobu NAKAMURA and Hideo HORIBE

*Chem. Commun.*, Vol. 51, pp. 17241-17244 (2015)

Liquid marbles have been shown to be a novel micro-reactor to synthesize polyperoxides by the radical alternating copolymerization of the 1,3-diene monomer with oxygen in a good yield. Oxygen gas is effectively absorbed as a comonomer by the large and permeable gas-liquid interface of the liquid marbles.

### **Liquid Marble Containing Degradable Polyperoxides for Adhesion Force-Changeable Pressure-Sensitive Adhesives**

Eriko SATO, Michihiro YURI, Syuji FUJII, Takashi NISHIYAMA, Yoshinobu NAKAMURA and Hideo HORIBE

*RSC Adv.*, Vol. 6, pp. 56475-56482 (2016)

Liquid marbles containing a sticky polyperoxide were prepared by the in-situ copolymerization of the 1,3-diene monomer with oxygen. The as-prepared liquid marbles had a non-sticky nature and could move on any substrates due to the presence of hard particles on their surfaces, while the squeezed liquid marble developed adhesion force-tunable PSA properties due to the outflow of the inner materials. The 180° peel strength of the squeezed liquid marble increased by heating at 90 °C for 1 h or by UV irradiation at 0.86 J/cm<sup>2</sup> because the cohesive force of the adhesive layer increased by the additional polymerization initiated by moderate decomposition of the polyperoxide. The increased 180° peel strengths were significantly decreased again to almost zero, i.e., dismantling, after an additional heating at 150 °C for 1 h because of an excess increase in the cohesive force as pressure-sensitive adhesives, where cross-linking took place as a result of significant decomposition of the polyperoxide accompanied by hydrogen abstraction and coupling.

### **Dismantlable Adhesion Properties of Reactive Acrylic Copolymers Resulting from Cross-linking and Gas Evolution**

Eriko SATO, Shusei IKI, Keisuke YAMANISHI, Hideo HORIBE and Akikazu MATSUMOTO

*J. Adhes.*, in press (DOI:10.1080/00218464.2016.1209114)

The acrylic copolymers involving 2-hydroxyethyl acrylate (HEA) and *tert*-butyl acrylate (tBA) units as reactive units behave as pressure-sensitive adhesive type dismantlable adhesive materials. In order to clarify the individual role of HEA and tBA units on dismantlability, the 180° peel behavior after the dismantling treatment, i.e., heating in the presence of given amount of acid catalysts, was systematically investigated using the acrylic copolymers involving different amounts of the reactive units. It was revealed that transesterification of HEA units resulted in an increase in the cohesive force and modulus due to an increase in the molecular weight and cross-linking. Deprotection of tBA units, i.e, transformation of tBA to acrylic acid unit with isobutene evolution, promoted cross-linking by the esterification of acrylic acid units and tended to reduce a cohesive force by forming voids in the adhesive layer due to the evolution of isobutene gas. Interfacial failure in the peel tests corresponded with a high degree of cross-linking and increased modulus of the adhesive. Conversely, cohesive failure was associated with reduced cohesive strength of the adhesive layer and a low peel strength.

### **Living Radical Polymerization of Diisopropyl Fumarate To Obtain Block Copolymers Containing Rigid Poly(substituted methylene) and Flexible Polyacrylate Segments**

Akikazu MATSUMOTO, Naoki MAEO and Eriko SATO

*J. Polym. Sci., Part A: Polym. Chem.*, Vol. 54, pp. 2136-2147 (2016)

Living radical polymerizations of diisopropyl fumarate (DiPF) are carried out to synthesize poly(diisopropyl fumarate) (PDiPF) as a rigid poly(substituted methylene) and its block copolymers combined with a flexible polyacrylate segment. Reversible addition-fragmentation chain transfer (RAFT) polymerization is suitable to obtain a high-molecular-weight PDiPF with well-controlled molecular weight, molecular weight distribution, and chain-end structures, while organotellurium-mediated living radical polymerization (TERP) and reversible chain transfer catalyzed polymerization (RTCP) give PDiPF with controlled chain structures under limited polymerization conditions. In contrast, controlled polymerization for the production of high-molecular-weight and well-defined PDiPF is not achieved by atom transfer radical polymerization (ATRP) and nitroxide-mediated radical polymerization (NMP). The block copolymers consisting of rigid poly(substituted methylene) and flexible polyacrylate segments are synthesized by the RAFT polymerization.

### **Design of Debonding Processes for Quick Dismantlable Adhesion System**

Yusuke FUKAMOTO, Takuya ASHIDA, Haruyuki OKAMURA, Eriko SATO, Hideo HORIBE and Akikazu MATSUMOTO

*Journal of The Adhesion Society of Japan*, Vol. 52, pp. 198-207 (2016) (in Japanese)

Dismantlable adhesion system responsible to photoirradiation and postbaking as the dual-type external stimuli is a new adhesion technique satisfying adhesive reliability during use and facile debonding after use. However, this system includes a two-step process for debonding requiring a relatively long time, typically,

more than several ten minutes. Further development of quick debonding process is indispensable for the use of this system in various application fields. In this study, we report quick dismantlable adhesion systems using random and block copolymers containing *tert*-butyl acrylate segment as the reactive segment and 2-ethylhexyl and 2-hydroxyethyl acrylates as the adhesive segment. The quick dismantling system within 1 minute was established by the use of LED as the photoirradiation source and a new photoacid generator (PAG) corresponding to the wavelength of the used UV light for debonding and the optimization of dismantling conditions such as the PAG concentration, heating temperature, and photoirradiation dose. A simultaneous photoirradiation and heating process was also revealed to be valid for a decrease in the adhesion strength enough to realize quick dismantling within 1 minute.

### **Control of Droplet Movement on an Inclined Wall by Difference of Wettability**

Kenji KATO, Hiroki TAMURA, Eriko SATO and Tatsuro WAKIMOTO

*Japanese Journal of Multiphase Flow*, Vol. 29, pp. 451-459 (2016) (in Japanese)

Recently it is strongly demanded to manipulate a liquid droplet in lab-on-chip or micro reactors used in chemical engineering devices. This study concerns the control of the movement of liquid droplet on an inclined plate, using the difference of wettability caused by the chemical structure change of a polymer which is resulted from the irradiation of ultraviolet rays. The behavior of droplets was carefully observed experimentally when it enters into the irradiated area having an oblique boundary to the moving direction. Considering the surface tension acting on the perimeter with different contact angles, the movement of droplet was analyzed theoretically. The calculated results approximate well the actual behavior of droplet. Then we proposed a geometric pattern of irradiated area in which the droplet could be moved linearly with a constant angle to the gravitational direction. The experimental observation shows that the droplet behavior was successfully controlled to be moved along on the line of geometric pattern.

### **Synthesis and Functionalities of Acrylic Mutli-functional Hyperbranched Polymers**

Eriko SATO

*Convertech*, Vol. 506, pp. 119-122 (2015) (in Japanese)

### **Design of Dismantlable Adhesives Using Photoacid Generator**

Eriko SATO and Akikazu MATSUMOTO

*Material Stage*, Vol. 15, pp. 51-58 (2015) (in Japanese)

### **Design of Reactive Acrylic Polymers and Their Application to Pressure-sensitive Type Dismantlable Adhesives**

Eriko SATO and Akikazu MATSUMOTO

*Kobunshi*, Vol. 65, pp. 573-574 (2016) (in Japanese)

Dismantlable adhesives are required strong bonding with durability in use and easy debonding on demand. In order to satisfy the contradicting properties, we designed reactive acrylic copolymers and investigated their application to pressure-sensitive type dismantlable adhesives, in terms of the reduction in peel strengths, the achievement of interfacial failures, and quick dismantling. Reactive acrylic copolymers containing gas generating units and cross-linkable units resulted in significant reduction in the peel strength in response to heating in the presence of acid catalysts due to a decrease in the effective bonding area and an excess increase in modulus. Different failure modes were observed by changing morphology and the balance between gas generation and cross-linking. Acrylic copolymers containing hemiacetal esters achieved spontaneous debonding with both interfacial failures between adhesive layer, a metal adherend, and a support polymer film by simply soaking in boiling water. Precise polymer synthesis and the reaction control are shown to be effective for the design of high performance dismantlable adhesive materials.

### **Design and Precise Synthesis of Reactive Polymers and Their Application to Functional Adhesive Materials**

Eriko SATO

*2016 Japan-USA Seminar on Polymer Synthesis: -Polymer Synthesis for a Sustainable Future-*, Invited Lecture, Hokkaido, Japan, June 28, 2016, Abstract Book, p. 63

### **Thermo- and Light-Responsive Monofunctional Polymers**

Eriko SATO

### **Quantitative Evaluation of Photoinduced Bending Speed of Diarylethene Crystals**

Daichi KITAGAWA, Chika IWAIHARA, Hiroyasu NISHI and Seiya KOBATAKE

*Crystals*, Vol. 5, pp. 551-561 (2015)

Photoinduced crystal bending behavior of various photochromic diarylethenes was investigated. In all the diarylethene derivatives used in this work, the relationship between the initial photoinduced bending speed and the crystal thickness was well explained by the easy-handled Timoshenko's bimetal model. Moreover, a quantitative analysis method was proposed to reveal the relationship between the bending speed and the molecular structure of diarylethenes. These results provide the quantitative evaluation method of the photoinduced crystal bending speed.

### **Solvent Polarity Dependence of Photochromic Reactions of a Diarylethene Derivative as Revealed by Steady-State and Transient Spectroscopies**

Yukihide ISHIBASHI, Toshiyuki UMESATO, Mika FUJIWARA, Kanako UNE, Yusuke YONEDA, Hikaru SOTOME, Tetsuo KATAYAMA, Seiya KOBATAKE, Tsuyoshi ASAHI, Masahiro IRIE and Hiroshi MIYASAKA

*J. Phys. Chem. C*, Vol. 120, pp. 1170-1177 (2016)

Solvent polarity dependence of photochromic reactions such as cyclization and cycloreversion of a photochromic diarylethene derivative, 1,2-bis(2-methyl-1-benzothiophen-3-yl)perfluorocyclopentene, was investigated by steady-state spectroscopic and femtosecond laser photolysis methods. For the cyclization reaction, it was revealed that the quantum yield decreased with an increase in solvent polarities, mainly due to the decrease in the fraction of the conformer with  $C_2$  symmetry favorable for the cyclization. This result indicated that the branching ratio for the cyclization and the deactivation to the open-ring isomer at the conical intersection was almost independent of the solvent polarity. On the other hand, it was found for the cycloreversion process that the closed-ring isomer in the S1 state rapidly deactivated into the ground state in competition with the activated process leading to the conical intersection providing a pathway toward both open- and closed-ring minima in the ground state. The cycloreversion quantum yield also decreasing with an increase in the solvent polarity was attributed to larger increase of the direct deactivation into the ground state from the excited state minimum of the closed-ring isomer.

### **Photochromic Reaction Behavior and Thermal Stability of Thiophene-*S,S*-Dioxidized Diarylethenes Having a Benzofuryl Group**

Koki TANAKA, Daichi KITAGAWA and Seiya KOBATAKE

*Tetrahedron*, Vol. 72, pp. 2364-2368 (2016)

Diarylethenes having a benzofuryl group and their thiophene-*S,S*-dioxidized diarylethenes were synthesized and their optical properties and thermal stability were investigated. Upon oxidation of the thiophene ring, the optical properties such as absorption maxima, photocycloreversion quantum yields, and conversion from the open-ring isomer to the closed-ring isomer have changed. On the other hand, the thermal stability of the closed-ring isomers of the *S,S*-dioxidized diarylethenes is significantly higher than those of thiophene-*S,S*-dioxidized diarylethenes having a phenylthienyl group instead of a benzofuryl group. The high thermal stability of the closed-ring isomer was quantitatively discussed based on ground state energies obtained by quantum chemical calculations.

### **Photoinduced Stepwise Bending Behavior of Photochromic Diarylethene Crystals**

Daichi KITAGAWA, Rika TANAKA and Seiya KOBATAKE

*CrystEngComm*, Vol. 18, pp. 7236-7240 (2016).

It was found that crystals of 1,2-bis(2-methyl-5-(4-(*p*-toluylloxymethyl)phenyl)-3-thienyl)perfluorocyclopentene to exhibit photoinduced stepwise bending behavior. The bending rate significantly changed during continuous irradiation with ultraviolet (UV) light. This is a new type of photomechanical motion reported previously for various photoresponsive molecular crystals. Furthermore, the delayed bending behavior was observed even after UV light was turned off. The mechanism for the stepwise bending is discussed.

### **Strategy for Molecular Design of Photochromic Diarylethenes Having Thermal Functionality**

Daichi KITAGAWA and Seiya KOBATAKE

*Chem. Rec.*, Vol. 16, pp. 2005-2015 (2016)

Thermal reactivities of photochromic diarylethene closed-ring isomers can be controlled by introduction of substituents at the reactive positions. Diarylethenes having bulky alkyl groups undergo thermal cycloreversion reactions. When bulky alkoxy groups are introduced, diarylethenes have both thermal cycloreversion reactivities and low photocycloreversion quantum yields. Such photochromic compounds can be applied to thermally reusable photoresponsive-image recordings. The thermal cycloreversion reactivity of the closed-ring isomers can be evaluated using specific steric substituent constants and be correlated with the parameters. By introduction of trimethylsilyl or methoxymethyl groups at the reactive positions, the diarylethene closed-ring isomers undergo thermal irreversible reactions to produce byproducts at high temperature. These diarylethenes may be useful for secret image recordings. Furthermore, thiophene-*S,S*-dioxidized diarylethenes having secondary alkyl groups at the reactive positions undergo thermal byproduct formation reactions in addition to the photostability of the colored closed-ring isomers. Such materials may be used for light-starting thermosensors. The thermal byproduct formation reactivity can be evaluated by the specific substituent constants and theoretical calculations of quantum chemistry. These results supply the strategy for the molecular design of the photochromic diarylethenes having thermal functionality.

### **Photoinduced Rapid and Explosive Fragmentation of Diarylethene Crystals Having Urethane Bonding**

Daichi KITAGAWA, Tomohiro OKUYAMA, Rika TANAKA and Seiya KOBATAKE

*Chem. Mater.*, Vol. 28, 4889-4892 (2016)

Crystals of diarylethenes having urethane bonding exhibited photoinduced rapid and explosive fragmentation according to the photochromic reaction. The speed of the photogenerated crystal fragments was as fast as a few meters per second. The kinetic energy was independent of size, thickness, and volume of crystals, and depended on the crystal characters, such as crystal density and strength of intermolecular hydrogen bonding.

### **Optical Properties and Solvatochromism of Fluorene Derivatives Bearing *S,S*-Dioxidized Thiophene**

Tatsumoto NAKAHAMA, Daichi KITAGAWA, Hikaru SOTOME, Shoji ITO, Hiroshi MIYASAKA and Seiya KOBATAKE

*Photochem. Photobiol. Sci.*, in press (DOI: 10.1039/C6PP00126B)

We synthesized fluorene derivatives having phenylthiophene (FPT) or benzothiophene (FBT), and their *S,S*-dioxidized compounds (FPTO<sub>2</sub>, FPTO<sub>4</sub>, FBTO<sub>2</sub> and FBTO<sub>4</sub>), which are prepared by oxidation of the thiophene rings in FPT and FBT with *m*-chloroperoxybenzoic acid. FPT and FBT exhibited similar optical properties for absorption maximum wavelength, fluorescence maximum wavelength and fluorescence quantum yield. However, the absorption and fluorescence spectra of FPTO<sub>2</sub> were largely shifted toward longer wavelength in comparison with those of FPT, and their fluorescence quantum yields dramatically decreased with the oxidation. In contrast, the absorption and fluorescence spectra and the fluorescence quantum yield of FBTO<sub>2</sub> and FBTO<sub>4</sub> were similar to those of FBT. Moreover, FPTO<sub>2</sub> and FBTO<sub>2</sub> showed large solvatochromism. Such solvent dependent properties are ascribed to the charge-transfer character of the molecules.

### **Synthesis of Phenanthrene Derivatives and Photochromic Compounds by Photocyclization (Chapter 27.2.2)**

Seiya KOBATAKE

*Handbook of Experimental Methods in Organic Synthesis*, 2<sup>nd</sup> Ed., The Society of Synthetic Organic Chemistry, Japan, Maruzen Publishing Co. Ltd., pp. 976-980 (2015) (in Japanese)

Synthesis of phenanthrene derivatives and photochromic compounds by photocyclization has been summarized.

### **Applying Photoresponsive Photochromic Materials to Light-Starting Thermosensors**

Seiya KOBATAKE

*Convertech*, No. 12, pp. 82-85 (2015) (in Japanese)

The light-starting thermosensor that has an ultraviolet light triggered thermosensor function and detects temperature change by fading in color from a colored state has been introduced in Japanese.

### **Functionalization of Photochromic Molecular Materials (Chapter 3-7)**

Seiya KOBATAKE

*Frontier of Self-organized Materials*, T. Nakanishi *et al.* Eds., Frontier Publishing, pp. 180-187 (2015) (in Japanese)

Photochromism and photomechanical effect of organic molecular crystals have been introduced in Japanese.

### **Applying Photoresponsive Photochromic Materials to Light-Starting Thermosensors**

Seiya KOBATAKE

*Convertech & e-Print*, Vol. 6(2), pp. 57-61 (2016)

The light-starting thermosensor that has an ultraviolet light triggered thermosensor function and detects temperature change by fading in color from a colored state has been introduced in English.

### **Photochromic Bulk Materials**

Masakazu MORIMOTO, Seiya KOBATAKE, Masahiro IRIE, Hari Krishna BISOYI, Quan LI, Sheng WANG, and He TIAN

*Photochromic Materials: Preparation, Properties and Applications*, First Edition, Eds. by H. Tian, J. Zhang, Wiley-VCH Verlag, pp. 281-361 (2016).

Photochromic behavior of photochromic bulk materials including polymers and crystals has been introduced in English.

### **Photoinduced Bending Behavior of Gold-Coated Diarylethene Crystals**

Daichi KITAGAWA and Seiya KOBATAKE

World Engineering Conference and Convention 2015 (WECC2015), Poster Presentation, PS 6-6-5, Kyoto, Japan, November 29-December 2 (2015)

Photoinduced bending behavior of gold-coated diarylethene crystals has been presented in English. The gold-coated rod-like crystals show photoreversible bending upon alternating irradiation with ultraviolet (UV) and visible light. The initial speed of bending depends on the crystal thickness and the relationship between the speed and the thickness can be well explained by using Timoshenko's bimetal model for the non-coated diarylethene crystals. Moreover, the bending behavior of the gold-coated diarylethene crystals can also be explained by the extended bimetal model which we propose here. The gold-coated layer on the crystal cannot be broken during the photoreversible bending. Thus, the photoreversible bending behavior can be used as actual electrical circuit switching which is very small size. These results provide not only a new useful strategy to design for photomechanical actuators but also a new practical use of photomechanical crystals.

### **Photoactuator of Photochromic Diarylethene Crystals**

Seiya KOBATAKE and Daichi KITAGAWA

*World Engineering Conference and Convention 2015 (WECC2015)*, Poster Presentation, PS 6-6-6, Kyoto, Japan, November 29-December 2 (2015)

Photochromism of the diarylethene crystals and their photomechanical phenomena have been presented in English. Diarylethene derivatives are designed and synthesized for study on the photoinduced crystal shape changes. Upon irradiation with UV light to the diarylethene crystals, the molecules in the crystals underwent a photocyclization reaction that transforms the initial open-ring isomers into the photogenerated closed-ring isomers in the crystalline phase. The rod-like crystal of diarylethenes showed the crystal bending away from the incident UV light or toward the incident UV light, depending on the molecular structure or the crystal packing. The bent crystal returned to the initial straight crystal by irradiation with visible light. The bending speed depended on the crystal thickness and the curvature change against the crystal thickness was well fitted to Timoshenko's bimetal model. Furthermore, we have found that the bending behavior depends on the wavelength of the incident light. The behavior also depends on the thickness of the crystal. These materials can be potentially applied for novel organic solid devices, and it is possible not only to become a new organic device but also to open a new possibility as the crystal materials.

### **Silica Nanoparticles Covered with Diarylethene Polymers for Photochromic Pigment**

Katsuya SHIMIZU, Ryuta SENO, and Seiya KOBATAKE

*World Engineering Conference and Convention 2015 (WECC2015)*, Poster Presentation, PS 6-6-7, Kyoto, Japan, November 29-December 2 (2015)

Fabrication of silica nanoparticles covered with polystyrene having diarylethene chromophores on side chain has been presented in English. The silica nanoparticles were prepared by reversible addition-fragmentation chain transfer (RAFT) copolymerization of St and a diarylethene monomer using silica nanoparticle covered with a RAFT agent.

### **Photomechanical Actuators of Photochromic Diarylethene Crystals**

Seiya KOBATAKE and Daichi KITAGAWA

*Pacificchem 2015*, Oral Presentation, MTL1249, Honolulu, Hawaii, USA, December 15-20 (2015)

Photochromism of the diarylethene crystals and their photomechanical phenomena, such as crystal bending and crystal twisting have been presented in English. Diarylethene derivatives are designed and synthesized for study on the photoinduced crystal shape changes. Upon irradiation with UV light to the diarylethene crystals, the molecules in the crystals underwent a photocyclization reaction that transforms the initial open-ring isomers into the photogenerated closed-ring isomers in the crystalline phase. The rod-like crystal of diarylethenes showed the crystal bending away from the incident UV light or toward the incident UV light. The bending speed depended on the crystal thickness and the curvature change against the crystal thickness was well fitted to Timoshenko's bimetal model. Furthermore, we have found specific crystal ribbon deformation. This crystal reversibly changed from the straight thin crystal to the spiral twisting crystal. Such deformation depends on the crystal packing. These materials can be potentially applied for novel organic solid devices.

### **UV Light Irradiation Wavelength Dependence on the Photoinduced Bending Behavior of Photochromic Diarylethene Crystals**

Daichi KITAGAWA and Seiya KOBATAKE

*Pacificchem 2015*, Poster Presentation, MTL1509, Honolulu, Hawaii, USA, December 15-20 (2015)

In our previous work, it has been clarified that the depth of the photochromic reaction of diarylethenes from the crystal surface in the crystal plays very important role for the photoinduced bending. Control of the reaction depth by changing UV irradiation wavelength and the change in the photoinduced bending behavior have been presented in English. When irradiated with 365 nm light, the crystal of a diarylethene bends toward the incident light. However, when irradiated with 380 nm light, at first the crystal bends away from the light source and then bends toward the incident light. We proposed the comprehensive mechanism to explain the both bending behaviors.

### **Synthesis and Characterization of Amphiphilic Silica Nanoparticles Covered with Block Copolymers Branching Photochromic Diarylethene Moieties on Side Chain**

Katsuya SHIMIZU, Ryuta SENO, and Seiya KOBATAKE

*Pacificchem 2015*, Poster Presentation, MTL1512, Honolulu, Hawaii, USA, December 15-20 (2015)

Fabrication of silica nanoparticles covered with polystyrene having photochromic diarylethene chromophores on side chain has been presented in English. The silica nanoparticles were prepared by reversible addition-fragmentation chain transfer (RAFT) copolymerization of styrene and diarylethene monomer using silica nanoparticle covered with a RAFT agent.

### **Reversible Photoinduced Linear Birefringence Change of Diarylethene Single Crystals**

Hajime TSUJIOKA and Seiya KOBATAKE

*Pacificchem 2015*, Poster Presentation, MTL1528, Honolulu, Hawaii, USA, December 15-20 (2015)

Photoinduced linear optical birefringence change in the single crystal of a diarylethene has been presented in English. When the crystal was irradiated with ultraviolet light UV, the interference spectrum was shifted. The changed birefringence returned to the initial state by irradiation with visible light. The change of the birefringence induced by UV irradiation depended on the crystal faces. The face dependence of the birefringence change is considered to be due to the difference in the magnitude of the molecular polarizability anisotropy viewed from the crystal faces.

### **Synthesis and Optical Properties of Fluorene Derivatives Bearing S,S-Dioxidized Thiophene**

Tatsumoto NAKAHAMA and Seiya KOBATAKE

*Pacificchem 2015*, Poster Presentation, MTL5 1565, Honolulu, Hawaii, USA, December 15-20 (2015)

The optical properties of fluorene derivatives introducing S,S-dioxidized thiophene moiety (FPTO<sub>2</sub>, FPTO<sub>4</sub>, FBTO<sub>2</sub>, and FBTO<sub>4</sub>) have been presented in English. FPTO<sub>2</sub> showed large solvatochromism. Such solvent dependent properties are ascribed to the charge transfer character of the molecule.

### **Development of Novel Photomechanical Phenomena of Photoresponsive Molecular Crystals by High-order Photoexcitation**

Seiya KOBATAKE

*The 96th CSJ Annual Meeting*, Invited Lecture, 4S6-09, Kyotanabe Campus, Doshisha University, Kyoto, Japan, March 24-27 (2016) (in Japanese)

Novel photomechanical phenomena of photochromic diarylethene crystals have been presented in Japanese.

### **Light-Driven Actuators of Photochromic Diarylethene Crystals**

Daichi KITAGAWA and Seiya KOBATAKE

*XXVIth IUPAC Symposium on Photochemistry (2016 IUPAC Photochem)*, Oral Presentation, 2EY09, Osaka City Central Public Hall, Osaka, Japan, April 3-8 (2016)

Photochromism of the diarylethene crystals and their photomechanical phenomena have been presented in English.

### **Development of Novel Photomechanical Phenomena of Photoresponsive Molecular Crystals by High-order Photoexcitation**

Seiya Kobatake

*1st International Symposium on Photosynergetics*, Oral Presentation, O14, Sigma Hall, Osaka University, Osaka, Japan, June 2-4 (2016)

Novel photomechanical phenomena of photochromic diarylethene crystals have been presented in English.

**Generation and Characterization of Rat Monoclonal Antibodies against Epidermal Growth Factor Receptor**

Tomohiro OSAKI, Cai-Xia WANG, Taro TACHIBANA, Masayuki AZUMA, Masaya KITAMURA and Takeshi NAKANISHI

*Monoclon. Antib. Immunodiagn. Immunother.*, Vol. 34, pp. 418–422 (2015)

Overexpression of the epidermal growth factor receptor (EGFR) gene and dysregulation of EGFR signaling are observed in various cancer cells, and EGFR is a validated target for cancer therapy. In the present study, we report on the generation of two rat anti-EGFR antibodies (clones 2C2D3 and 4H7F4) by using the rat lymph node method. Flow cytometric analysis and immunofluorescence showed that both antibodies specifically bound to EGFR on the surface of cancer cells. Competitive analysis demonstrated that the epitope of each antibody had no overlap with that of the therapeutic anti-EGFR antibody cetuximab. These results suggest that 2C2D3 and 4H7F4 are potentially useful in EGFR-targeted cancer therapy.

**Photoinduced Electron Transfer from Aromatic Amino Acids to the Excited Isoalloxazine in Flavin Mononucleotide Binding Protein. Is the Rate in the Inverted Region of Donor–Acceptor Distance Not Real?**

Nadtanet NUNTHABOOT, Kiattisak LUGSANANGARM, Arthit NUEANGAUDOM, Somsak PIANWANIT, Sirirat KOKPOL, Fumio TANAKA, Seiji TANIGUCHI, Haik CHOSROWJAN, Takeshi NAKANISHI and Masaya KITAMURA

*J. Photochem. Photobiol. A: Chem.*, Vol. 326, pp. 60–68 (2016)

Mechanisms of photoinduced electron transfer (ET) from tryptophanes 32 and 106 in subunits A and B (Trp32A, Trp32B, Trp106A and Trp106B) of wild type flavin mononucleotide binding protein (FBP) dimer were studied through relations of the logarithmic ET rate ( $\ln$  Rate) vs the donor-acceptor distance ( $R_c$ ). The sum ( $GT$ ) of standard free energy gap (SFEG) between the products and reactants, electrostatic energy (ESDA) between the photo-products and solvation reorganization energy (SROE) and electrostatic energy (NetES) between the photo-products and ionic groups inside the protein were numerically determined for the all donors with atomic coordinates obtained by molecular dynamic simulation. The  $GT$  values of Trp32A and Trp32B displayed always negative in the entire  $R_c$  range, which predicts that ET rate becomes slower as the  $R_c$  shorter. The reason of negative  $GT$  values in Trp32A and Trp32B were numerically elucidated with the mean values of SFEG, ESDA, SROE, and NetES.

**Conformational Difference between Two Subunits in Flavin Mononucleotide Binding Protein Dimers from *Desulfovibrio vulgaris* (MF): Molecular Dynamics Simulation**

Nadtanet NUNTHABOOT, Kiattisak LUGSANANGARM, Somsak PIANWANIT, Sirirat KOKPOL, Fumio TANAKA, Takeshi NAKANISHI and Masaya KITAMURA

*Comput. Biol. Chem.*, Vol. 64, pp. 113–125 (2016)

The structural and dynamical properties of five FMN binding protein (FBP) dimers, WT (wild type), E13 K (Glu13 replaced by Lys), E13 R (Glu13 replaced by Arg), E13 T (Glu13 replaced by Thr) and E13Q (Glu13 replaced by Gln), were investigated using a method of molecular dynamics simulation (MDS). In crystal structures, subunit A (Sub A) and subunit B (Sub B) were almost completely equivalent in all of the five FBP dimers. However, the predicted MDS structures of the two subunits were not equivalent in solution, revealed by the distances and inter-planar angles between isoalloxazine (Iso) and aromatic amino acids (Trp32, Tyr35 and Trp106) as well as the hydrogen bonding pairs between Iso and nearby amino acids. Residue root of mean square fluctuations (RMSF) also displayed considerable differences between Sub A and Sub B and in the five FBP dimers. The dynamics of the whole protein structures were examined with the distance (RNN) between the peptide N atom of the N terminal (Met1) and the peptide N atom of the C terminal (Leu122). Water molecules were rarely accessible to Iso in all FBP dimers which are in contrast with other flavoenzymes.

**Development of UV Light Irradiation Patterning of Bacteriorhodopsin Thin Films for Biomimetic Functional Devices**

Yoshihiro HARUYAMA, Katsuyuki KASAI, Toshiki YAMADA, Shukichi TANAKA, Yukihiro TOMINARI,

Takahiro KAJI, Masaya KITAMURA and Akira OTOMO

*J. Nanosci. Nanotechnol.* Vol.16, pp. 3420–3425 (2016)

We developed a new patterning method for bacteriorhodopsin (bR) thin films using UV light irradiation. The proton pump function of bR thin films can be deactivated with UV light irradiation. Inactivation of the proton pump function of bR is related to structural changes or photo-bleaching of the retinal in bR using UV light exposure, which was confirmed with absorption and Raman spectroscopy measurements. Utilizing inactivation of the proton pump function with UV light irradiation, we prepared a bR photocell with a stripe-patterned bR thin film and measured its photocurrent response. The new patterning method is applicable to complicated patterning and patterning with a higher spatial resolution, which extends the application of bR thin films as sensor devices.

### **Improved Isolation Products for Shikonin from the Root of the Chinese Medicinal Plant *Lithospermum erythrorhizon* and its Solubilization with Cyclodextrins**

Hideki AZUMA, Jiawei LI, Ryota YOUTA, Toshio SUZUKI, Kazuhide MIYAMOTO, Taizo TANIGUCHI and Takeshi NAGASAKI

*J. Appl. Med. Arom. Plant.*, Vol. 3(2), pp. 58-63 (2016).

In this study, we improved the method for the isolation and purification of the bioactive compound shikonin from the dried root of the traditional Chinese medicinal plant *Lithospermum erythrorhizon* without a tedious chromatographic separation. Furthermore, we also attempted the solubilization of shikonin in water with cyclodextrins (CDs) using a solid phase “high-speed vibration milling”. Among the various CDs, sulfobutylether- $\beta$ -CD (SBE $\beta$ -CD) showed a highest solubilizing ability and 52.5% of shikonin was solubilized with equimolar amount of SBE $\beta$ -CD. In addition, the SBE $\beta$ -CD-shikonin complex showed higher apoptogenic activity than that of the same concentration of free shikonin against murine primary peritoneal macrophages. These results indicate that SBE $\beta$ -CD is a suitable excipient for clinical application of shikonin.

### **Lipid-Membrane-Incorporated Arylboronate Esters as Agents for Boron Neutron Capture Therapy: Third Method for Preparation of High Boron Content Liposomes**

Masafumi UEDA, Kengo ASHIZAWA, Kouta SUGIKAWA, Kazuya KOUMOTO, Takeshi NAGASAKI and Atsushi IKEDA

*Org. Biomol. Chem.* in press

Arylboronate esters with methyl groups in both *ortho* positions could be stably incorporated in the lipid membranes with a high concentration without hydrolysis. This method could increase the maximum ratio of boron atoms in liposomal boron carriers by the combination of previous methods; (A) water-soluble boron compounds introduced in internal water phase, (B) lipophilic boron compounds embedded in a liposome bilayer.

### **Water Soluble Complex of Kojic Acid Modified *o*-Carborane with Hydroxypropyl- $\beta$ -Cyclodextrin for Melanoma-Targeting Boron Neutron Capture Therapy**

Takeshi NAGASAKI, Riku KAWASAKI, Junki Kawaguchi and Mitsunori KIRIHATA

*The 4<sup>th</sup> Asian Chemical Biology Conference*, Invited Lecture, KaoHsiung, Taiwan, November 28-December 1, 2016; Preprints.

### **Changes in Cell Adhesiveness and Physicochemical Properties of Cross-Linked Albumin Films after Ultraviolet Irradiation**

Hironori YAMAZOE, Hisashi NAKANISHI, Yukiyasu KASHIWAGI, Masami NAKAMOTO, Akira TACHIBANA, Yoshihisa HAGIHARA and Toshizumi TANABE

*Langmuir*, Vol. 32, pp. 203-210. (2016)

We discovered the unique cell adhesive properties of ultraviolet (UV)-irradiated albumin films. Albumin films prepared using a cross-linking reagent with epoxy groups maintained native albumin properties, such as resistance to cell adhesion. Interestingly, the cell adhesive properties of films varied depending upon the UV irradiation time; specifically, cell adhesiveness increased until 2 h of UV irradiation, when the cell number attached to the film was similar to that of culture dishes, and then cell adhesiveness decreased until 20 h of UV irradiation, after which the surface returned to the initial nonadhesive state. To elucidate the molecular mechanisms underlying this phenomenon, we examined the effect of UV irradiation on albumin

film properties. The following changes occurred in response to UV irradiation: decreased  $\alpha$ -helical structure, cleavage of albumin peptide bonds, and increased hydrophilicity and oxygen content of the albumin film surface. In addition, we found a positive correlation between the degree of cell adhesion and the amount of fibronectin adsorbed on the film. Taken together, UV-induced changes in films highly affect the amount of cell adhesion proteins adsorbed on the films depending upon the irradiation time, which determines cell adhesion behavior.

#### **Acquisition of Cell-Adhesion Capability of the Surface of Crosslinked Albumin Films Irradiated with Atmospheric-Pressure Plasma Jets**

Tatsuru SHIRAFUJI, Mami IWAMURA, Ryosuke TAGA, Yukiyasu KASHIWAGI, Kota NAKAJIMA, Yuji OGATA, Kenji TANAKA, Akira TACHIBANA and Toshizumi TANABE

*Jpn. J. Appl. Phys.* Vol. 55(7S2), 07LG03 (2016)

Crosslinked albumin films, to which L929 cells do not attach by nature, acquire the L929-cell-adhesion capability by irradiation of an atmospheric pressure plasma jet (APPJ) of He gas. The number of attached cells was  $2.6 \times 10^4$  cells/cm<sup>2</sup> after the APPJ irradiation for 180 s, while conventional UV photolithography, which was performed in our previous work, required 2 h to obtain the same order of magnitude of the number of attached cells. The contact angle of samples decreased steeply from 105 to 38° in the first 10 s irradiation, but decreased quite gradually from 38 to 32° with increasing irradiation time from 10 to 180 s. In contrast to the nonlinear variation in the contact angles, the number of attached cells almost linearly increased from  $4.5 \times 10^3$  to  $2.6 \times 10^4$  cells/cm<sup>2</sup> with increasing treatment time. X-ray photoelectron spectroscopy of the samples indicated that hydrophilic functional groups of C–C=O gradually formed with increasing APPJ irradiation time up to 180 s. These results suggest that the cell adhesion capability of the crosslinked albumin films is not simply explained by the decrease in contact angle but also by the formation of oxidized functional groups on the surface. The effects of UV and vacuum UV light from APPJ were negligible, which indicates that the formation of oxidized functional groups on the surface is not caused by photon-assisted surface reactions but by reactions involving chemically active species supplied from APPJ

#### **Identification and Characterization of d-Succinylase, and a Proposed Enzymatic Method for d-Amino Acid Synthesis**

Yosuke SUMIDA, Sachio IWAI, Yoshiaki NISHIYA Shinya KUMAGAI, Toshihide YAMADA and Masayuki AZUMA

*Adv. Synth. Catal.* Vol.358, pp.2041–2046 (2016)

Chiral amino acids are important intermediates for the pharmaceutical industry. We have developed a novel one-pot enzymatic method for amino acid synthesis by the dynamic kinetic resolution of N-succinyl-dl-amino acids using d-succinylase (DSA) and N-succinylamino acid racemes (NSAR, EC 4.2.1.113). The DSA from *Cupriavidus* sp. P4-10-C, which hydrolyzes N-succinyl-d-amino acids enantioselectively to their corresponding amino acids, was identified for the first time by screening soil microorganisms. Subsequently, the DSA gene was cloned and overexpressed in *Escherichia coli*. DSA was shown to comprise two subunits with molecular masses of 26 kDa and 60 kDa. Additionally, the NSAR gene from *Geobacillus stearothermophilus* NCA1503, which racemizes N-succinylamino acids, was also cloned and overexpressed in *E. coli*. The highly purified DSA and NSAR prepared from each recombinant *E. coli* were characterized and used for d-amino acid synthesis. An one-pot enzymatic method converted 100 mM N-succinyl-dl-phenylalanine to d-phenylalanine in 91.1% conversion with 86.7% ee. This novel enzymatic method may be useful for the industrial production of many d-amino acids.

#### **Chromatin-Prebound Crm1 Recruits Nup98-HoxA9 Fusion to Induce Aberrant Expression of Hox Cluster Genes**

Masahiro OKA, Sonoko MURA, Kohji YAMADA, Percival SANGEL, Saki HIRATA, Kazumitsu MAEHARA, Koichi KAWAKAMI, Taro TACHIBANA, Yasuyuki OHKAWA, Hiroshi KIMURA and Yoshihiro YONEDA.

*Elife.* 5. pii: e09540. doi: 10.7554/eLife.09540. (2016)

The nucleoporin Nup98 is frequently rearranged to form leukemogenic Nup98-fusion proteins with various partners. However, their function remains largely elusive. Here, we show that Nup98-HoxA9, a fusion between Nup98 and the homeobox transcription factor HoxA9, forms nuclear aggregates that

frequently associate with facultative heterochromatin. We demonstrate that stable expression of Nup98-HoxA9 in mouse embryonic stem cells selectively induces the expression of Hox cluster genes. Genome-wide binding site analysis revealed that Nup98-HoxA9 is preferentially targeted and accumulated at Hox cluster regions where the export factor Crm1 is originally prebound. In addition, leptomycin B, an inhibitor of Crm1, disassembled nuclear Nup98-HoxA9 dots, resulting in the loss of chromatin binding of Nup98-HoxA9 and Nup98-HoxA9-mediated activation of Hox genes. Collectively, our results indicate that highly selective targeting of Nup98-fusion proteins to Hox cluster regions via prebound Crm1 induces the formation of higher order chromatin structures that causes aberrant Hox gene regulation.

#### **Generation of Rat Monoclonal Antibodies Against Human Pancreatic Ductal Adenocarcinoma Cells**

Kiyoshi HIGASHI, Nobuyuki FUJII, Masahiko KUSHIDA, Keita YAMADA, Noriyuki SUZUKI, Koichi SAITO K and Taro TACHIBANA.

*Monoclon. Antib. Immunodiagn. Immunother.*, Vo. 35, pp. 148-154 (2016)

Pancreatic ductal adenocarcinoma is an aggressive tumor with a poor prognosis. Biomarkers that can detect the tumor in its early stages when it may be amenable to curative resection might improve prognosis. To discover novel markers expressed in primary pancreatic cancer, we generated a panel of monoclonal antibodies against pancreatic ductal adenocarcinoma cell line BxPC3 using a rat medial iliac lymph node method. The antigen recognized by 1B5A5 was expressed on the cell surface and secreted into the conditioned medium of BxPC3 cells, and characterized as glycoproteins with molecular mass between 60 and 90 kDa. A wide range of molecular weights of 1B5A5 antigen in several pancreatic cancer cell lines were observed. Immunohistochemistry using a human multiple organ tumor tissue array showed an enhanced expression of 1B5A5 antigen in pancreas, lung, stomach, breast, urinary bladder, colon, and cervix uteri cancers. Immunoprecipitation followed by proteomic analyses identified CEACAM6 as a 1B5A5 antigen. In addition, western blot analysis results indicated that the 1B5A5 epitope is located within an amino-terminal domain of CEACAM6. These results raised the possibility that our approach could lead to discovery of novel biomarkers for the early stage of cancers in a relatively short period of time.

*Architecture and Building Engineering*

**Comparison Study of Elasto Plastic Behavior on Static and Dynamic Responses for Plane Lattice Structures**

Yoshiya TANIGUCHI and Kenta TOKUDA

*J. Struct. Constr. Eng., AIJ, Vol. 81 No. 723, 859-869, May, 2016*

DOI <http://doi.org/10.3130/aijs.81.859>

This paper focuses on the elasto - plastic behavior on static responses and dynamic responses for plane lattice structures, which are considered as a beam type structure. The purpose is to make clear the relationship between seismic responses and static responses such as static absorbed energy properties after and before yielding, and to estimate allowable seismic levels with the information of static elasto - plastic behaviors. In comparing the two responses for 4 plane lattice structures, the following conclusions are obtained in the present study. (1) The relationships between the static absorbed energy and displacements are not affected by the loading shape. It may be able to estimate the response of structures with an index of potential energy. (2) The fact is confirmed that the allowable maximum earthquake input accelerations are affected with the self-weight under vertical oscillations more than horizontal oscillations. (3) In comparing the dynamic property  $q$  and the static property  $j$ , the dash and dotted line in Fig.28 could be presented to estimate the allowable maximum earthquake acceleration with the static elasto plastic behaviors for beam type structures.

**Impact Testing of an Arch Model Using Tuned Mass Dampers with Initial Displacement**

Susumu YOSHINAKA, Yoshiya TANIGUCHI and Makoto YAMAKAWA (Tokyo Denki University)

*Journal of Structural and Construction Engineering (Transactions of AIJ), AIJ, No. 722, pp. 735-745, (2016) (in Japanese)*

We propose TMDs (Tuned mass dampers) with initial displacement that are possible to control initial transient responses effectively. In our previous study, we proposed the optimal design formulas of TMDs with initial displacement to control impulse responses focusing on modal damping ratios of two vibration modes and formulated the initial conditions of TMD displacement release. In this paper, we describe the vibration test using an arch model under impulse loading to verify the control performance of the proposed method experimentally. Then, we study the influence of different conditions about the length and the release time of TMD initial displacement on the control performance analytically.

**Formulation of release conditions for TMDs with initial displacement and its application to an arch model**

Susumu YOSHINAKA, Riki YOSHIDA (West Japan Railway Company) and Yoshiya TANIGUCHI

*Proceedings of the IASS Annual Symposium 2016, "Spatial Structures in the 21st Century", 26-30 September, 2016, Tokyo, Japan, CS1F-1, ID 1024, pp.1-10, (2016)*

TMDs show high control performance for harmonic responses, but have limited capacity under transient responses. To control transient responses effectively, we propose a TMD with initial displacement. In our previous study, we proposed design formulas for impulse loading. These formulas are based on the principle that under restricted structural initial conditions giving a specific TMD initial displacement, the first modal response is eliminated while the the second modal response with high modal damping is only oscillated. In this paper, we formulate an equation for initial conditions to release initial TMD displacement, and show that by dividing one TMD into multiple TMDs with different natural frequencies, the restricted initial conditions to release a TMD can be altered. Then, to confirm the applicability of the proposed method to spatial structures, we study the control effect of TMDs with initial displacement attached to an arch model.

**Actual situation of ventilation design and evaluation using contamination area ratio of smoking rooms**

Noriko Umemiya, Satoshi Hirata, Ayako Fujita and Tomohiro Kobayashi

*Proceedings of the 14th International Building Performance and Simulation Association Conference, pp. 1663-1668 (2015).*

Contamination distributions were calculated and evaluated by contamination area ratio at respiration height for actual smoking rooms. As a result, 1) Dust contamination area ratio is about 20 % for required ventilation volume by Guidelines. 2) Ventilation volume based on smell level 1 is almost as much as that based on dust criterion. 3) Contamination area ratio of smell level is more rapidly reduced than that of dust as ventilation volume is increased. 4) A desirable clean air condition is producible by increasing ventilation volume on the basis of smell level 1, but strong air current is locally created.

**Questionnaire survey of air-conditioner effects on sleep quality in summer -Analyses of falling asleep, maintaining sleep factor and fatigue recovery factor**

Nakayama Yusuke, Umemiya Noriko, Sakane Tatsuya, Arai Jun-ichiro (Daikin Industries, Ltd.), Kobayashi Tomohiro and TACHIBANA Yoshiki

*Proceedings of the 6th International Building Physics Conference*, No.862, pp.1-6 (2015).

A questionnaire survey was administered to assess air-conditioner use effects on the relation between residential thermal performance and sleep quality. Results showed the following. 1-1) The Factor 2 (Falling Asleep, Maintaining Sleep) score is unrelated to ‘residential heating performance’ or ‘residential cooling performance’. Some items included in Factor 2, however, are more highly related to performance for an air-conditioner non-user group (AC-NU) than for a user group (AC-U). 1-2) The Factor 2 score is unrelated to ‘solar heat from windows’ for AC-U. However, the score is lower and ‘solar heat from windows’ is higher for AC-NU. 2-1) The Factor 4 (Fatigue Recovery) scores by ‘residential heating performance’ and ‘residential cooling performance’ are higher for AC-U. 2-2) The Factor 4 score is unrelated to ‘solar heat from windows’.

**Lighting use and evaluation in apartment family rooms with various lamp types and colors**

Noriko Umemiya, Yuya Kobayashi and Tomohiro Kobayashi

*Proceedings of the 8th conference of CJK*, pp.78-81 (2015).

A survey of the actual state of possession, setting, use, and evaluation of lamps in family rooms was conducted for 458 apartments in 111 buildings during 2012 and 2013 in Osaka, Japan. Evaluation included items of light environment evaluation of family rooms: brightness, glare, preference, comfort and performance and colours of light, and so on. Impressions of the room were reported by 18 scales comprising three factors of comfort, luxury, and simplicity. Light environment evaluations other than preferences did not differ among those of incandescent, fluorescent, and LED lamps. However, incandescent lamps were more preferred in light environment evaluations. Rooms with incandescent lamps were regarded as more ‘comfortable’, ‘fashionable’, ‘warm’, and ‘active’ than those without incandescent lamps. No difference was found in either light environment evaluation or impression evaluation between rooms with only ‘yellow’ LED lamps and those with only incandescent lamps.

**Estimation of natural ventilation flow rate for a pitched-roof detached house provided with monitor roof**

Tomohiro Kobayashi, Tomoyuki Chikamoto (Ritsumeikan Univ.), Noriko Umemiya and Keishi Osada (R.I.A.)

*Journal of Environmental Engineering (Transactions of AIJ)*, Vol.81, No.719, pp.83-91 (2016) (in Japanese).

Monitor roofs can promote natural ventilation, but it is not easy to predict ventilation flow rate through a monitor roof because of its variable resistance depending upon a number of factors such as wind velocity, wind direction. To predict flow rate through monitor roof, its ventilation characteristic must be arranged in advance, which is expressed as a correlation between internal pressure and flow rate; i.e. p-Q curve. By using dimensionless ventilation characteristics obtained in the previous work, this paper focuses on the flow rate of realistic residential building under various meteorological conditions, which has almost never been evaluated before. This paper presents wind tunnel measurement to obtain  $C_p$  value, and calculation of annual ventilation flow rate based on simplified estimation method using ventilation characteristics. Assuming several cases of ventilation path aiming for ventilation or cross-ventilation, ventilation performance is evaluated.

## ***Urban Design and Engineering***

### **An Empirical Study on Verbal Sketch for Visually-impaired People Navigation**

Mei TAKAHASHI, Takashi UCHIDA, and Keisuke MATSUURA

*Japan Society of Traffic Engineers, Papers on Traffic Engineering, No. 35, pp. 465-470 (2015) (in Japanese)*

### **An Empirical Study on Verbal Map Guidelines for Visually-impaired People Navigation considering Daily Mobility Needs**

Mei TAKAHASHI and Takashi UCHIDA

*Japan Society of Civil Engineers, Proceedings of Infrastructure Planning, No.52, pp. 1481-1488 (2015) (in Japanese)*

Unlike sighted people, visually-impaired people cannot use a high performance pedestrian navigation system. The purpose of this study is to revise verbal map guidelines that show rules for describing features in a town to enhance everyday mobility. Therefore, this study figures out feature information visually-impaired people use in everyday life.

This study presents a review of earlier studies and related studies, and make a speech augmented reality (AR) application. Then, two kinds of field experiments are conducted. The first experiment is a monitor experiment and has visually-impaired people use a smartphone which implemented a speech AR application in everyday life. The second experiment is a site experiment and has them use a pedestrian navigation system and walk in a course we set according to it. Finally, from the hearing result of those experiments, verbal map guidelines are revised.

### **Study on the Effect that the Relationship and Evaluation for the Community Bus Gives Support Awareness to Business**

Yusuke KURASHIMA and Takashi UCHIDA

*Japan Society of Civil Engineers, Proceedings of Infrastructure Planning, No.52, pp. 1135-1143 (2015) (in Japanese)*

For the purpose of the acquisition of the new user and the increase in user, various use promotion measures are carried out by the community bus. Today, the measure for the purpose of bringing up attachment and support awareness for the bus is worked on. In such situation, it is that following two are important. First, evaluate a measure transversely and clarify the difference of the evaluation. Next, clearly about the relationship with the actual situation of the use and the evaluation and the attachment and support awareness to a bus.

In this study, we took up community bus "Taco-bass" of Akashi-shi, Hyogo as an example. We clarified the influence that the relation with the community bus such as the evaluation for various use promotion measures or the use of the bus, or the situation of the movement limitation, gave to support awareness, and showed consideration for the breeding of the support awareness.

### **Causal Analyses of Attitudes of Residents along the Medium and Small Size River for the Posterior Evaluation of the Nature-Friendly Environment and the Water Amenity**

Yasumasa FUKUSHIMA and Takashi UCHIDA

*Japan Society of Civil Engineers, Proceedings of Infrastructure Planning, No.52, pp.136-143 (2015) (in Japanese)*

In recent years the development of the urban river has been focusing on efforts for the environment and the water amenity besides the flood control and the water utilization. In the waterfront development the stakeholders/agents such as local governments, inhabitants, planners, and bodies concerned are mutually involved, in some cases however, the residents along the river have failed to value and then water amenity has made little progress.

This paper takes a case of the waterfront development of the small size river in an emerging built-up area. Going through several years after the project implementation, we take hold of the actual condition and the attitudes of residents by means of questionnaire survey to the inhabitants. This study performs respective analyses on the relationship between the factors towards the smooth implementation of the enterprise and the consensus formation and in urban riverside development considering development methods in order to promote the utilization with high evaluations from the inhabitants as concrete strategies.

### **Analysis of Resident Interest and Intentions for Community Bus Network Reorganization**

Yumie SAWADA and Takashi UCHIDA

*Osaka City University, Memoirs of the Faculty of Engineering, Vol. 56, pp. 37-50 (2015)*

Continuous reorganization of a community bus network to maintain the service is extremely important. This study specifically examines residents, who must play an important role in the reorganization of a community bus network, in terms of their interests and intentions for reorganization of community bus network. The target case is Akashi community bus "Taco Bus," which is well known by its PDCA cycle.

The questionnaire results of the reveal usage conditions and socioeconomic characteristics in addition to the state of their interests and intentions. Based on the data of the questionnaire, the interests and intentions are classified into five groups by principal component analysis and cluster analysis. To clarify the group characteristics, discriminant analysis was conducted. We discuss the problems of maintaining a bus network based on the group characteristics.

### **Major Issues of Bicycle Use in Urban Area from View Point of Community Development**

Yurie ISHIMURA, Yasuo HINO and Yuuka WATANABE

*Osaka City University, Memoirs of the Faculty of Engineering, Vol. 56, pp. 51-55(2015)*

The problems of illegally parked bicycles have been shifting in a central area from around rail station. In order to improve such problem, the activities based on public involvement must be necessary, because there are not only many small stores without parking facilities of bicycles, but also many stakeholders such as habitants and the store owners and the visitors, who have different interests. However, it is not always revealed the differences of interests for using bicycles among them. Then the aims of this study must be to investigate the consciousness of each stakeholder in the commercial area in Osaka city. As a result, it became clear that the illegal parked bicycles must be the common problem among of them, nevertheless the thinking of community development may be different. These interesting findings should be important information to realize the activity based on the public involvement.

### **A Case Study on Effect and Sustainability of Community Development based on Public Involvement in Wide Area**

Mizuho SHIMA and Yasuo HINO

*Japan Associate of Civil Engineers, Proceedings of Infrastructure Planning, No. 52, 4p (CD-ROM) (2015) (in Japanese)*

The community development based on public involvement in wide area must be supported by local government from viewpoint of public benefit. On the other hand, there may be some weak points in terms of sustainability. Especially, it must be important issues to not only keep the relationships of participants and areas, but also continue the organization for activities by its own resources.

In this paper, some interesting findings concerned with the effects and problems of community development in wide area came out of the questionnaire for the event promoters, the program planners and the participants. In addition, some proposals were referred to improve their problems.

### **Consciousness for Community Development and Bicycle Use in Commercial Zone of City Centre**

Yurie ISHIMURA, Yasuo HINO, Yuuka WATANABE and Yasutaka Kashimoto

*Japan Associate of Civil Engineers, Proceedings of Infrastructure Planning, No. 52, 4p (CD-ROM) (2015) (in Japanese)*

Illegal parked bicycle problem has moved to city centre from near rail station area. In these areas, there are many stakeholders such as residents, shop owners, employee and visitors. Therefore, it may be not easy to improve the illegal parking of bicycles.

In this paper, some interesting findings came out of the questionnaire survey, such as differences of image for desirable community development, common idea for bicycle use and the problem of illegal parked bicycles, are summarized. In addition, it was also clear that there must be the possibility of activity by public involvement. These results must be useful information to realize the workshop activities among residents, shop owners and visitors based on governmental support.

### **Evaluation of New Bus Services to Support Needs for Going-out of Elderly People from view point of Effects of Time Process**

Kumi OSANAGA, Yasuo HINO, Kazuya NIZUKAMI and Ryou TANAKA

*Japan Associate of Civil Engineers, Proceedings of Infrastructure Planning, No. 52, 4p (CD-ROM) (2015) (in Japanese)*

In the aging society, the vitality of region and/or city center must depend on the activities of elderly people. Therefore, it must be essential to keep and improve the public transport services to encourage and support the going-out of elderly people. Especially, it should be important to investigate the change of understanding, and as a result, increase bus passengers according to time process.

In this paper, in comparison of results of questionnaire surveys in one month and one year after introducing these new bus services to support the elderly person's activities, some interesting findings concerned with the effects of time process. These information may be useful to investigate the introduction of further trials in many cities which gave same problems.

### **Practical Use of Infrastructure Stock - From View Point of Reallocation of Road Space –**

Yasuo HINO

*Annual Report of Institute of Road Study in Kansai Region, Vol.40, pp.2-7(2016) (in Japanese)*

This paper intends to propose the necessity both of reallocation of road space in conformity with the needs in the future and the invariable policy, from view point of practical use of infrastructure stock. The contents of this paper were consist of four parts. At first, some major social problems caused by motorization and road network construction as the countermeasure of those problems were reviewed in comparison with the change of social conditions. Secondly, the quality of road space may be not enough in terms of reviewing the functions and required quantity of road. Thirdly, the new thinking of road construction was investigated with some trials of reallocation road space at home and abroad. Finally, the necessity both of reallocation of road space in conformity with the needs in the future was emphasize with the invariable policy.

### **A Prospect of road safety based on major problems for last 5decades**

Yasuo HINO

*Traffic Engineering, Vol. 51, No.1 pp. 44-45(2016) (in Japanese)*

In Japan, the real motorization started from 1960's have required to rectify the traffic flow by road constructing and signal controlling, in order to improve the traffic congestion. In the next decade, the frequently occurrence of traffic accidents was the serious social problem. And from 1980's the environmental problems caused by automobiles became appearance as the next social problem. As a result, it goes without saying that the role of traffic engineering must be most important to cope with these serious problems, during 50 years from starting the motorization. In this paper, the new approach for some problems which may occur in the coming decades was referred by reviewing such social history of 50 years concerned with motorization.

### **A Case Study on the Relationship between Discretionary Travel of Mobility Difficulties and Service Level of Public Transportation in Urban Area**

Yuto ARUJI, Nagahiro YOSHIDA and Yasuo HINO

*Japan Associate of Civil Engineers, Proceedings of Infrastructure Planning, No. 52, pp.1893-1896 (CD-ROM)(2015) (in Japanese)*

From "5th Kinki person trip survey" conducted in 2010, person with mobility difficulties were surveyed for the first time. According to the report, while mobility difficulties were expected to increase with the progress of aging in recent years, people with mobility difficulties in a relatively traffic highly convenient urban areas still face some difficulties in their daily travel.

In this study, using a questionnaire survey and PT survey data in Sumiyoshi ward of Osaka, the relationship between discretionary travel of mobility difficulties and service level of public transport were analyzed as a case study.

### **Daily Needs and Challenges of Tandem Bicycle for the Disabilities**

Yoriko YARIYAMA, Nagahiro YOSHIDA and Itaru FUJIE

*The City Planning Institute of Japan, The 14th annual conference of Kansai branch, pp.105-108 (2016) (in Japanese)*

Tandem bicycles are a human-powered vehicle with more than two saddles and two sets of pedals. Tandem bicycles have some potential benefit for the people who cannot ride bicycle by themselves like the visually-challenged, the intellectually-challenged or some of the elderly. This type of bicycle could offer a cycling opportunity and improve their daily activities. However these are only used as sports or sightseeing purpose in Japan so far. In addition, as the potential benefits of tandem bicycles are not well-known, usage of tandem bicycles is regulated by each prefecture's traffic enforcement. Therefore we conducted a

questionnaire survey for users in order to understand current situations. Some results showed the disabilities would like to use tandem bicycles for their daily life and the bicycle would bring their daily travel longer while there are several concerns related with tandem bicycle usage; the difficulties of riding on busy roads, getting space of bicycle parking and finding the pilot who rides a front seat. Based on these findings we will make a tandem bicycles safety manual to move on to the next step.

### **Toward to Realize a Bicycle Town through the Critical Mass Event “Midosuji Cycle Picnic”**

Itaru FUJIE, Nagahiro YOSHIDA and Yoriko YARIYAMA

*The City Planning Institute of Japan, The 14th annual conference of Kansai branch, pp.101-104 (2016) (in Japanese)*

The prevailing image of cycling in Japan is still negative due to the long history of countermeasures for illegal parking issues or undesirable cyclists' behaviors. Under these situations, some interested people planned a unique cycling demonstration event called as Midosuji Cycle Picnic for raising the awareness of positive images of cycling. The purpose of the event is 1) to demonstrate the cultural diversity of cycling for publics, 2) to get reliance about right-of-way from car drivers, 3) to increase the number of desirable cyclists who could use hand signals or eye contact with drivers, and 4) to make some recommendations for improving the condition of cycling infrastructure through demonstration. This paper deal with the concept of this event toward to realize a bicycle town as well as the evaluation of the participant comments in the latest event.

### **Link-based Accident Risk Analysis Using Near Miss Incidents in Trunk Roads**

Satoki KUBOTA, Nagahiro YOSHIDA and Masashi NISHIOKA

*Japan Society of Traffic Engineers, Proceedings of the 36th annual conference(research paper), pp.229-232, (2016) (in Japanese)*

Recently, the number of traffic accidents and casualties are decreasing, but in trunk roads compared with residential streets, there are still many traffic accidents casualties. Although the implementation of remedial measures is known as a typical method to reducing traffic accidents after identifying the accident hazardous areas based on accident statistics, it takes longer time to collect accident data. So, in order to tackling with potential hazardous area, it is important to evaluate traffic accident risk in a short period of time. The purpose of this study is to analyze the relationship between traffic accidents and two near-miss-incident indicators which are objective data collected from vehicle and subjective data evaluated by the local residents and road user.

### **250m Square Mesh Model of Upper Pleistocene Deposits (Dg1 and Ma12) in Osaka Area and Settlement Prediction by Dewatering**

Shun ARAI (West Japan Railway Company), Akihiko OSHIMA, Suguru YAMADA, Azusa TSUTSUMI (NEWJEC), Teruyuki HAMADA, Mari KASUGAI and Yoshitaka KONDO (Geo-Research Institute)

*Proceedings of the Kansai Geo-Symposium 2015, JGS\_KB, pp. 45–50, 2015. (in Japanese)*

### **About a Comparison between Liquefaction Strength by Each Guideline**

Hisanori NAGAI (Konoikegumi), Akihiko OSHIMA, Fusao OKA (Kyoto University), Kazuaki HIOKI (Osaka Institute of Technology), Seiji KAI (Dia Consultant), Atsushi SAGAWA (Chouhukken Consalutants), Kouji HIRAI (Atec Yoshimura), Haruo FUKAI (Kiso-Jiban Consalutants) and Kazufumi KAWASAKI (MLIT Kinki Regional Development Bureau)

*Proceedings of the Kansai Geo-Symposium 2015, JGS\_KB, pp. 197–202, 2015. (in Japanese)*

### **Construction of the Site Amplification Map using 250m Square Mesh Models of Shallow Subsurface Structures in Osaka Area**

Toshiyuki HIRAI, Azusa TSUTSUMI (NEWJEC), Akihiko OSHIMA, Shun ARAI (West Japan Railway Company), Teruyuki HAMADA, Naoko KITADA (Geo-Research Institute), Hiroyuki GOTO (Kyoto University), Katsuyuki KAWAI (Kinki University) and Isao NAKAJIMA (Oyo Corporation)

*Proceedings of the Kansai Geo-Symposium 2015, JGS\_KB, pp. 203–208, 2015. (in Japanese)*

### **Transition of Ground Improvement Technologies in Japan: II : Current Situation in Ground Investigation and Countermeasure for Liquefaction**

Akihiko OSHIMA, Kenji HARADA and Shigehiro MURAKAMI (Fudo Tetra Corporation)  
*Journal of the Society of Materials Science, Japan*, Vol. 65, No.9, pp. 687–693, 2016. (in Japanese)

### **An Attempting Research on Evaluating Grain-size Characteristics based on Acoustic Properties of Soil for Liquefaction Assessment by Swedish Ram Sounding**

Suguru YAMADA and Akihiko OSHIMA

*Proc. of the 15th Asian regional conference on soil mechanics and geotechnical engineering*, Fukuoka, Japan, Nov., Paper No. JPN-142, 2015.

In order to achieve the economical assessment of liquefaction safeness for an individual residential property by Swedish Ram Sounding (SRS), an attempting research on evaluating the grain-size properties of strata employing acoustic properties of soils was carried out. The sounds generated by friction between soils and stainless-steel metal during direct shear testing and SRS were recorded. And then, their acoustic properties were compared with grain size properties of soils. As results of examination on their relationships, the possibility was discovered that the fines content,  $F_c$ , at certain stratum and presence or non-presence of plasticity of fines would be able to estimate based on the spectrum shape of frictional sound. The trends were also observed that the frictional sound of soils without plastic fines has narrow spectrum width and its peak frequency might be affected by particle size.

### **Evaluation of Grain-size Properties using Soil-Metal Frictional Sound for Liquefaction Assessment by Swedish Ram Sounding**

Suguru YAMADA, Akihiko OSHIMA and Shigeyoshi HIRATA (Daiwa House Industry Co., Ltd.)

*Proc. of the 6th International Conference on Earthquake Geotechnical Engineering*, Christchurch, New Zealand, Nov., paper No. 572, 2015.

This article presents a possible idea for evaluating grain-size properties of subsurface soil through an operation of Swedish Ram Sounding (SRS) by employing acoustic properties of friction sound generating by friction occurs between surface of metallic penetration cone and surrounding soil. A series of soil-metal friction test was performed on silica sand with various fines content using a modified direct shear apparatus to simulate a friction phenomenon between SRS cone and soil. As a result of experiments, it was found that the sound pressure level (SPL) of friction sound was depended on relative density as well as fines content of sandy specimen. Based on obtained testing results, an idea for evaluating fines content of ground by SRS was tentatively proposed.

### **Laboratory Tests on Cyclic Undrained Behavior of Loose Sand with Cohesionless Silt and Its Application to Assessment of Seismic Performance of Subsoil**

Yolanda Alberto HERNANDEZ, Ikuo TOWHATA, Keigo GUNJI (Univ. of Tokyo) and Suguru YAMADA

*Soil Dynamics and Earthquake Engineering*, Vol. 79, Part B, pp. 365–378, 2015.

Geotechnical earthquake engineering in the recent times has been paying special attention to themes such as liquefaction of sand with cohesionless fines, performance-based design, and seismic mitigation measures for housing areas. Because recent earthquakes in Japan and New Zealand caused many liquefaction problems in residential zones, the above-mentioned issues have become even more important than before. The present study conducted laboratory tests on sand with cohesionless fines in order to show how the seismic performance of loose subsoil is assessed, thus developing a practical methodology of performance-based mitigations. Most experimental data obtained is presented together with interpretations, and the mathematical framework for the performance assessment is described together with an example of specified mitigation methods. It is worth mentioning that the target of this assessment is the residential land of people who cannot afford high costs of testing and analysis, therefore, the methodology is simplified as much as possible.

### **Estimation Method on Power Transduce from Waves by a Watermill Installed in a Chamber of a Vertical-slotted Breakwater**

Shinji MORIMOTO, Takaaki SHIGEMATSU, Daichi UEJIMA, Kenji KATOH, Tatusro WAKIMOTO and Shin'ya YOSHIOKA

*Journal of Japan Society of Civil Engineers, Ser.B2 (Coastal Engineering)*, Vol. 71, No. 2, I\_1567-I\_1572 (2015) (in Japanese).

Renewable energies as substitute energy of nuclear power get much attention in not only Japan but also the

world. Authors focus on the wave energy and have developed a wave power generation system using a vertical slotted breakwater with watermills installed in the chamber. From view point of the practical realization, it is necessary to estimate electrical power obtained by the watermill and power generation cost with enough accuracy as possible as we can. In the previous work, authors developed the experimental formulation between rotation rate of watermill and velocity amplitude through a vertical slit of the breakwater. In this paper, effect of scale of laboratory experiment was investigated through a series of experiments in different scale. Based on the experimental results, the formulation was modified so that the power obtained from wave by a watermill may be obtained with enough accuracy.

#### **Investigation on Criterion of Splash Generation by Wave Acting on a Coastal Structure**

Masahide TAKEDA (TOA Corporation), Yuki YASUHIRA, Takaaki SHIGEMATSU, Muneo TSUDA (TOA Corporation), Takashi HABUCHI (TOA Corporation) and Takahiko AMINO

*Journal of Japan Society of Civil Engineers, Ser.B2 (Coastal Engineering)*, Vol. 71, No. 2, I\_853-I\_858 (2015) (in Japanese).

In this study, we aimed to derive the criterion of splash generation by wave acting on an impermeable vertical wall using hydraulic experiments and numerical simulations, in order to estimate the salt supply to port and harbor structure in close proximity to the surface of the sea. We found that the criterion of splash generation can separate into two different forms of splash generation using the maximum of vertical acceleration of water mass rising along vertical wall.

#### **A Study on Properties of Flow and Free-Surface Oscillations Induced by Oscillating Circular Cylinder Arrays**

Hiroshi MATSUMOTO and Takaaki SHIGEMATSU

*Journal of Japan Society of Civil Engineers, Ser.B2 (Coastal Engineering)*, Vol. 71, No. 2, I\_877-I\_882 (2015) (in Japanese).

The properties of flow and free-surface oscillations induced by oscillating circular cylinder arrays in stationary fluid were investigated by hydraulic experiment. Not only longitudinal sloshing but also transverse sloshing were observed depending on the oscillation conditions of circular cylinder arrays. Longitudinal sloshing occurred when the frequencies of circular cylinder arrays nearly equaled to the natural longitudinal sloshing frequencies of a rectangular tank. The largest free-surface displacement occurred when longitudinal sloshing occurred. The flow structures were generated and transverse turbulent intensity increased around circular cylinders by transverse sloshing occurrence.

#### **Storm Surge Hindcast and Return Period of a Haiyan-Like Super Typhoon**

Kenzou KUMAGAI (Pacific Consultants Co. Ltd.), Nobuhito MORI (Kyoto University) and Sota NAKAJO

*Coastal Engineering Journal*, Vol. 58, Issue 01, 1640001, [24 pages] (2016)

The extremely intense Typhoon Haiyan (local name Yolanda), struck the Philippines in November 2013, catastrophically impacting the region. It is important to understand the storm surge characteristics and occurrence probability of such super typhoons for reconstruction of the devastated area. This study mainly examines two topics. First, the characteristics of Typhoon Haiyan and its related storm surge were analyzed with a series of numerical experiments using an empirical typhoon model and storm surge model. The maximum surge height and inundation area were estimated and validated against measurements of tides and wind speeds obtained from local agencies NAMRIA and PAGASA, as well as against post-event surveys of maximum inundation heights. Based on the analysis of best hindcast results, the maximum storm surge level was about 5m at Tacloban on Leyte Island. Second, the return period of a Haiyan-like typhoon and associated storm surge was estimated with NOAA's long-term observed IBTrACS typhoon dataset and a stochastic tropical cyclone model. Statistical analysis of typhoons around Tacloban was performed, and the estimated return period of storm surge levels seen during Typhoon Haiyan is 240–360 years.

#### **A Basic Study of Estuary Delta Topography Long-term Predictive Model Which Can Consider a Future External Force Change**

Kohei NAKANISHI (Obayashi Co. Ltd.), Sota NAKAJO and Takaomi HOKAMURA (Kumamoto

University)

*Journal of Japan Society of Civil Engineers, Ser. B2 (Coastal Engineering)*, Vol. 71, No. 2, p. I\_505-I\_510 (2015) (in Japanese)

The objective of this paper is to grasp estuary delta topography change on having considered a future external force change by using a long-term predictive model. The 38 years topography data of Shirakawa river including two years data which we got from survey can explain the process of extension of the delta. High potential of our process-based model for prediction of vertical profile of river delta was proved after some tests in ideal condition of wave, tidal current and river flood. After that, we simulated historical development of Shirakawa river delta by using our model with some observation data. Finally, future prediction of topography of river delta including climate change effect such as sea level rise was conducted.

#### **Physical Modeling of Surge-like Wave Impact on Urban Structure Due to Tsunami Inundation**

Yukari FUKUSHIMA(NEWJEC Inc.), Kenji EBISU(NEWJEC Inc.), Sota NAKAJYO, Takaomi HOKAMURA(Kumamoto University), Gozo TSUJIMOTO(Kobe City College of Technology), Masayasu MIYAKE(National Institute of Technology, Hakodate College) and Tetsuya KAKINOKI(Kobe City College of Technology)

*Journal of Japan Society of Civil Engineers, Ser. B2 (Coastal Engineering)*, Vol. 71, No. 2, p. I\_271-I\_276 (2015) (in Japanese)

This work aims to investigate the impact of a surge-like wave front on urban structures by performing physical experiments. Flume experiments are being conducted to test the hydrodynamic impact of surge on urban structures, with a particular interest to assess the role of an embankment-like structure in reducing hydrodynamic loadings. Since the onshore wave front induced by a tsunami or storm surge commonly propagates as a hydraulic bore, its hydrodynamic features are similar to those of a dam-break flow. Therefore, it is feasible to use a dam break to mimic an onshore tsunami or surge wave in laboratory, which is much straightforward to be implemented in practice. The laboratory measurements provide data for understanding the physics of the underlying processes of surge-structure interaction and for validating numerical tools.

#### **A Parametric Study on Potential of Storm Surge in TOKYO BAY**

Sota NAKAJYO, Hideyuki FUJIKI(Kumamoto University), Sooyoul KIM(Tottori University), Nobuhito MORI(Kyoto University), Yoko SHIBUTANI(Tottori University) and Tomohiro YASUDA(Kyoto University)

*Journal of Japan Society of Civil Engineers, Ser. B2 (Coastal Engineering)*, Vol. 71, No. 2, p. I\_199-I\_204 (2015) (in Japanese)

By using about 80 years historical data of tropical cyclone which passed through near Tokyo Bay area, this paper has estimated the potential of extreme storm surge event. Temporal variation of minimum central pressure and translation speed of along tropical cyclone tracks which will cause severe storm surge event has been determined from envelope curve of historical data, although tropical cyclone tracks themselves were assumed to same to those of original. Physical process of storm surge was simulated by the nonlinear shallow water equation. As a result, expected maximum storm surge at Tokyo was estimated about 1.8 m. This study clarified that northward cyclone tracks are especially dangerous for Tokyo bay because wind induced surge, rapid wind direction change, and harbor oscillation affect significantly.

#### **Estimation of Worst-class Tropical Cyclone and Storm Surge, and Its Return Period –Case Study for ISE BAY-**

Yoko SHIBUTANI(Tottori University), Sota NAKAJYO, Nobuhito MORI(Kyoto University), Sooyoul KIM(Tottori University) and Hajime MASE(Kyoto University)

*Journal of Japan Society of Civil Engineers, Ser. B2 (Coastal Engineering)*, Vol. 71, No. 2 p. I\_1513-I\_1518 (2015) (in Japanese)

In several decades, numbers of studies have been conducted to assess the impact of climate changes on tropical cyclones. It is reported that tropical cyclones will become more intense in future and indicated that storm surge risks will be significantly severer. In the present study, we conducted a series of Typhoon Vera storm surge simulations as changing scenario-based typhoon tracks under pseudo global warming scenarios and model-based ones by a global stochastic tropical cyclone model in the Ise Bay. We aimed to take a look at the maximum surge level as changing the central pressure depression and track of Typhoon Vera in order

to estimate a group of typhoons that induces the highest surge levels in the Ise Bay. Our results showed that the maximum surge level due to Typhoon Vera with the worst track is 1.5 m higher than the observed maximum surge level due to the typhoon with the original track. In addition, we estimated that its return period is 430 year.

#### **The Effect of Small Fluctuation of Atmospheric Pressure and Tide to Development of Seiche around KYUSHU Coastal Area**

Ryuta YAMAGUCHI(Japan Port Consultants, Ltd.), Hayato TAKAYAMA(TAISEI Co.), Sooyoul KIM(Tottori University), Masaya KATO(Kumamoto University), Hideyuki FUJIKI(Kumamoto University) and Sota NAKAJO

*Journal of Japan Society of Civil Engineers, Ser. B3 (Ocean Engineering)*, Vol. 72, No. 2, p. I\_312-I\_317 (2016) (in Japanese)

Exceptional long wave called ‘Abiki’ (it’s a kind of meteotsunami or seich) has occurred around west coast on Kyushu Island from winter to spring season. Previous studies on Abiki showed initial amplification mechanism called Proudman resonance caused by low crest pressure waves, and secondary amplification mechanism caused by resonance between long wave and bay. However, the nonlinear relationships of tidal variation and Abiki has not been made clear so much. In this study, we tried some simulations of Abiki occurred on Feb., 2009, and basic analysis of interaction between tidal variation and development process of Abiki by using numerical model of nonlinear long wave equation.

#### **Characteristics of Water Level Rise Speed by Storm Surge at Inner Part of YATSUSHIRO BAY and Disaster Reduction Activity**

Sota NAKAJO, Hideyuki FUJIKI(Kumamoto University) and Sooyoul KIM(Tottori University)

*Journal of Japan Society of Civil Engineers, Ser. B3 (Ocean Engineering)*, Vol. 72, No. 2, p. I\_25-I\_30 (2016) (in Japanese)

The operation of tidal gate constructed in river is difficult when heavy rain is forecasted because flood risk is significant. The delay of operation caused overflow by storm surge in Yatsushiro Bay at August 2015. One of the reason was unexperienced high speed of water level rise. In this study, we analyzed the mechanism of this phenomena and compared to past storm surge events. Then we assessed the variance of water level rise speed from virtual tropical cyclone scenario. Finally, typical tropical cyclone tracks causing high water level rise were selected. Then one viewpoint to assess the possibility of dangerous storm surge event was shown.

#### **Effects of Current on Sediment Transport at DINH AN Estuary, MEKONG RIVER, VIETNAM**

Ngoc Thanh NGUYEN(Kumamoto University), Sota NAKAJO and Toshifumi MUKUNOKI(Kumamoto University)

*Journal of Japan Society of Civil Engineers, Ser. B3 (Ocean Engineering)*, Vol. 71, No. 2, p. I\_790-I\_795 (2015)

Deposition at semi-diurnal tide estuaries is tremendously complicated due to the competition of river discharge and ocean tide. The difficulty in assessing deposition on estuarine bed is we have limited information about characteristics of river and tidal current. This study investigates current distribution and the relationship between current and sediment transport at Dinh An estuary, Mekong river, Vietnam. An Acoustic Doppler Current Profiler (ADCP) was used to measure river discharge and vertical current at Dinh An estuary in high-flow season in September 2009, then three-dimensional model was employed to figure out the effects of current on sediment transport. It was found that currents were stratified at the estuary in reversal period corresponding to certain range of discharge in ebb tide and in flood tide. Besides, suspended sediment concentration at the estuary strongly depends on magnitude and direction of current. Our study suggests that current distribution is the most important factor contributing to the serious accretion at the estuary.

#### **Blue Carbon in Human-dominated Estuarine and Shallow Coastal Systems**

Tomohiro KUWAE (Port and Airport Research Institute), Jota KANDA (Univ. of Marine Science and Technology), Atsushi KUBO (Univ. of Marine Science and Technology), Fumiyuki NAKAJIMA(Univ. of Tokyo), Hiroshi OGAWA (Univ. of Tokyo), Akio SOHMA and Masahiro SUZUMURA (National Institute of Advanced Industrial Science and Technology)

*Ambio*, Vol. 45, Issue 3, pp 290-301 (2016)

Estuarine and shallow coastal systems (ESCS) are recognized as not only significant organic carbon reservoirs but also emitters of CO<sub>2</sub> to the atmosphere through air-sea CO<sub>2</sub> gas exchange, thus posing a dilemma on ESCS's role in climate change mitigation measures. However, some studies have shown that coastal waters take up atmospheric CO<sub>2</sub> (Catm), although the magnitude and determinants remain unclear. We argue that the phenomenon of net uptake of Catm by ESCS is not unusual under a given set of terrestrial inputs and geophysical conditions. We assessed the key properties of systems that show the net Catm uptake and found that they are often characteristic of human-dominated systems: (1) input of high terrestrial nutrients, (2) input of treated wastewater in which labile carbon is highly removed, and (3) presence of hypoxia. We propose that human-dominated ESCS are worthy of investigation as a contributor to climate change mitigation.

### **Hypothesis and Verification of Tidal Flats' Function to Receiving Water Areas (Invited)**

Akio SOHMA

*J. of Japan Society on Water Environment*, Vol. 39(A), No.4, pp 141-145 (2016) (in Japanese)

The function of tidal flats' ecosystem to the eutrophic-hypoxic estuary was evaluated by using a newly developed ecosystem model - the first model describing the ecological connectivity consisting of both benthic-pelagic and central bay-tidal flat ecosystem coupling while simultaneously describing the vertical micro-scale in the benthic ecosystem. The model was applied to Tokyo bay. The applied model demonstrated that the tidal flat creation and nutrients load reduction decreased the anoxic water volume and mass of detritus in Tokyo Bay. However, the creation of tidal flats led to the higher biomass of benthic fauna, while the nutrients load reduction led to the lower biomass of benthic fauna. In addition, the model demonstrated that reproducing reclaimed tidal flats, as existed in the earlier Tokyo Bay system, prevented an increase of oxygen consumption potential (hypoxia potential) and activated the grazing from lower to higher trophic production, compared to the existing Tokyo Bay system with reclamation of tidal flats. These results demonstrate the tidal flat's function of keeping both a clean and bountiful ocean, and of driving the environmental restoration spirals resulting in a high/bountiful biodiversity, a smooth nutrient transition from a lower to higher trophic level, and a high utilizable potential of stored nutrients in the estuary.

### **Characteristics of CO<sub>2</sub> Absorption and Emission in the High Water Temperature Seasons at the North Salt Marsh of Osaka Nanko Bird Sanctuary**

Toshiyuki TANAKA, Toru ENDO, Noriaki IKADA and Susumu YAMOCHI

*Journal of Japan Society of Civil Engineers, Ser. B2 (Coastal Engineering)*, Vol.71, No.1, pp.1-11, 2016 (in Japanese)

Field investigations were conducted at the north salt marsh of Osaka Nanko bird sanctuary (ca.43100 m<sup>2</sup>) in high water temperature seasons of 2012-2014 and the amount of net CO<sub>2</sub> absorption was estimated along with the characteristic of CO<sub>2</sub> absorption and emission on the surface of the sediment. Gross CO<sub>2</sub> absorption flux was closely related to sediment temperature, chlorophyll a and photon flux density, while CO<sub>2</sub> emission flux changed depending on the sediment temperature and groundwater level. The groundwater level was thought to be indispensable for estimating the flux of CO<sub>2</sub> emission on the sediment. For instance, when groundwater level was not taken into account, the CO<sub>2</sub> emission flux from the sediment reached 29 tons, showing 2.1 times higher than the value with consideration of the groundwater level. Using the relationship of CO<sub>2</sub> flux with sediment temperature, chlorophyll a, photon flux density and groundwater level, the total CO<sub>2</sub> absorption and/or emission of the north salt marsh of Osaka Nanko bird sanctuary was estimated as ca.23 tons for absorption and ca.14 tons for emission in May to September, 2014. These results suggest that a net of 9 tons CO<sub>2</sub> was absorbed and this salt marsh plays the role of a CO<sub>2</sub> sink in the high temperature season of a year.

### **Estimation of CO<sub>2</sub> Budget in the Artificial Salt Marsh Developed at Urban Coastal Zone by Seasonal 24-Hour Field Investigations of CO<sub>2</sub> Fluxes**

Toru ENDO, Yusuke NAKANO, Noriaki IKADA, Toshiyuki TANAKA, Junpei SHIMANO, Kohei MIYAWAKI and Susumu YAMOCHI

*Journal of Japan Society of Civil Engineers, Ser. B2 (Coastal Engineering)*, Vol.71, No.2, pp.1-1327-I-1332, 2015 (in Japanese)

In order to estimate CO<sub>2</sub> budget in a salt marsh in urban coastal zone, 24-hour field investigations of air-sea and air-intertidal flat CO<sub>2</sub> fluxes were conducted at the north salt marsh at Osaka nanko bird sanctuary every season. CO<sub>2</sub> fluxes from intertidal flat to the atmosphere ranged from -16.4 to 5.8 mg/m<sup>2</sup>/min, but the fluxes of both absorption and emission were very small in winter. On the other hand, CO<sub>2</sub> fluxes from sea surface to the atmosphere ranged from -2.5 to 2.0 mg/m<sup>2</sup>/min. The variation trends of air-sea fluxes of every season were similar. Next, in order to examine the characteristics of CO<sub>2</sub> absorptions and emissions, the relationships between each fluxes and environmental factors were analyzed. It was found that CO<sub>2</sub> emissions from intertidal flat were related with mud temperature and air-sea CO<sub>2</sub> fluxes related with pH. It was confirmed that CO<sub>2</sub> absorptions of intertidal flat could be estimated by photon flux density and micro algal photosynthesis rates. Finally, CO<sub>2</sub> budgets were calculated in consideration of variability characteristic of fluxes and area of intertidal flat and sea surface. It was found that the north salt marsh at Osaka nanko bird sanctuary usually absorbed CO<sub>2</sub> from the atmosphere in all seasons (CO<sub>2</sub> absorptions were 49.5 kg/day in spring, 32.5 kg/day in summer, 7.5 kg/day in fall, and 12.3 kg/day in winter).

### **Soil Environment and Reeds Growing at the Artificial Tidal Flat of Hannan Second District in Osaka Bay**

Masaki SUGIMOTO and Susumu YAMOCHI

*Journal of Japan Society of Civil Engineers, Ser. B2 (Coastal Engineering), Vol.71, No.2, pp.I\_1339-I\_1344, 2015 (in Japanese)*

Reeds were transplanted in 2004, together with some technologies to reserve rainwater, at the artificial tidal flat of Hannan Second District locating ca. 1Km away from the coastline of Osaka Bay. Reeds grew and increased their distributions at the salty tidal flat although they were known as a plant growing in brackish or freshwater areas. Some field surveys were conducted from May 2013 to January 2015 to examine the relationship between the growth of reeds and crucial environmental factors for the growth. The concentrations of carbon and nitrogen of the shoots were relatively high (Carbon: 35-45%, Nitrogen: 0.2-2.4%), suggesting that they were not nutrient deficient. Salinity of the sediment showed less than 21psu except for a short period after typhoon. Biomass of the shoots increased at stations where capacity for reserving rainwater into sediment was high. These results demonstrate that reeds can grow at the salty artificial tidal flats in they had high potential to reserve soil moisture.

### **Control of Manganese Concentrations in the Effluent of the Sea-based Waste Disposal Site**

Yoshinori KANJO

*Proceeding of the 5<sup>th</sup> Forum on Studies of the Environmental & Public Health Issues in the Asian Mega-cities (EPAM2014), pp.179-181 (2014)*

Mn<sup>2+</sup> ion concentrations in the pond of sea-based waste disposal site increased drastically below the thermocline depth and this result was supported with Eh-pH diagram for manganese. The effective countermeasure for the SBWDS was to dump up to the thermocline depth with alkaline materials such as incineration ash in order to increase the pH value in pond. After the implementation of this countermeasure, dissolved manganese concentrations in effluent and the pond in SBWDS decreased to less than 5 mg/L even in summer season.

### **Quantity Estimation of Material Stock and Demolition Waste in Osaka City**

Satoshi MIZUTANI and Yoshinori KANJO

*Annual Journal of Urban Disaster Reduction Research, Vol.1, pp.35-38 (2014) (in Japanese)*

### **Estimation of the Amount of Water Supply and Water Demand in the Post-quake Period in Osaka City**

Yoshinori KANJO, Masayuki MORI and Satoshi MIZUTANI

*Annual Journal of Urban Disaster Reduction Research, Vol.1, pp.83-87 (2014) (in Japanese)*

### **Using of Contact Oxidation Methods for the Treatment of Wastewater Containing Aromatic Compounds**

Akihito KUMAMI (Osaka Gas Co. Ltd.), Shojiro OSUMI (Osaka Gas Co. Ltd.) and Yoshinori KANJO

*Journal of Environmental Conservation Engineering, Vol.44, No.12, pp.667-675 (2015) (in Japanese)*

In order to treat wastewater containing high concentration of aromatic compounds, we evaluated the performance of the contact oxidation method by conducting a removal test with initial substrate

concentration of 1,500 mg/L phenol or 1,000 mg/L cresol. The test showed that compound removal rates were three times higher than when using the conventional activated sludge process. Also, these results suggested that contact oxidation provided higher resistance to 1,500 mg/L of the reaction inhibitor cresol. We conducted a continuous contact oxidation experiment at high load conditions for 50 days, which resulted in COD<sub>Cr</sub> removal of 6.5 kg/m<sup>3</sup>/d. Genetic analysis of microorganisms in the sludge revealed a dramatic change in bacterial flora and preferential growth, particularly of *Alcaligenes* sp. The test using labeled substance <sup>13</sup>C-phenol revealed the large contribution of *Alcaligenes* sp. to be able to remove phenol.

#### **Effect of Occurrence Time of Earthquake on the Balance between Water Supply and Demand in the Post-quake Period in Osaka City**

Kazuki NISHIMURA, Yoshinori KANJO and Satoshi MIZUTANI

*Annual Journal of Urban Disaster Reduction Research*, Vol.2, pp.29-34 (2015) (in Japanese)

#### **Fractionation Analysis of Phosphorus in Sewage Sludge and Phosphorus Recovery by Acid Treatment**

Yoshinori KANJO, Satoshi MIZUTANI and Masafumi OHTA

*Proceeding of the 6<sup>th</sup> Forum on Studies of the Environmental & Public Health Issues in the Asian Mega-cities (EPAM2015)*, pp.57-61 (2015)

In order to investigate the chemical forms of phosphorus in sewage sludge, several sewage sludge were fractionated into 6 categories, and we could obtain that the fractions of particulate reactive phosphorus (P-PO<sub>4</sub>-P) in the settled sludge, thickened excess sludge and digested sludge were about 20% to 30% to the total content of phosphorus. According to the acid treating experiments of sewage sludge, citric acid was suitable for solubilization of P-PO<sub>4</sub>-P, and acid treatment of sewage sludge led to increase recovery ratio of phosphorus.

#### **Distribution of Acid-extractable Pb Contents in Molten Slag from Municipal Solid Waste Incineration Ash**

Satoshi MIZUTANI and Yoshinori KANJO

*JJ Civil Eng.* 1(1): 002. pp.1-4 (2015)

In Japan, when molten slag from municipal solid waste incineration ash is used in the general environment, acid-extractable Pb contents must be lower than utilization criteria, as determined by JIS (Japanese Industrial Standard) K 0058-2 method. However, representativeness of 1,000 t of slag samples in practical usage is ineffective because only 6 g of samples are used for testing under such standards. This study has three aims: 1. to determine the variation of acid-extractable Pb contents in the 20 slag samples from one plant, 2. to estimate the probability of excess acid-extractable Pb content distributed among the 20 samples that adhere to utilization criteria, and 3. to show the importance of evaluating acid-extractable metal contents not based on a single analysed value but probability density. In this study, twenty lots of slag were sampled from one melting plant for two months in 2006. In the first experiment, 6 g of samples were taken from each lot at random and tested. In the second experiment, 20 portions were prepared from four lots of them and 20 of 6 g samples were taken from each small portion and tested. The results indicate that significantly high Pb values derived from heterogeneous character. The dataset shows a log-normal distribution and the rates exceeding the utilization standard are discussed based on probability density function.

#### **Variation of Acid-extractable Fluoride Content in an Increment and in a lot in Steelmaking Slag**

Satoshi MIZUTANI, Hirofumi SAKANAKURA (National Institute of Environmental studies, Japan) and Yoshinori KANJO

*Proceeding of the 6th Forum on Studies of the Environmental and Public Health Issues in the Asian Mega cities (EPAM & EMES-2015)*, pp.64-70 October 30-November 2, Xiamen, China (2015)

In order to manage safe utilization of steelmaking slag, samples of slag are examined to assess the levels of hazardous acid-extractable fluoride. From a conveyor of the slag products, 50 increments were obtained every 6 min for 5 h from one lot of a steel making slag to determine the analytical repeatability error of fluoride analysis and the acid-extractable fluoride content variation in an increment and in the entire lot. The analytical error of repeatability was 1.3%, which is a negligible. The coefficient of variance was 5.5% in an increment and 8.9% in the lot, therefore the variation in the lot is 1.6 times larger than that in an increment. All of the observed acid-extractable contents were sufficiently low for meeting the safe utilization criteria.

#### **Selective Recovery of Indium from Lead-smelting Dust**

Hikaru SAWAI (Kanazawa Univ.), Ismail M.M. RAHMAN (Univ. of Chittagong, Bangladesh), Yoshinori TSUKAGOSHI (Kanazawa Univ.), Tomoya WAKABAYASHI (Kanazawa Univ.), Teruya MAKI (Kanazawa

Univ.), Satoshi MIZUTANI and Hiroshi HASEGAWA (Kanazawa Univ.)

*Chemical Engineering Journal* 277 pp.219-228 (2015)

Non-ferrous smelting dust, especially lead-smelting dust (LSD), contains percent levels of indium and thus constitutes a novel indium resource. The main difficulty in recovering indium from LSD is the coexisting presence of lead and zinc. In this study, a unique indium separation process was designed, combining techniques that involve washing with a chelant, leaching with acid and precipitation as hydroxide. The majority of the Pb in the LSD was selectively separated during chelant-assisted washing with ethylenediaminedisuccinate (EDDS), while the residual Pb was diminished through an acid leaching treatment with a mixed solution of sulfuric acid and hydrochloric acid. The chelant washing step also ensures a decrease in the raw LSD weight at a ratio of approximately 82% due to the removal of lead and counter ions such as sulfate, and the washing step also minimizes the consumption of corrosive acids in the subsequent step. Selective indium separation from LSD is further complicated by the similarity of the behavior of zinc during the acid leaching step. Therefore, hydroxide precipitation at pH 5 has been introduced as the final step, ensuring the maintenance of zinc as a soluble species in the supernatant and the selective separation of indium (~88%) as a hydroxide precipitate.

### **Particle Size Dependency of Acid Extractable Contents and Leaching Quantity of Pb in Contaminated Soil from Shooting Range**

Satoshi MIZUTANI, Kenta HAYASHI and Yoshinori KANJO

*Proceeding of the 7th Forum on Studies of Environmental and Public Health Issues in Asian Mega-cities (EPAM2016)*, September 2-3, Muroan, Japan (2016)

Contaminated soils of which lead content is higher than 10000 mg/ kg are often found at shooting range because of lead pellet for shooting. In order to remove and recover lead from those soils effectively, the particle size dependency of lead concentration in contaminated soil is focused on in this study. The contaminated soil with smaller than 2mm particle size are divided into 5 fractions using the sieves with 2.0 mm, 0.85 mm, 0.425 mm, 0.25 mm, 0.075 mm of screen size, and the total contents, acid extractable contents and leaching quantity of lead from each fraction are determined. The negative correlation between particle size of the soil and total contents of lead are observed. The similar tendency is seen for the acid extractable contents. However, there are no correlation between particle size and leaching quantity, and the leaching behavior seems to be controlled by other factors.

### **Decontamination of Metal-contaminated Waste Foundry Sands using an EDTA-NaOH-NH<sub>3</sub> Washing Solution**

Hikaru SAWAI (Kanazawa Univ.), Ismail M.M. RAHMAN (Fukushima Univ.), Mayuko FUJITA (Kanazawa Univ.), Naoyuki JII (Kanazawa Univ.), Tomoya WAKABAYASHI (Kanazawa Univ.), Zinnat A. BEGUM (Southern Univ., Bangladesh), Teruya MAKI (Kanazawa Univ.), Satoshi MIZUTANI and Hiroshi HASEGAWA (Kanazawa Univ.)

*Chemical Engineering Journal* 296 pp.199-208 (2016)

Waste foundry sand (WFS), which is a hazardous byproduct from the foundry industry, is often contaminated with potentially toxic elements (PTEs), such as Cu, Pb and Zn, and widely re-utilized as a construction material. Therefore, the depollution of WFS has been suggested due to its environment friendly reprocessing to avoid potential long-term hazardous impacts. In the current study, a unique chemically induced technique has been proposed for the removal of PTEs from WFS. EDTA, NaOH and NH<sub>3</sub> were used as extractants in combination or in succession. The optimum removal of PTEs was accomplished using a solid (WFS) to solution (50 mmol/L EDTA) ratio of 10 under strongly basic pH conditions, which was achieved with NaOH addition. The washing efficiency was further enhanced with the addition of NH<sub>3</sub> to the solution. The complete process cycle duration was adjusted to 9 h with a washing sequence that was repeated three times for 3 h each. The ultimate efficiencies (%) for the removal of PTEs were as follows: Cu, 98; Pb, 81; Sn, 83; and Zn, 50. The leaching of residual PTEs (%) from the decontaminated WFS was also in compliance with the regulatory levels that are defined by the monitoring authorities.



